Experimental Investigations into the Fluid Dynamics and Forcing Underlying Cross-flow Turbine Operation

Abigale Snortland

A dissertation
submitted in partial fulfillment of the
requirements for the degree of

Doctor of Philosophy

University of Washington

2024

Reading Committee:
Owen Williams, Chair
Brian Polagye, Chair
Steven Brunton

Program Authorized to Offer Degree:
Mechanical Engineering

University of Washington

Abstract

Experimental Investigations into the Fluid Dynamics and Forcing Underlying Cross-flow Turbine Operation

Abigale Snortland

Co-Chairs of the Supervisory Committee:
Owen Williams
Aeronautics and Astronautics

Brian Polagye
Mechanical Engineering

Within the wind and marine energy sectors, axial-flow (i.e., horizontal axis) turbines are a well-established and well-understood approach to converting the kinetic energy in a moving fluid to electricity. Recent cross-flow (i.e., vertical axis) turbine research has yielded substantial performance gains through the exploitation of unsteady fluid dynamics for individual turbines and mutually beneficial interactions between closely-spaced turbines in arrays. However, an understanding of the dynamics underlying cross-flow turbine operation remains incomplete due to the presence of fluid phenomena that are difficult to model, including dynamic stall, flow curvature effects, and the influence of the turbine on the surrounding flow, called induction. This thesis considers the intricate relationship between the flow physics and performance of cross-flow turbines and augments understanding of their fundamental operation.

First, cross-flow turbine performance and flow fields exhibit cycle-to-cycle variations, though this is often implicitly neglected through time- and phase-averaging. This variability could potentially arise from a variety of mechanisms – inflow fluctuations, the stochastic nature of dynamic stall, and cycle-to-cycle hysteresis – each of which have different implications for our understanding of cross-flow turbine dynamics. In this work, the extent and sources of cycle-to-cycle variability, for both the flow fields and performance, are explored experimentally under two, contrasting operational

conditions. Flow fields, obtained through two-dimensional planar particle image velocimetry (PIV) inside the turbine swept area, are correlated simultaneously with measured performance using an unsupervised hierarchical clustering pipeline. A principal component analysis (PCA) pre-processor is employed that allows for clustering based on all the dynamics present in the high-dimensional flow-field data in an interpretable, low-dimensional subspace that is weighted by contribution to overall velocity variance. We find that the flow-field clusters and their associated performance are correlated primarily with inflow fluctuations, despite relatively low turbulence intensity. These inflow fluctuations drive variations in the timing of the dynamic stall process, while hysteresis between cycles is found to be negligible. Clustering reveals persistent ties between performance and flow-field variability during the upstream portion of the turbine rotation. The approach employed here provides a more comprehensive picture of cross-flow turbine flow fields and performance than aggregate, statistical representations.

Second, cross-flow turbine blades encounter a relatively undisturbed inflow for the first half of each rotational cycle ("upstream sweep") and then pass through their own wake for the latter half ("downstream sweep"). While most research on cross-flow turbine optimization focuses on the power-generating upstream sweep, we use single-bladed turbine experiments to show that the downstream sweep strongly affects time-averaged performance. Specifically, we find that power generation from the upstream sweep continues to increase beyond the optimal tip-speed ratio. In contrast, the power consumption from the downstream sweep begins to increase approximately linearly beyond the optimal tip-speed ratio due, in part, to an increasingly unfavorable orientation of lift and drag relative to the rotation direction. Downstream power degradation increases faster than upstream power generation, indicating the downstream sweep strongly influences the optimal tip-speed ratio. In addition, PIV data is obtained inside the turbine swept area at three tip-speed ratios. This illuminates the mechanisms underpinning the observed performance degradation in the downstream sweep and motivates an analytical model for a limiting case with high induction or an infinite tip-speed ratio. Performance results are shown to be consistent across 55 unique

combinations of chord-to-radius ratio, preset pitch angle, and Reynolds number, underscoring the general significance of the downstream sweep to cross-flow turbine performance.

Third, while investigating trends in terms of turbine-level forces and torques is important, it does not tell the full story of cross-flow turbine operation. Identification of blade-level forces and torques allows for specific investigations into how effectively fluid forcing on the blade drives rotation and can aid in blade structural design. Further, the determination of blade-level forces allows more robust comparison to computational fluid dynamic simulations. Here, we present a methodology for extracting blade-level forces and moments from experimental measurements at the axis of rotation for a single-bladed turbine. The method is based on knowledge of the flow physics and its validity is assessed via comparison with equivalent blade-only large-eddy simulations. By applying this method, we identify the fluid force components contributing to cross-flow turbine power production and forcing, illuminating the significance of the commonly ignored pitching moment. Failing to consider this term leads to an over-prediction of cross-flow turbine performance.

Overall, these three works contribute new methods, fundamental knowledge, and data to the field of cross-flow turbine research and together they constitute a set of well-characterized benchmark cases useful for informing future works that consider different turbine geometries, kinematics, or non-ideal inflows. Further these works provide useful insight applicable to improving reduced-order models and turbine structural design.

TABLE OF CONTENTS

LIST OF FIGURES

Figure Number Page

LIST OF TABLES

ACKNOWLEDGMENTS

This dissertation is the culmination of nearly six years of work and would not exist without the support and motivation that I have received in that time or the education I received prior. I want to first and foremost thank my advisors Brian and Owen who have believed in me and pushed me. Coming to the University of Washington I could not imagine ever pursuing a PhD, and I am endlessly grateful to them both for encouraging me to stay beyond my master's. I'd especially like to thank Brian for all the dedication he shows to the lab. The lab environment that you have fostered is special. The continuous support, insight, and stability you provided, while allowing me the ability to be creative and explore in my work has been a massive positive of my time here. Thank you Owen for your many many hours in the lab working with me to re-commision the PIV system, and the patient training you provided. Thank you for being a sounding board for all things airfoils and hydrodynamics and sharing your breadth of knowledge. I am grateful for both Brian and Owen for empowering me to expand my horizons. I would not be the researcher I am today without them. They have both allowed me to explore where my projects would take me, but reined me in when I strayed too far. I believe this has culminated in a satisfying body of work and established collaborations. To my committee members (present and past) Steven Brunton, Michael Motley, Alex Horner Devine, Alberto Aliseda, and James Riley, thank you for your time, consideration, and support.

I would be remissed to not expand on how wonderful the Marine Renewable Energy Lab and its associates are. I have had the pleasure to work closely with, to recreate with, to travel with, to grow friendships with so many who have passed through its doors. Each of you inspires me in so many ways, your research is top tier, your advise, patience, kindness, and support are difficult to put into words. I'm in awe most days of the quality of the people I get to work with, the

care they put into their work, and the time and effort they put into helping others succeed. I must specifically thank the members of the turbine group: Aidan Hunt, Ari Athair, Isabel Scherl, Kate Van Ness, Hannah Ross, Greg Talpey, and Carl Stringer for all the advice, help, late nights, hard work, knowledge, discussions, and inspiration that you infused into what has become this dissertation. I'm proud to be a part of our broader community, the Pacific Marine Energy Center, and the relationships that it has fostered. The breadth of marine energy research happening across multiple institutions is impressive, and PMEC has cultivated my far extending research network. I always appreciate running into you all here and afar, especially at EWTEC. I specifically want to extend my gratitude to my colleagues at the University of Wisconsin: Jennifer Franck, and Mukul Dave. Our collaborations and discussions, in person and virtually, have helped me grow as a researcher, inspired new ideas, and have culminated in exciting works. Thanks for talking all things hydrodynamics with me.

I would not be here today if it were not for my family, mentors, and colleagues who exposed me to research and supported and pushed me towards grad school, something I did not think I would do, nor know how to do. The support of my family has been constant. My parents have encouraged me through my entire education. I'll dearly remember the space camps and science fair projects and your belief I could excel in whatever I put my mind to. My grandma Tutu has endlessly supported my education and the travels it has pertained. Some of my favorite memories and engineering experiences of undergrad occurred on my Peru study abroad trip, made possible thanks to her. I also want to thank my Uncle Britt, my conversation with whom years ago spurred me to take the jump and commit to the PhD program. My time at Montana State University formed me into who I am today academically and recreationally, and introduced me to research in several ways. I specifically want to thank Roberta Amendola who inspired me to pursue grad school even though I never thought I would. I additionally largely credit my involvement in the Future Female Leaders in Engineering program at Los Alamos National Labs for placing me on a path towards graduate school and providing my initial funding. I am particularly grateful for the inspiring women I met

in the program and at the lab whose close friendships underscored my experience there including, Lia Meirose, Sophie Graf, and Sophie Weidenbenner.

To the earth for all its splendor. To the rivers, the snowy mountains, the muddy trails, the sunny beaches, and the red canyons. My recreation and exploration in these beautiful places is a cornerstone of my life, but it would not be the same without those I get to share that with. I especially want to extend my immense gratitude to my friends old and new who have seen me through undergrad to now. This community is something I am forever grateful for. It has brought me tremendous joy and connection, a reprieve from my studies, such fun, and adventures. My friends, especially those from my Bozeman crew, have seen me through all my years of college education and their near decade of friendship is of special importance to me. My Seattle friends have greatly added to my life and make this place home. Some notable memories I will forever hold near and dear: Bike fests, our river trips, backpacking trips, deep pow days and sunny slush laps, goofy parties and ridiculous costumes. In addition to my research, these adventures have rounded out a graduate school experience that has been one of the most satisfying periods of my life.

Lastly, I want to thank the funding agencies and folks who laid the groundwork that made this research possible. I want to thank the Alice C. Tyler Charitable Trust for supporting the research facility and to acknowledge the substantial contributions by Benjamin Strom, Hannah Ross, Aidan Hunt, Carl Stringer, Andy Witt, Erik Skeel, and Craig Hill to the development and upgrades of the experimental setup and code base I utilized throughout this work. Financial support for this thesis was provided by the United States Department of Defense Naval Facilities Engineering Systems Command, the Graduate Fellowship for STEM Diversity, and the National Science Foundation Graduate Research Fellowship Program. Thank you to all these programs for funding my ability to conduct high quality research.

.

DEDICATION

to my Parents and my Grandma Tutu

Chapter 1

INTRODUCTION

Elimination of fossil fuel dependence necessitates a diverse portfolio of renewable energy sources. Cross-flow turbines, consisting of blades that rotate perpendicular to the inflow, are able to harness the kinetic energy in wind, tidal currents, and rivers. While axial-flow devices currently dominate this space, particularly in wind, cross-flow turbines provide several benefits. These include lower rotation rates (reduced noise, lower risk of animal collision), omni-directionality (obviating yaw control), lower blade bending stresses and simpler construction, the ability for favorable generator positioning (e.g., on the water surface with floating platforms), and the potential to achieve greater scale for individual turbines [5, 6]. Cross-flow turbine arrays can benefit from interactions with neighboring turbines [7], and may also achieve greater power output per unit land area relative to axial flow devices [8]. However, as a consequence of the axis of rotation, the blades experience complex, phase-dependent dynamics. Because of this, the drivers of cross-flow turbine forcing and performance are less well understood relative to axial-flow devices, and no robust, computationally inexpensive design tools exist. Improving load predictions and understanding of cross-flow turbine performance are key steps towards the large-scale adoption of these devices. Therefore, it is the aim of this thesis to contribute methods for studying cross-flow turbine forcing and performance that provide insight into their fundamental operation.

Several factors complicate the fluid-structure interaction central to cross-flow turbine operation. First, throughout the turbine rotation, the blades encounter a continually fluctuating angle of attack and relative inflow velocity that can lead to the unsteady, non-linear phenomenon of dynamic stall [9–15]. Additionally, because of the rotation, flow curvature phenomena known as virtual camber and incidence become important, and the fluid dynamics are subject to the inertial Coriolis and centrifugal forces [16, 17]. Further, the influence of the turbine on the inflow through the rotor –

"induction" – is substantial [18–20]. Lastly, cross-flow turbine fluid dynamics and performance depend on a multitude of geometric factors and non-dimensional flow parameters including the ratio of the blade chord to the radius, the foil geometry, the preset pitch angle, the number of blades, the Reynolds number, the Froude number, and channel blockage [3, 19, 21–24]. Together these factors cause forces and torque to depend on a large parameter space, fluctuate with the blade position, and differ substantially between the first half of the blade rotation (the "upstream sweep") and the second half of the rotation (the "downstream sweep"). The upstream sweep is commonly referred to as the "power stroke" as it accounts for the majority of power generation, while the downstream sweep is characterized by limited power production, post- and secondary-stall events, and boundary layer reattachment. Because of the variety of fluid-structure interactions, it is critical to understand the relationship between the fluid dynamics, forcing, and performance of cross-flow turbines throughout the entire rotation.

Prior works have employed analytical, simulation, and experimental methods to predict, characterize, and design cross-flow turbines. Analytical methods and low-fidelity simulations aim to balance computational cost and accuracy when making cross-flow turbine performance predictions. Some examples include Double Multiple Streamtube Theory (DMST) [25–29] and vortex models (e.g., CACTUS code developed by Sandia National labs [30]). However, these models suffer in accuracy because they rely on lift and drag polars that are poorly characterized for unsteady rotating systems [31], and require empirical corrections to account for rotational effects such as virtual camber and dynamic stall. Further, they do not resolve details of the blade-level fluid dynamics, and so it is not possible to draw connections between the fluid dynamics and performance. For these reasons, experimental and higher-fidelity computational studies are desirable for more accurately studying performance and are requisite for exploring the fluid dynamics. Some authors have employed experiments to study pitching foil kinematics relevant to cross-flow turbines [32–37] and others have specifically attempted to use pitching and surging foils in a rectilinear reference frame as proxies for cross-flow turbines [15, 38–40]. However, since induction and rotational effects strongly influence cross-flow turbine dynamics, rectilinear kinematics cannot capture all the physics present in a rotational reference frame. Multiple computational studies have investigated performance in

conjunction with the in-rotor fluid dynamics of cross-flow turbines in a rotational reference frame [9, 10, 13, 14, 16, 41–45], but fewer [11, 46–48] have done so experimentally. These works highlight the complex relationship between the fluid dynamics and turbine performance, leaving many open questions. These include to what extent turbine performance and fluid dynamics vary between rotational cycles and how the dynamics of the downstream sweep influence performance. Further, a comprehensive understanding of how fluid forcing on the blades drives power production has not been comprehensively presented in the literature.

This thesis expands current field understanding of the fundamental operation of cross-flow turbines via experimental performance and flow-field investigations (Particle Image velocimetry, PIV), and yields data available for simulation validation. The work presented herein provides valuable insights applicable to improving turbine and blade design, control strategies, and modeling methods, all of which are essential for the commercial adoption of cross-flow turbine technologies. Chapter 2 presents an overview of cross-flow turbine theory. While experimental methods are similar across chapters, these are described with each line of investigation because aspects of the approach and nomenclature are distinct. First, Chapter 3 presents and applies a methodology for quantifying and determining the sources of cycle-to-cycle variations in cross-flow turbine performance and flow fields via an unsupervised clustering pipeline, comprised of well-known, data-driven techniques. This work demonstrates that the majority of cycle-to-cycle variations in our experiments are driven by inflow variations over relatively long time scales of $O(10\text{ s})$, such that time- and phase-averaging capture important dynamics. Second, Chapter 4 presents a specific investigation of performance and fluid dynamics in the downstream sweep and demonstrates its critical operational importance. Third, a new methodology for estimating blade-level force and torques from measurements at the center of rotation is presented in Chapter 5 and utilized to reveal trends in the force components contributing to cross-flow turbine performance. This includes the significance of the pitching moment term, which is commonly neglected in analytical formulations. Chapter 6 finishes with a summary of the major conclusions of this work, the contributions to knowledge, and suggestions for future work.

Chapter 2

BACKGROUND

Overall, cross-flow turbine kinematics, dynamics, and performance for a specific geometry and set of inflow parameters are functions of the tip-speed ratio, λ, and the blade azimuthal position, θ. The tip-speed ratio is the non-dimensional ratio of the tangential velocity (product of turbine radius to the quarter chord, r, and rotation rate, ω) to the freestream velocity, U_∞, and is defined as

$$\lambda = \frac{r\omega}{U_\infty}. \tag{2.1}$$

We define a 0° azimuthal position as corresponding to the location at which the blade tangential velocity vector points directly into the freestream (Figure 2.1a). The upstream sweep spans $\theta = 0° - 180°$ and the downstream sweep spans $\theta = 180° - 360°$. During each rotation, blades encounter a continually fluctuating relative inflow velocity, U_{rel}, (affecting the magnitude of the lift and drag forces) and angle of attack, α, (affecting lift and drag coefficients). The resultant force on the blade is a combination of lift, F_L, and drag, F_D, as shown in Figure 2.1b. Power production by the blades is a function of the tangential projection of the resultant force in the direction of rotation and its location along the blade chord, ω, and r.

2.1 *Common Nominal Kinematic Description*

Descriptions of the kinematic terms often utilize "nominal" formulations (U^*_{rel}, α^*) that assume the turbine does not affect the inflow and that velocities everywhere in the flow are equal to the free stream condition. Here, * denotes a model for a quantity that neglects induction. A schematic of the blade geometry, kinematic definitions, and azimuthal variations in $||U^*_{rel}||$ and α^* over one rotation are shown in Figure 2.1. Here $||\cdot||$ denotes magnitude. The nominal incident velocity at the quarter chord, $c/4$, is the vector sum of the tangential and freestream velocities, such that its

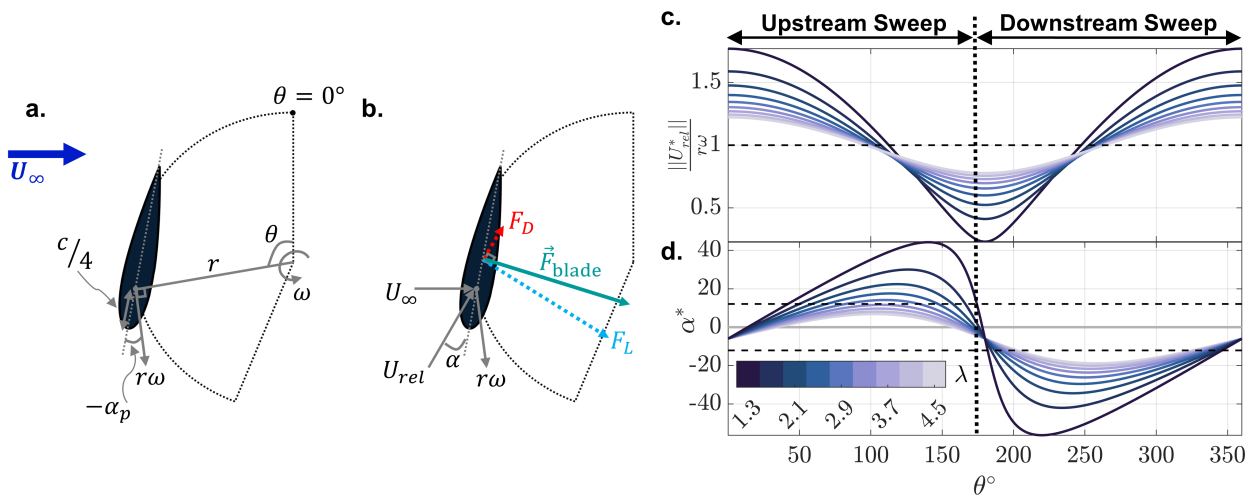

Figure 2.1: (a,b) Blade geometric definitions and forces, (c) normalized nominal relative velocity trajectories, and (d) nominal angle of attack trajectories for a preset pitch angle, α_p, of $-6°$. The tangential velocity is defined as tangent to the circular blade path. A negative (i.e., "toe-out") preset pitch angle is depicted in (a), and (b) shows the angle of attack definition. The static stall angle in (c) is for a foil in rectilinear flow at a similar Reynolds number ($Re_c = 1.5x10^5$,[1]). Because of the rapidly varying angle of attack and appreciable induction, the comparison between α^* and the steady-state stall angle is qualitative.

magnitude is

$$||U^*_{rel}(\lambda,\theta)|| = U_\infty\sqrt{\lambda^2 + 2\lambda cos(\theta) + 1}. \tag{2.2}$$

The nominal angle of attack, defined as the angle between the chord line and U^*_{rel} at $c/4$ is

$$\alpha^*(\lambda,\theta) = tan^{-1}\left[\frac{sin(\theta)}{\lambda + cos(\theta)}\right] + \alpha_p \tag{2.3}$$

where α_p is the blade preset pitch angle. As defined, a negative (i.e., "toe-out") preset pitch angle (Figure 2.1a) decreases the maximum angle of attack magnitude in the upstream sweep but increases the maximum angle of attack magnitude in the downstream sweep. For positive α^*, on the upstream sweep, the lift vector points inward to the center of rotation and, therefore, the suction side of the blade is the inner surface (closer to the center of the turbine). Conversely, for negative α^* on the

downstream sweep, the suction side of the blade is the outer surface. Nominally, a decrease in λ increases the range of α^* encountered during a cycle, which corresponds to increased dynamic stall severity and delayed flow recovery. Conversely, as λ increases, $||U^*_{rel}||$ converges towards the tangential velocity (Figure 2.1c).

2.2 *Dynamic Stall*

Because α and U_{rel} depend on λ, the phase, duration, and severity of dynamic stall are influenced by this parameter. A foil experiencing dynamic stall can produce lift far in excess of a static foil at the same angle of attack [32, 49–52], but flow separation from the blade is eventually accompanied by a significant loss of lift and increased drag. In severe, or "deep" dynamic stall cases (lower λ, larger α ranges), the near-blade flow field is characterized by the formation and roll-up of an energetic dynamic stall vortex that is of a similar size to the blade chord. This vortex grows to maturity and sheds before the maximum angle of attack is reached. After shedding, the blade experiences a sharp drop-off in lift production and an increase in drag. In contrast, any vortex growth in "light" dynamic stall cases (higher λ, smaller α ranges) is prematurely terminated and shedding is induced by flow entertainment from the pitch downs motion as α begins to decrease [35, 50]. Changes to the foil geometry (such as thickness) and the turbine control strategy can change the topology of dynamic stall experienced.

There remains debate as to whether dynamic stall should be completely avoided or simply controlled in the context of cross-flow turbines. Completely evading dynamic stall during operation neglects the benefit of increased lift during the dynamic stall process, but avoids the sharp lift reduction after vortex shedding. Complete avoidance can be achieved if the rate of change in α and the maximum of α are adequately small, and is possible at sufficiently high λ where the flow is dominated by the rotation. Nevertheless, it is clear from previous work that dynamic stall can occur at optimal λ for some turbines and blade geometries [9, 11, 53].

2.3 *Rotational Effects*

Flow curvature arises from the variation in the angle of attack and relative velocity along the blade chord such that a physically symmetric rotating foil behaves like a cambered one with a virtual incidence (change in the perceived angle of attack due to flow curvature) in rectilinear flow [17]. Virtual camber and incidence depend on the turbine geometry (particularly the ratio between the chord and radius, c/r), the azimuthal position, and the tip-speed ratio. These effects are understood to increase as c/r increases and/or λ decreases. The virtual geometry and incidence may be estimated via the conformal mapping methodology laid out by Migliore and Wolfe [17]. Further, the inertial Coriolis and centrifugal forces imparted by the turbine rotation may affect the near-blade fluid dynamics. As an example, Tsai and Colonious credit the Coriolis force for a "wake capturing effect" in rotating blade simulations where flow structures remain near the blade for longer than in rectilinear flow [16].

2.4 *Induction*

While neglected by the nominal kinematic description (Section 2.1), induction is unknown *a priori* but significant to cross-flow turbine operation. As power is extracted from the flow via forcing on the turbine, the flow must decelerate to satisfy conservation of mass, momentum, and energy. Flow is also diverted around the turbine and, if the flow is substantially confined, blockage accelerates the fluid through and around the rotor [54–57]. Together, these induction effects result in velocities in and around the rotor that differ from the freestream velocity, particularly in the downstream sweep. These in-rotor velocities depend on the blade azimuthal position, so, in reality, the blade kinematics differ appreciably between the upstream and downstream sweeps – a substantial departure from the nominal model. Because of this, the topology of the near-blade flow structures can also differ substantially between the upstream and downstream sweeps. The actual relative velocity magnitude incident on the blade is the vector sum of the induction-modified inflow and the blade tangential velocity, while the actual angle of attack depends on the angle between the relative velocity direction and the chord line (Figure 2.1a,b). The deviation between nominal and true values for α and U_{rel}

(Figure 2.1c,d) is most pronounced in the downstream sweep because of momentum extraction by the upstream sweep, but induction is also appreciable upstream.

Chapter 3

CYCLE-TO-CYCLE VARIATIONS IN CROSS-FLOW TURBINE FLOW FIELDS AND PERFORMANCE

This chapter contains content from "Cycle-to-cycle variations in cross-flow turbine flow fields and performance" published in the *Experiments in Fluids* special issue on vortex-dominated flows [58]. This work is co-authored by Isabel Scherl, Brian Polagye, and Owen Williams. Data collection was performed by the author and Isabel Scherl. All data analysis, visualization creation, and code base development were performed by the author. The manuscript was written by the author. Brian Polagye and Owen Williams advised throughout this project and were involved in the framing and editing of the final manuscript.

3.1 *Introduction*

Cross-flow turbine fluid dynamics are functions of both the blade azimuthal position and the tip-speed ratio, but cycle-to-cycle variability in performance and near-rotor flow fields is also observed. This is potentially caused by inflow fluctuations, hysteresis from previous cycles, and the sensitive and stochastic nature of dynamic stall itself. For example, any perturbations in the inflow velocity not only change the kinetic energy available in the flow but also change the instantaneous angle of attack and relative velocity encountered by the blade. This may, in turn, appreciably affect the timing and severity of dynamic stall. Similarly, Choudhry et al. [36] hypothesize that dynamic stall is influenced by the state of the boundary layer, which suggests that hysteresis from previous cycles, such as the extent of separated flow remaining on the blade at the beginning of the next cycle, may affect future dynamic stall. Additionally, the specific mechanisms underlying cycle-to-cycle variability could depend on the inflow conditions (e.g., Reynolds number), turbine geometry and kinematics.

Cycle-to-cycle variability is commonly neglected in the cross-flow turbine literature. RANS simulations, while often employed to study these flows, are inherently unable to accurately model cycle-to-cycle variations, and the computational expense of LES and DNS precludes their wider use to characterize this variation over a large numbers of cycles [34]. For experiments, these variations are implicitly neglected when data are time- or phase-averaged. However, phase-averaging can remove information that would otherwise assist in interpreting power production, vortex shedding, and stall, as well as distorting the timing and character of the dynamic stall process by smearing out non-linear phenomena and post-stall events [59–62]. As such, more sophisticated techniques that preserve cycle-to-cycle variability could provide additional insight into the flow-field physics. Some cross-flow turbine works do acknowledge the variability that is present in performance and/or flow-field measurements, but simply treat it as experimental uncertainty [23, 46, 63–65].

Our objective is to quantify the extent of cycle-to-cycle variation in cross-flow turbine performance and flow fields, its sources, and the relationships between performance and flow-field variability. To do so, we employ an unsupervised clustering pipeline, comprised of well-developed, data-driven methods, that identifies physically meaningful flow-field clusters with differing dynamics relevant to the dynamic stall process. Clustering was chosen since it can provide a basis for conditionally-averaging experimental data using all the dynamics present, rather than resorting to hand-engineered metrics (e.g., flow-field data based on phase-specific vortex separation from the foil surface). We are also able to correlate these flow-field clusters with performance and investigate the different sources of variability.

While cycle-to-cycle variability has not been explicitly studied for cross-flow turbines, variability in dynamic stall is the subject of several recent works [34, 59, 61, 62, 66, 67]. By using pressure tap measurements on a flapping foil, Harms et al. [61] investigated variability in dynamic stall and concluded that the phase-average and a measure of the spread (e.g., standard deviation) were descriptive of the general dynamics for cases where bivariate pressure distributions did not exhibit bimodal behavior. They hypothesized that the cases exhibiting bimodal behavior were more sensitive to inflow conditions and boundary layer unsteadiness. Tsang et al. [66] employed a wavelet analysis on lift and drag data from a flapping foil, and showed that non-stationarity between cycles

increased with stall severity. They hypothesized that this was the result of non-linear interactions between the fluid force and the pitching motion. Lennie et al. [59] used a Covolutional Neural Network on distributed pressure tap measurements to estimate cycle-specific vortex convection speeds, and hierarchical clustering on the coefficient of lift time-series to highlight underlying structure in the cycle-to-cycle variability. They found that vortex convection speed varied cycle-to-cycle, most prominently post-stall, and stall onset differed between the clusters. Because of this, phase-averaging inadequately represented portions of the data set. Kuppers and Reinicke [34] showed that using hierarchical clustering on the coefficient of lift time series on a flapping foil produced physically meaningful clusters. They found that one cluster exhibited a higher secondary lift peak than the other even though no clear bimodal behavior existed in the bivariate distributions. Ramasamy et al. [67] also employed clustering of distributed pressure measurements to investigate cycle-to-cycle variation for a pitching foil. They focused on cases with bimodal behavior in bivariate distributions and found that the clusters diverged in the post-stall region. They also showed that cluster-conditional averages deviated substantially from phase-averages, and that the clusters differed in shedding timing of the dynamic stall vortex (inferred from the pressure data), lift production, and flow recovery. They concluded that the clusters were associated with physical processes. These studies highlight the presence and complexity of cycle-to-cycle variability in systems that exhibit dynamic stall, and also demonstrate that phase-averaging can generate misleading representations. However, because none of these studies involve flow-field or inflow velocity measurements, they could not quantify the sources of the observed variability, characterize the flow-field variability beyond inference from force/pressure data, or directly correlate force and flow-field variability.

An analysis that considers both forces and flow fields is necessary to understand the extent and sources of the variability present and the sensitivity of the dynamics. However, unlike forces and pressures, flow-field data is high-dimensional in space and time, which poses apparent limitations on the use of clustering. Specifically, a “curse of dimensionality” arises for flow-field data because the algorithmic distances, such as the Euclidian distances, between individual flow-field snapshots begin to converge as the number of data points increases. In other words, from an algorithmic viewpoint, the flow-field snapshots begin to look equally similar and dissimilar from each other

even if they differ physically. This makes distinct clusters increasingly difficult to define [68]. As such, clustering of high-dimensional data requires adaptations for dimensionality reduction. Principle component analysis, PCA, is a well-known technique useful for decoupling the dynamics of complex, high-dimensional data sets, for feature selection, and for dimensionality reduction [69–75]. Additionally, several groups have demonstrated the use of PCA as a means of preserving dynamics otherwise smeared out by phase-averaging of unsteady, vortex-dominated flows [60, 62, 76]. Clustering in a PCA subspace is particularly useful because the PCA basis optimally maximizes variance in the data [67]. Because of this, PCA and clustering are commonly used in conjunction [77–81]. Additionally, clusters in a PCA subspace are a useful basis for producing probabilistic reduced-order models and for cluster-based feedback control [82, 83].

We explore the topic of cycle-to-cycle variability in cross-flow turbines using near-blade flow fields and performance (i.e., power output) for two distinct operating conditions. Through this, we characterize the flow-field variability and its connection with turbine performance using unsupervised, hierarchical clustering with a PCA pre-processor on the flow fields. The paper is laid out as follows. Section 3.2 provides a theoretical background for flow-field interactions with the moving rotor, then lays out the methodology for turbine performance and flow-field measurement, flow-field clustering, and correlations between flow-field clusters and performance. Section 5.3 quantifies the extent of cycle-to-cycle performance and flow-field variability, then explores how near-blade fluid dynamics, inflow velocity, and hysteresis from previous cycles contribute to the observed variability.

3.2 *Methods*

We begin with a discussion of the experimental acquisition of the simultaneous performance and PIV measurements in Sections 3.2.1-3.2.3, and conclude with a detailed description of the PCA analysis and flow-field clustering pipeline in Section 3.2.4. A contextual discussion of experimental uncertainty in flow fields and turbine performance is provided in Appendix A. The systematic uncertainty (accuracy of the central moment) indicated by this formal analysis exceeds the experimentally-observed variation. However, the aim of this work is to investigate the cycle-to-

cycle variability around the central moment that would normally be treated as random uncertainty.

Provided turbine geometry and all other relevant non-dimensional parameters (e.g., Reynolds number, Froude number, blockage) are held constant, phase-averaged hydrodynamic power, P, and the global velocity fields, $\vec{V}$, are functions of U_∞, λ, and θ [23, 63]. In this chapter λ is defined using the radius to blade outer surface ($D/2$). Within a single turbine cycle, n, hydrodynamic power is non-dimensionalized as the coefficient of performance $\eta(\lambda, \theta, n) = \frac{P(\theta)}{\frac{1}{2}\rho U_\infty^3 LD}$ where ρ is fluid density and L is the blade span. The coefficient of performance is often presented as C_P, but η is used here for notational simplicity and does not imply a "water-to-wire" efficiency.

3.2.1 Experimental Facility

Experiments were performed in the Alice C. Tyler flume at the University of Washington, a rendering of which is shown in Figure 3.1a. A free surface transducer measured a mean dynamic water depth, H, of 0.5 m, resulting in a channel cross-sectional area A_C of 0.375 m^2 (0.75 m width). The water temperature was maintained at 36.3 ± 0.2 °C, giving a ρ of 993.5 kg/m^3, and a kinematic viscosity, ν, of 7.1×10^{-7} m^2/s. An acoustic Doppler velocimeter (Nortek Vectrino) operating at a 100 Hz sampling rate and positioned approximately 5 diameters upstream of the turbine rotor measured the inflow. The average U_∞ was 0.7 m/s with a turbulence intensity, TI, of 1.8-2.1% . These conditions corresponded to a Froude number, $Fr = \frac{U_\infty}{\sqrt{gH}}$, of 0.32 where the gravitational constant g is 9.81 m/s^2.

3.2.2 Cross-flow Turbine

Experimental Setup and Measurements

These experiments utilized a one-bladed (NACA 0018 foil) turbine. The turbine has a radius of 8.6 cm, blade span of 23.4 cm, a blade chord length, C, of 4.06 cm and a $-6°$ preset pitch. Note: in this chapter, C is the chord length because of the cluster notation used in this chapter. The support structure comprised of a NACA 0008 foil strut at the top of the blade span and a large acrylic plate (40 cm diameter, 2.3x the rotor diameter) at the bottom. The plate facilitates PIV imaging of the

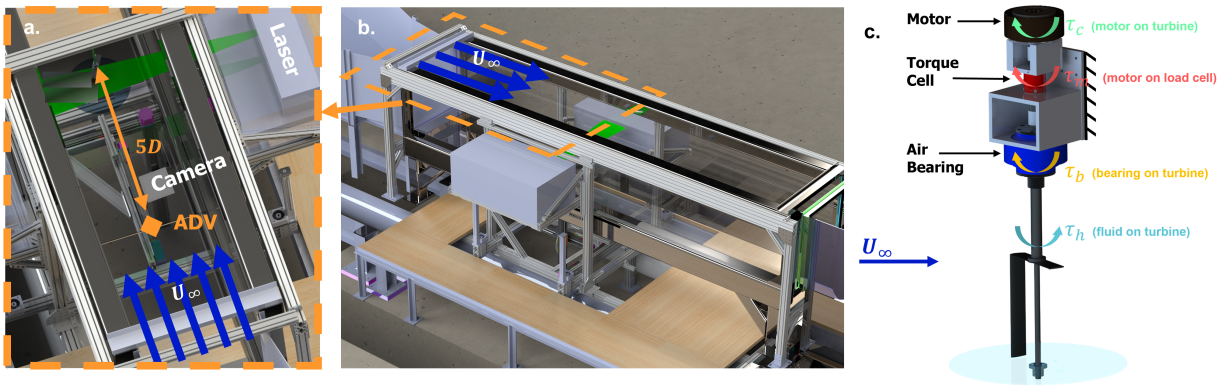

Figure 3.1: Annotated PIV experimental setup in the flume (a,b) and turbine free body diagram (c). The turbine is one-bladed but utilizes a top strut designed to support two blades.

mid-span from the cameras positioned below the flume (Figure 3.1a,c). Because turbine torque is measured in line with the drive train, a one-bladed turbine is necessary to directly tie performance variations to the near-blade flow fields (i.e., with a two-bladed turbine, the torque contribution from each blade is ambiguous). The blockage ratio, $\beta = \frac{LD}{A_C}$ is 8.9% and the Reynolds number, $Re_C = \frac{U_\infty C}{\nu}$ is 3.95×10^4.

As shown in Figure 3.1c, the turbine rotation rate, ω, is regulated by a servomotor (Yaskawa SGMCS-02B servomotor, Yaskawa SGDV-2R1F01A002 drive). In these experiments, we are operating under constant speed control holding ω constant, which requires the servomotor to apply a variable control torque, τ_c, which is measured by a hollow reaction torque cell (Futek FSH02595) rigidly coupled to the motor and flume cross beam. An air bearing (Professional Instruments Company Block-Head 4R low-inertia) absorbs the thrust moment while imparting a minimal bearing torque.

MATLAB Simulink Desktop Real-Time was used for data collection and turbine control. For each control set point (constant $\omega = 8.8 - 28$ rad/s in 1.6 rad/s increments, corresponding to $\lambda = 1.1 - 3.5$ in 0.2 increments), torque cell data were acquired for > 60 seconds (sufficient for convergence of the time-averaged statistics) at 1 kHz (upper limit of the acquisition hardware).

Blade position was measured by the servomotor encoder with a resolution of 2^{18} counts/rotation, also sampled at 1 kHz. The rotation rates were computed by taking the derivative of the measured blade position.

Blade-level Performance Calculation

Hydrodynamic power produced by the turbine is the product of the hydrodynamic torque, τ_h, and ω. At the turbine level, τ_h is the net hydrodynamic torque produced by the blades, less the parasitic torque from support structure drag. For constant ω and negligible bearing torque, the torque balance reduces to $\tau_h = \tau_c$.

Because the measured torque is dominated by the parasitic torque incurred by large bottom plate, "full-turbine" performance is not a meaningful metric. To this end, "blade-level" η is calculated by subtracting phase-averaged performance for the turbine support structure (no blade), $\langle \eta_S \rangle$, at the same inflow conditions from the full-turbine performance measurements, η_T (Figure 3.2). Here the $\langle\rangle$ brackets denote the phase-average which is conditional on λ and θ, or, in other words, an average for a single operating condition and azimuthal position across multiple cycles. Since the performance data is captured continuously, we utilize a 1° θ bin for phase-averaging. Blade-level η is used throughout to describe cycle-to-cycle performance variability. This approach requires that secondary interactions between the blades and support structures are minimal (demonstrated in [84, 85]) and that cycle-to-cycle fluctuations are dominated by variation in blade performance and not variation from the support structure.

All performance measurements were filtered with a low-pass, zero-phase, Butterworth filter to remove high-frequency electromagnetic interference from the servomotor. Both the 75 and 30 Hz cutoff frequencies used for the turbine and support structure performance data, respectively, are 10+ harmonics faster than the blade passage frequency. Additionally, the Butterworth filter has no effect on the time-averaged performance. Therefore, it unlikely the filter is removing any hydrodynamic power.

In calculating η, we note there is some ambiguity in the choice of U_∞^3. For example, one could attempt to use instantaneous velocity measurements, but there is a temporal mismatch between the

time the freestream velocity is measured and when it interacts with the rotor. Additionally, we cannot use PIV to estimate inflow since our field of view does not extend far enough upstream to measure the undisturbed inflow. Our notional choices are (1) to use a time-average of all of the cubed freestream velocity measurements acquired at a tip-speed ratio set point, or (2) apply an advection correction, as in [86], to compute the instantaneous freestream velocities and calculate cycle-specific kinetic power. The advection correction is based on a cross-correlation of U_∞ with measured power and the application of Taylor's frozen flow hypothesis. Option (2) performs poorly in these experiments, in that it generates greater relative variability in η than measured power, possibly because of the single-bladed configuration. Consequently, we utilize option (1), but in Section 3.3.3, we employ a hybrid approach to estimate "cluster-specific" kinetic power as an explanatory factor for cycle-to-cycle performance variation. A characteristic time-averaged performance curve, utilizing option (1), is given in Figure 3.3.

3.2.3 Flow Fields

Two-dimensional, two-component, phase-locked, flow-field measurements were obtained in a streamwise plane at the mid-span of the turbine, simultaneously with turbine performance measurements for two tip-speed ratios: $\lambda = 1.5$ (sub-optimal performance) and $\lambda = 2.5$ (near-optimal performance). While the performance measurements were continuously recorded over the entire turbine rotation, each PIV acquisition only captured flow-field data during each cycle at discrete, prescribed θ positions. PIV acquisition was controlled by TSI Insight, and acquisition for each cycle commenced upon receipt of trigger pulses sent at a specified θ from the Simulink model controlling the turbine. The PIV system returned pulses at each image pair capture instance (Figure 3.4a), the timing of which were logged by the Simulink model. Using these timing signals, the PIV snapshots were aligned with performance in post-processing. We note that this does not produce perfect phase-locking, but "phase jitter" between image pairs at the same θ was on the order of 0.009°, which we deem insignificant for the current analysis.

The general arrangement of the PIV laser and cameras is shown in Figure 3.1a. A dual cavity, Nd:YLF laser (Continuum Terra PIV) capable of a repetition rate of 10 kHz, illuminated the flow

with an approximately 2 mm thick light sheet in the field of view, FoV. A high-speed camera (Vision Research Phantom v641) with 2560 x 1600 resolution and a 105 mm lens at f# 16, and a calibration of 11.67 pixels/mm resulted in a FoV of 21.9 x 13.7 cm [5.4C (1.3D) x 3.4C (0.8D)]. With this magnification and the flow seeding (10 μm hollow-glass beads), the resulting particle images were approximately 2-3 pixels in diameter. To minimize laser reflections at the blade surface, matte black paint was applied.

As shown in Figure 3.4b,c, the combination of the camera lens focal length and streamwise extent of the laser sheet necessitated multiple FoVs to capture the important stages of dynamic stall and flow recovery. Each FoV outline is color-coded to denote the flow segment, S_k (where k denotes the segment letter), used in the clustering analysis detailed in Section 3.2.4. A single flow segment is captured per PIV experiment. The PIV parameters specific to each flow segment are

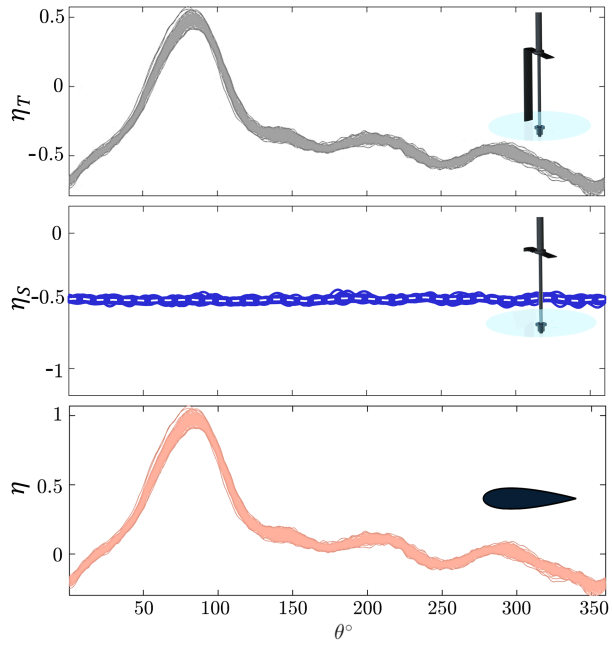

Figure 3.2: Schematic representations of the calculation of blade level performance, η, by subtracting support-only "performance", η_S, from the full-turbine performance, η_T, at the same conditions. $\eta = \eta_T - \langle \eta_S \rangle$.

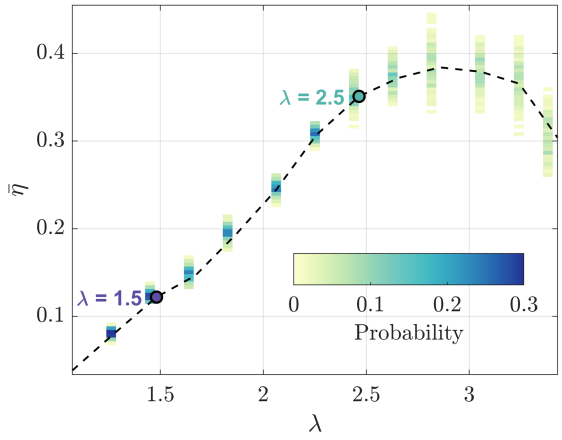

Figure 3.3: Time-averaged coefficient of performance for the one-bladed turbine investigated. The dashed line represents the time-average at each λ. Near-optimal (green dot) and sub-optimal (purple dot) cases are highlighted. The histograms (yellow to blue shading) describe the range of time-average performance over individual cycles at each λ.

listed in Table 3.1. Sequences of 9 image pairs for S_a, S_b and S_e, and 6 image pairs for S_c and S_d were acquired per rotational cycle with prescribed angular displacements, $\Delta\theta$, between frames ranging from $5.1 - 6.6°$, depending on desired phase resolution. The phase resolution is adjusted by setting the camera capture frequency equal to $\frac{\omega}{2\pi\Delta\theta} \times 360$. A total of 139 image pairs ($N = 139$ turbine cycles, limited by camera storage capacity) were acquired at each phase position, θ. FoV positioning relied on a combination of camera and turbine movement. A motorized, three-axis gantry positioned the camera relative to the laser sheet and provided the dominant adjustment for cross-stream FoV positioning, as well as fine adjustments in the streamwise direction. The limited streamwise extent of the laser sheet (Figure 3.4b,c) necessitated shifting the turbine by $\approx \frac{1}{2}D$ upstream to illuminate and capture the downstream blade sweep. Both the turbine shaft and blade cast shadows in the laser sheet. Therefore, to obtain data adjacent to the suction and/or pressure sides of the foil at all phases of interest, PIV measurements were repeated with the turbine spinning in both clockwise ($S_b - S_e$) and counter-clockwise (S_a) directions as depicted in Figure 3.4b,c. By

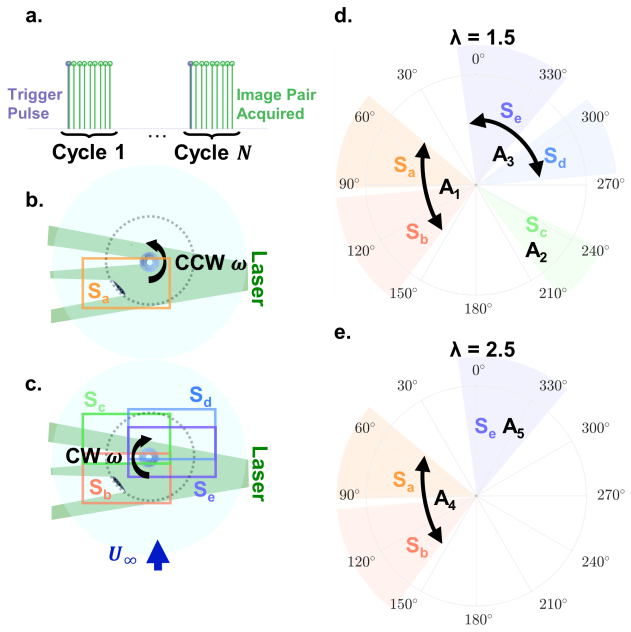

Figure 3.4: (a) A simple timing diagram for the PIV acquisition. Acquisition begins each cycle by the trigger pulse and then a pre-determined number of phase-locked image pairs are aquired at the prescribed camera capture frequency, For example, in S_a, 9 image pairs are taken after the trigger pulse each cycle. Field of view locations captured for (b) CCW rotation and (c) CW rotation. Example blade and support structure shadows are shown. Note that the $\theta = 0°$ reference changes with rotation direction, such that S_a does not overlap with S_b. (d,e) PIV segments captured for the different fields of view and visual representation of corresponding A matrix assignments for input into the PCA pre-processor.

changing the direction of rotation, we exploit the symmetry of the system to minimize the impact of blade shadows on the following analysis. In this way, we were able to image the suction side of the blade throughout the upstream sweep. For the downstream sweep, we choose to capture the side of the blade with the more visually distinct dynamics.

PIV processing was performed in LaVision DaVis (version 10.1.1). Background subtraction using a Butterworth filter on phase-matched images mitigated residual reflections and background

Table 3.1: PIV parameters for $\lambda = 1.5$ and $\lambda = 2.5$.

Parameter		$\lambda = 1.5$	$\lambda = 2.5$
ω	Hz	1.9	3.2
$\Delta\theta$ (S_a)		5.1°	5.1°
$\Delta\theta$ (S_b, S_e)		6°	6°
$\Delta\theta$ (S_c, S_d)		6.6°	N/A
Camera freq. (S_a)	Hz	135	225
Camera freq. (S_b, S_e)	Hz	115	191.7
Camera freq. (S_c, S_d)	Hz	105	N/A
Total image pairs (S_a, S_b, S_e)		1251	1251
Total image pairs (S_c, S_d)		834	N/A

illumination variation. The shadowed regions, visible turbine structures, and remaining reflections were manually masked prior to PIV processing. These masks are specific to each phase, as the shadows and location of the turbine structures vary with blade position. These phase-specific masks applied are functions of S_k, λ, and θ, but constant for all n. Processing utilized a multi-grid, multi-pass cross-correlation algorithm with adaptive image deformation with a 75% overlap and 32 x 32 pixel final interrogation window size resulting in a 0.69 mm vector spacing (approximately 60 vectors per blade chord). Spurious vectors (less than 2%) were removed with a universal outlier median filter [87] utilizing a 9x9 filter region and a threshold value of 1.5 for the $\lambda = 1.5$ cases and 2.5 for the $\lambda - 2.5$ cases.

All vector field post-processing was performed in MATLAB (R2020b). To align the different flow segments and limit the contribution of blade rotation in the PCA pre-processing, each FoV was translated from the flume reference frame to a blade reference frame. Figure 3.5 provides an overview of this process. First, we located and aligned the center of rotation between the different

FoVs. Tracking a small dot on the end of the shaft and registering all resultant PIV vector fields to a common shaft location corrected phase-dependent shaft procession (slight run-out on the cantilevered turbine shaft). Because of parallax and differences in the index of refraction between air and water, the imaged center of the turbine shaft does not correspond to the center of rotation of the turbine at the imaging plane. Therefore, we determined a best-fit location of the center of rotation in each FoV by manually fitting blades to the masked regions. Second, with the center of rotation located, the flow fields were rotated to the blade-centric coordinate system by locating the turbine blade in each $\vec{V}$ field and rotating the entire field to a common blade position. Third, after rotation, a constant crop boundary and common, segment-specific, mask were applied to each frame, and the relative velocity fields with respect to the blade were computed as the vector sum of $\vec{V}$ with the blade tangential velocity component, $r\omega$. The segment-specific mask was a function of λ only and was formed by combining all the phase-specific masks in a specific segment. Finally, the cropped fields were interpolated to a common grid relative to $C/4$. The cropped relative velocity fields, $\vec{\mathbf{\Phi}}(\lambda, \theta, n, x, y) = [u_{rel}(\lambda, \theta, n, x, y)\ ,\ v_{rel}(\lambda, \theta, n, x, y)]$ within each S_k are functions of, λ, θ, and n.

3.2.4 Correlating Turbine Performance and Flow-field Variability with Hierarchical Clustering

Cycle-to-cycle variations are present in performance and flow fields, but the correlation between the two is not obvious *a priori*. For example, if flow fields are observed in isolation, the significance of the observed flow structures on turbine performance is unknown. Throughout this work, we use "correlation" in a qualitative sense as we do not formally compute correlation coefficients. The flow fields are high-dimensional and a reduced order representation of $\vec{\mathbf{\Phi}}$ is needed to compactly describe cycle-to-cycle variation. Clustering with a PCA pre-proccesor allows us to do so while considering all of the flow-field dynamics (and the interplay between them) in an unsupervised manner without relying on hand-engineered metrics. Here we describe the flow-field clustering pipeline used for each flow segment. Using this pipeline, we correlate the variability between the simultaneously captured performance and flow fields.

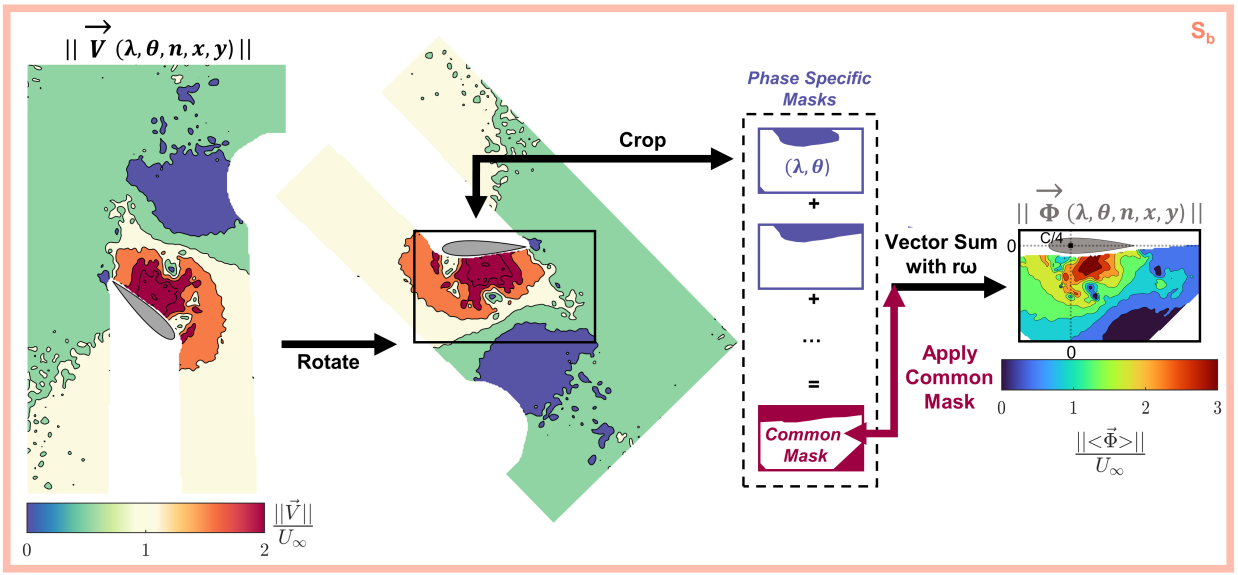

Figure 3.5: Overview schematic of the flow-field rotation pipeline. The center of rotation between the different fields of view is aligned, then the fields are rotated and cropped into a common blade-centric reference frame. A common mask between all the fields of view in a flow segment is applied and the velocity fields relative to the blade are calculated.

Flow-field PCA Pre-processor

Figure 3.6 describes the flow-field clustering pipeline. Here the PCA pre-processor enables clustering of all the dynamics using a low-dimensional subspace that is interpretable and weighted by contribution to overall velocity variance.

PCA Setup: PCA represents the dynamics of complex data sets as the linear summation of orthogonal modes ranked by the amount variance in the data they describe [69]. The singular value decomposition (SVD) is used to compute the PCA modes for a data matrix $\boldsymbol{A}_{\#}$ as

$$\boldsymbol{A}_{\#} = \boldsymbol{\phi}\boldsymbol{\sigma}\boldsymbol{a}^{*}. \tag{3.1}$$

where the PCA modes are columns of $\boldsymbol{\phi}$, the singular values, which quantify the contribution of

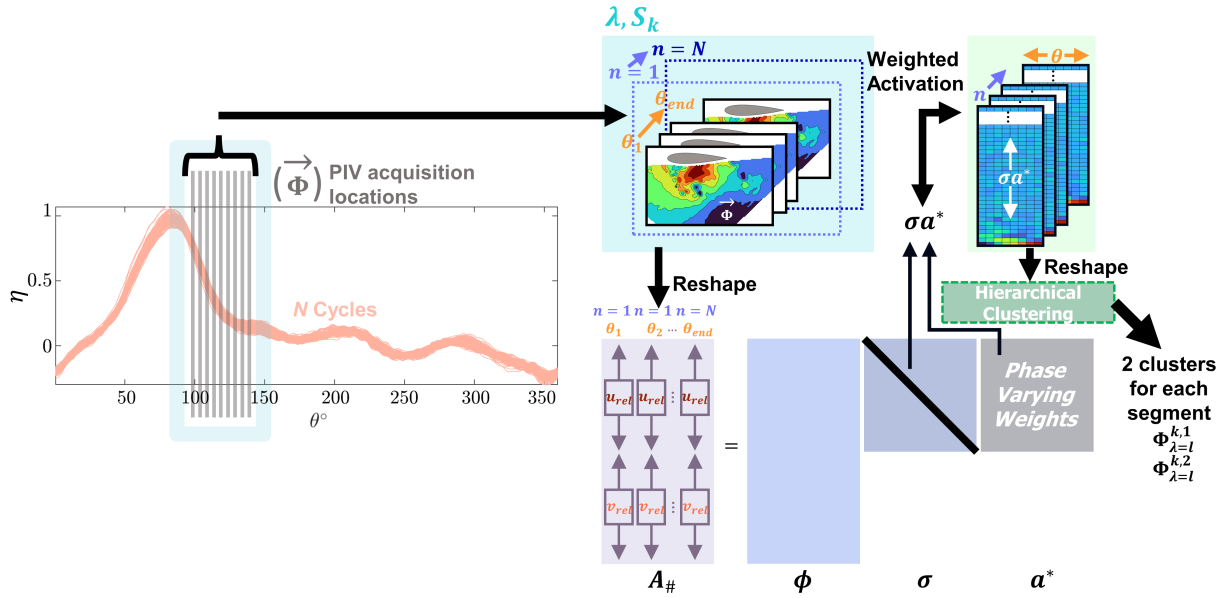

Figure 3.6: Overview of the flow-field clustering pipeline. Everything upstream of the hierarchical clustering is considered an element of the PCA pre-processor. This involves performing a singular value decomposition on the relative velocity fields in the blade-centric reference frame. The weighted activations (multiplication of the singular values and the phase-varying weights) are then separated by cycle. For each flow segment, the hiearchical clustering algorithm identifies two clusters from this population of cycles.

each mode, are diagonals of $\boldsymbol{\sigma}$, and the phase evolution of the modes make up the rows of $\boldsymbol{a}^*$. Here $*$ denotes the matrix transpose and # specifies a specific data matrix. The percentage of the flow-field variance described by a specific mode, ϕ_j, is quantified using the corresponding singular value σ_j, as $\Psi_j = \frac{\sigma_i}{\sum_{j=1}^{J}\sigma_j}$ where J is the total number of modes (smallest dimension of $\boldsymbol{A}_\#$).

Here, each $\boldsymbol{A}_\#$ is made up of reshaped $\vec{\boldsymbol{\Phi}}$ column vectors, u_{rel} stacked on v_{rel}. Any missing values (from the removal of spurious PIV vectors during processing) are linearly interpolated. A common mask is defined for each $\boldsymbol{A}_\#$ as the union of the segment-specific masks. Any data in the common mask region is completely removed ahead of the PCA processing. The presence of the shadowed regions meant a common mask across all θ (sum of all the segment-specific masks) would

occlude the majority of the FoV from analysis, so different segments, S_k, at each λ were strategically grouped to maximize data yield. This results in five distinct PCA computations of $\boldsymbol{A}_{\#}$ (Figure 3.4). The columns of each $\boldsymbol{A}_{\#}$ were sorted chronologically $[(n = 1, \theta_1), (n = 1, \theta_2)...(n = N, \theta_{end})]$ with the row-wise mean subtracted prior to SVD decomposition.

Computing Weighted Activation Pictures: To compactly describe how the dynamics evolve within a rotation, "weighted activation pictures" in the PCA subspace are constructed as $\boldsymbol{\sigma a}^*$. This multiplication may also be interpreted as the projection of each $\vec{\boldsymbol{\Phi}}$ onto the PCA basis, and encodes both the dominance and phase evolution of all the dynamics (PCA modes) of the system into lower-dimension representations for the hierarchical clustering algorithm. The result of this multiplication is 139 weighted activation pictures (one for each n) in each S_k. Each "picture" is composed of column vectors of the individual weighted activation profiles across all of the computed PCA modes. The individual weighted activation profiles are functions of θ, and describe the dominance of each mode across the range of θ included in each S_k. The weighted activation profiles associated with a mode, ϕ_j, are denoted as a_j.

Flow-field Clustering

After the PCA pre-processor, each $\vec{\boldsymbol{\Phi}}$ field is represented in a low-dimensional form suitable for clustering. While a few of the $\boldsymbol{A}_{\#}$ contained multiple S_k (i.e., common PCA modes were calculated for segment pairs as shown in Figure 3.4), each S_k was clustered separately after PCA pre-processing. This approach was taken because each S_k is an independent data set (e.g., $n = 1$ in S_a is unrelated to $n = 1$ in S_b). The weighted activation pictures in each S_k (each weighted activation picture encoding the flow-field dynamics over 1 cycle), were reshaped into column vectors and sorted into one of two clusters via a hierarchical clustering algorithm utilizing a Ward linkage method (employing a Euclidian distance metric) to minimize variance within a cluster [88]. We utilized the implementation within the MATLAB "clusterdata" function. From this, each of the 139 turbine cycles for each flow segment are associated with one of two clusters. Two clusters were prescribed because this corresponded to the maximum number of clusters that produced unique cluster-averaged weighted activation profiles (phase average of all profiles within a cluster). In

other words, if more than two clusters were prescribed, two or more of the cluster-averaged profiles were almost identical.

Cluster Assignments

After flow-field clustering, we have a set of cluster assignments in each S_k (Figure 3.6). We can use these cluster assignments to evaluate ties between the flow fields, $\vec{\mathbf{\Phi}}$, and performance, η, associated with the $\vec{\mathbf{\Phi}}$ clusters. This basis also allows us to investigate ties between the performance and flow-field variability and the potential sources of this variability by considering both conditional-averages and individual trajectories of different parameters based on flow-field cluster assignment. As shown in Figure 3.6, cluster assignments are denoted as $\Phi^{k,c}_{\lambda=l}$, where k is the segment designation (a-e), c is the cluster number (1 or 2), and l is the tip-speed ratio set point. Conditional-averages across n, based on cluster assignment, for any variable X (e.g., η, $\vec{\mathbf{\Phi}}$) within one S_k are expressed as $\langle X|\Phi^{k,c}_{\lambda=l}\rangle$. In cases where examining individual trajectories of X within a cluster is preferred, an equivalent set notation, $\{\}$, denotes the subset of cycles of X assigned to the specified cluster. For example, a set of individual η trajectories based on $\vec{\mathbf{\Phi}}$ clusters is written as

$$\eta_{\Phi}(\lambda, \theta, n, k, c) = \{\eta(\lambda, \theta, n)|\Phi^{k,c}_{\lambda=l}\}. \tag{3.2}$$

While the clusters are agnostic to η, we manually assign cluster 1 (i.e., $c = 1$) to the cluster with a higher associated time-averaged performance, $\bar{\eta}$, for full revolutions. To quantify the statistical significance of the identified clusters, we utilized a two-sided Wilcoxon Rank Sum test ([89], MATLAB "ranksum" function) with a 5% significance level. The null hypothesis is that the populations of X contained in each cluster are drawn from the same continuous distribution and have equal medians. Rejection of the null hypothesis means the populations of X contained in each cluster are statistically significant.

Considering how individual trajectories or cluster conditional-averages differ from the phase-averages over all n can illuminate cluster-specific characteristics. This is done for both performance and flow fields. Conditional performance perturbations, η'_{Φ}, are defined as the differences between the individual performance trajectories in each cluster and the phase-averaged performance (average

for a single operating condition and azimuthal position across all cycles), $\langle\eta(\lambda,\theta,n)\rangle$, within the same S_k. They are computed as

$$\eta'_\Phi(\lambda,\theta,n,k,c) = \eta_\Phi(\lambda,\theta,n,c) - \langle\eta(\lambda,\theta,n)\rangle \tag{3.3}$$

These perturbation quantities help highlight where the clusters are performing better or worse than the phase-average.

Conditional difference fields, Φ', highlight how the conditional-averaged velocity magnitude fields, $||\langle\vec{\mathbf{\Phi}}|\Phi^{k,c}_{\lambda=l}\rangle||$, differ from the phase-averaged fields, $||\langle\vec{\mathbf{\Phi}}\rangle||$. As with the phase-averaged fields, the conditional-averaged velocity magnitudes are computed from the component averages (i.e., $||\langle u_{rel}\rangle, \langle v_{rel}\rangle||$). The conditional difference fields, computed at each point in space (x,y), are defined as

$$\Phi'_\Phi(\lambda,\theta,k,c,x,y) = ||\langle\vec{\mathbf{\Phi}}|\Phi^{k,c}_{\lambda=l}\rangle|| - ||\langle\vec{\mathbf{\Phi}}\rangle||. \tag{3.4}$$

3.3 *Results*

We explore the three potential sources of cycle-to-cycle performance variability: variations in near-blade flow fields, variations in inflow velocity, and hysteresis from previous cycles. Section 3.3.1 describes the statistical variability in performance and flow fields, highlighting the influence of tip-speed ratio and the blade's phase in the rotation. In Section 3.3.2, we utilize flow-field clustering to correlate cycle-to-cycle performance and flow-field variability. We conclude with a discussion of the impact of the freestream velocity perturbations in Section 3.3.3 and hysteresis in Section 3.3.4.

3.3.1 Performance and Flow-field Variability

The tip-speed ratio affects both time-average performance and the properties of cycle-to-cycle variation around that average, as visualized in Figure 3.3. Mean performance and its variability both increase with tip-speed ratio but performance reaches a maximum near $\lambda = 2.9$, while variability continues to increase at higher tip-speed ratios. For the remainder of this work, we focus on two cases: $\lambda = 1.5$ (sub-optimal performance) and $\lambda = 2.5$ (near-optimal performance) which

exhibit differences in both time-averaged performance and cycle-to-cycle variability. Both cases are relevant to turbine operation because maximizing efficiency (optimal tip-speed ratio) is a control objective when the freestream velocity is below the turbine's rated speed, while the sub-optimal case corresponds to a strategy for shedding power above the rated speed. We note that the larger variation associated with $\lambda = 2.5$ is due in part to the larger performance and address this later by normalizing by the time-averaged performance as the coefficient of variation.

A defining feature of cross-flow turbine performance is periodic variation within a cycle (i.e., performance variation with θ). The polar representations of performance and flow fields for both tip-speed ratios in Figure 3.7 show that the largest cycle-to-cycle variation in phase-specific performance occurs in the upstream sweep around the performance peak ($\theta = 30° - 135°$ for $\lambda = 1.5$ and $\theta = 60° - 165°$ for $\lambda = 2.5$). In agreement with time-averaged performance (Figure 3.3), the $\lambda = 1.5$ case exhibits less cycle-to-cycle variability during the smaller, narrower performance peak (lower time-averaged performance) than the $\lambda = 2.5$ case. The phase-specific variation in performance is appreciable, but secondary in comparison to the range in performance over a cycle. For both tip-speed ratios, the bivariate distributions of performance are unimodal at each θ, suggesting that this local variation is adequately described by the mean and a descriptor of the spread [61].

The phase-averaged flow fields of global velocity magnitude around a cross-flow turbine (Figure 3.7) depend strongly on blade position and tip-speed ratio. Overall, dynamic stall severity and turbine performance are inversely proportional for the two cases (i.e., the higher tip-speed ratio decreases stall severity and increases performance). Specifically, coherent structures from dynamic stall are more apparent for the sub-optimal case, $\lambda = 1.5$, than for the near-optimal case, $\lambda = 2.5$. In comparing the flow fields with turbine performance, we see that for $\lambda = 1.5$, the performance peak coincides with formation, growth, and shedding of the dynamic stall vortex. On the other hand, for $\lambda = 2.5$, the flow remains primarily attached until maximum performance, beyond which we observe increasing separation at the trailing edge. For both tip-speed ratios, performance is at a minimum during the downstream sweep, consistent with lower incident velocities due to extraction of momentum from the flow during the "power stroke". The flow fields are in qualitative agreement

with dynamic stall theory (Section 2.2), as well as prior experiments [11, 13, 53] and simulation [9, 16] for cross-flow turbines. Because the lower tip-speed ratio leads to a wide oscillation in angle of attack, the $\lambda = 1.5$ case experiences "deep" dynamic stall. This is evidenced by a strong dynamic stall vortex that is shed before the maximum nominal angle of attack (Figure 3.7a), as well as prolonged post-stall flow separation. In contrast, for $\lambda = 2.5$, the foil experiences only "light" dynamic stall with smaller vortex structures, limited flow separation until near the maximum nominal angle of attack, and faster post-stall flow recovery.

To characterize the cycle-to-cycle variation in the flow fields, we compute the standard deviation fields, s_Φ. These are presented normalized by the mean, as the coefficient of variation, to facilitate comparisons with performance variability. Since the flow-field data is sparse in θ, we cannot calculate an accurate time-average, so we define the flow-field coefficient of variation as $CV_\Phi(\lambda, \theta, x, y) = \frac{s_\Phi}{\tilde{\phi}}$, where $\tilde{\phi}$ is the mean of all the PIV vectors collected at a given phase. Figure 3.8 demonstrates the spatial extent of flow-field variability as a function of θ and λ. The flow-field coefficient of variation ranges from 1% to 110% and is truncated in the figure for visualization. During the early portion of the cycle (locations i and ii, S_a), variability is confined to a region on the order of the foil thickness close to the blade and in the wake (Figure 3.8a,b) for both tip-speed ratios. The two cases diverge around $\theta = 90°$ (beginning of S_b). There, for $\lambda = 1.5$, flow-field variability expands in the vicinity of the dynamic stall vortex. In contrast, at the same θ, variability for $\lambda = 2.5$ remains confined to the blade wake and the region of separated flow at the trailing edge. By the end of the cycle (location v, S_e), for $\lambda = 2.5$, variation is once again primarily limited to the blade wake, while, for $\lambda = 1.5$, we observe high variability in a large region of separated flow (locations iv-v, $S_c - S_e$). We can compactly visualize the trends across phase by summation of CV_Φ in space (i.e., $\sum CV_\Phi$). As shown in Figure 3.8c, $\sum CV_\Phi$ is higher at all resolved phases for $\lambda = 1.5$ than $\lambda = 2.5$. For $\lambda = 1.5$, $\sum CV_\Phi$ increases dramatically during the growth of the dynamic stall vortex (S_b) and, for the resolved phases of the power stroke, reaches a maximum at location iii. This is in agreement with prior work that has consistently demonstrated large increases in cycle-to-cycle variation post-stall [34, 59, 67]. In contrast, for $\lambda = 2.5$, $\sum CV_\Phi$ remains relatively low during the power stroke, and the maximum variability likely occurs in a portion of the flow

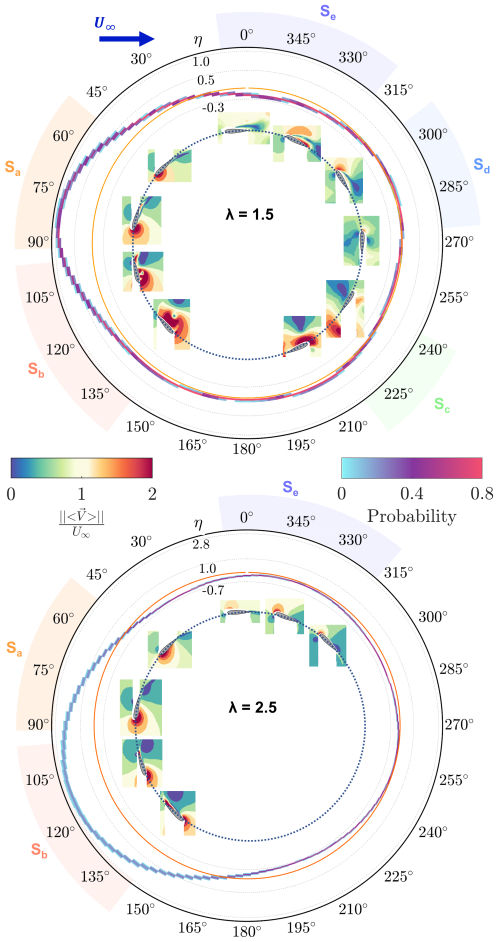

Figure 3.7: Phase-averaged coefficient of performance for a (a) deep dynamic stall case at $\lambda = 1.5$ and a (c) light dynamic stall case at $\lambda = 2.5$. The orange line corresponds to $\eta = 0$, demarcating the power producing from power consumptive phases. Inset are phase-averaged global velocity magnitude fields (normalized by the freestream velocity). Note that the blade and turbine diameter (blue dashed line) are not to scale. The velocity fields are presented in the fixed global reference frame. Shaded regions at the periphery denote the radial extent of flow segments for PIV, S_k. (b,d) Bivariate distributions of phase-specific coefficient of performance (blue-to-purple shading with 0.05 $\Delta\eta$ and 2° $\Delta\theta$).

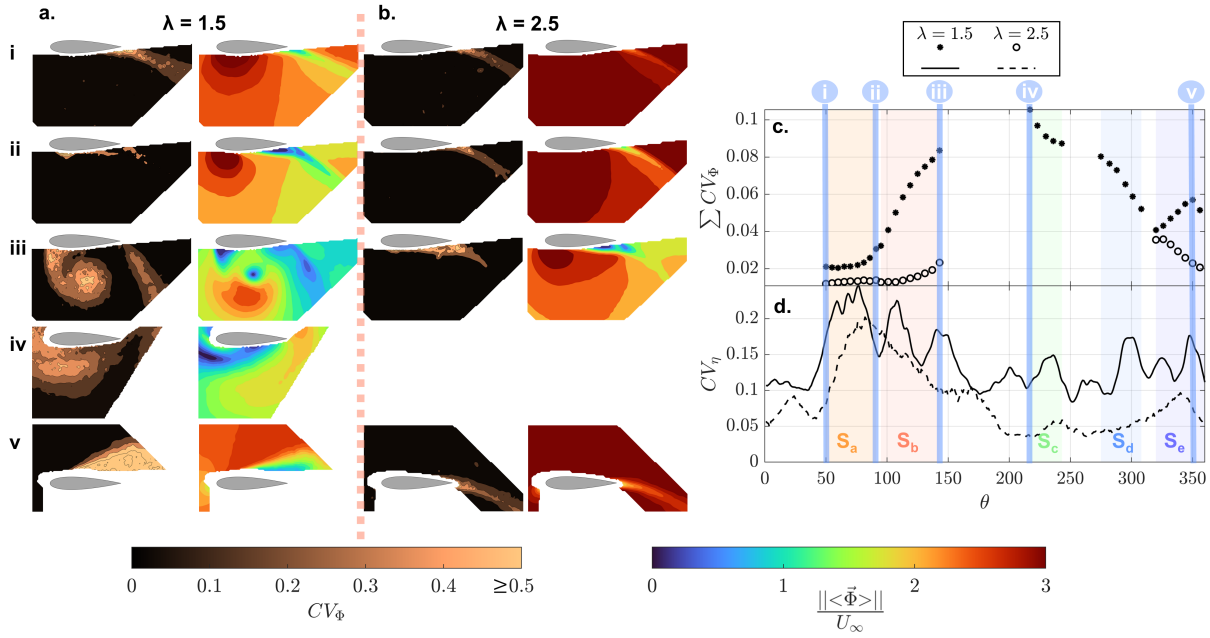

Figure 3.8: Coefficient of variation fields (colorbar has been truncated at 0.25 for visualization) at select θ for (a) $\lambda = 1.5$ (b) and $\lambda = 2.5$ and their accompanying relative velocity fields (normalized by the freestream velocity). The location of the θ positions in (a-b) are labeled in (c-d) which show the (c) sum of the coefficient of variation fields (normalized by the number of data points) (d) and the coefficient of variation for performance for both λ.

field not visualized in these experiments. For both cases, the highest observed flow-field variability occurs in the downstream sweep. In summary, cycle-to-cycle flow-field variability increases with stall severity and is concentrated around coherent structures originating from the blade or in the blade wake.

The increase in flow-field variability for the lower tip-speed ratio is expected given the higher stall severity, but is inverted from the trends in time-average and phase-specific performance variability, which are higher for $\lambda = 2.5$ (Figure 3.3 and 3.7). However, the coefficient of variation for performance, $CV_\eta = \frac{s_\eta}{\bar{\eta}}$ (Figure 3.8d), is higher for $\lambda = 1.5$ across most of the cycle, consistent

with flow-field variability. In other words, while $\lambda = 2.5$ exhibits higher absolute performance variability, the $\lambda = 1.5$ case has higher relative variability.

Finally, it is instructive to directly compare the magnitude and timing of flow-field and performance variability. Overall, we observe a non-coincidence between the performance and flow-field variability for both tip-speed ratios. For $\lambda = 1.5$, $\sum CV_\Phi$ lags CV_η, particularly in S_a (Figure 3.8c,d), which suggests that corresponding flow-field variability present during maximum performance variability likely occurs too close to the blade to be resolved by these PIV measurements. It is also possible that our interpretation is influenced by the $\sum CV_\Phi$ formulation which equally weights the flow-field variability regardless of proximity to the blade. For $\lambda = 2.5$, we similarly see the $\sum CV_\Phi$ is minimal during the phases of maximum performance variability. For both tip-speed ratios, the observed high flow-field variability in the downstream sweep is associated with lower relative performance variability further in Section 3.3.2).

3.3.2 Flow-field Clusters and Their Associated Performance

Due to the non-coincidence between the performance and flow-field variability, we must employ a different approach to better understand relationships between the observed performance and flow-field variability. By utilizing the flow-field clusters and their associated, cycle-specific performance trajectories, η_Φ, we are able to characterize the flow-field and performance variability more completely, as well as identify correlations between them. For this analysis, we focus on segment S_b, which encompasses the end of the power stroke for both tip-speed ratios and the shedding of a dynamic stall vortex for $\lambda = 1.5$.

Figure 3.9 summarizes the comparison of the flow-field clusters for segment S_b and their corresponding performance trajectories for the two tip-speed ratios. As mentioned in Section 3.2.4, we designate cluster 1 to be the higher-performing cluster in terms of time-averaged performance. The conditionally-averaged difference fields (i and ii) highlight the deviation between the cluster conditionally-averaged fields and the phase-averaged fields (iii). The performance trajectories (iv) and their perturbations from the phase-average (v) for each cycle reveal correlations between performance and the flow-field clusters. For both tip-speed ratios, the conditionally-averaged

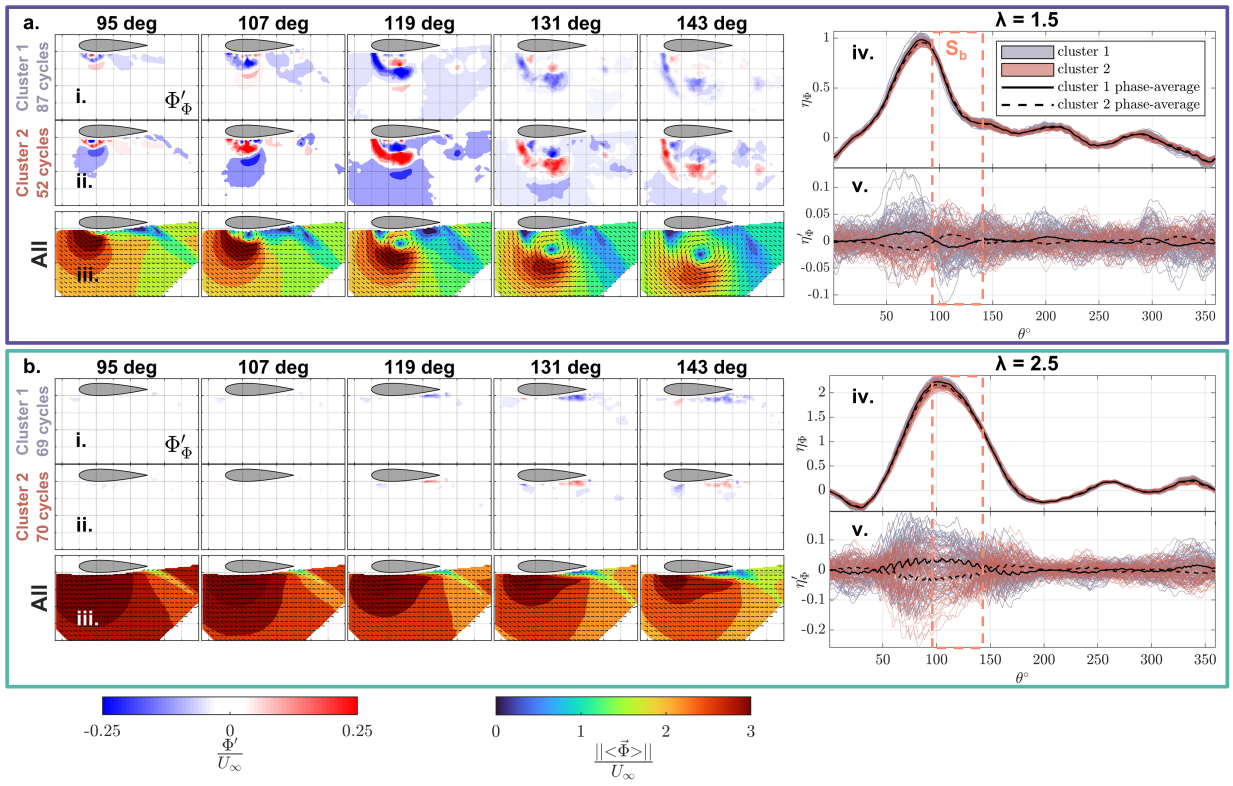

Figure 3.9: Clustering analysis overview for for (a) $\lambda = 1.5$ (b) and $\lambda = 2.5$. (i,ii) Cluster conditional difference fields and (iii) phase averages for selected θ, with (iv) corresponding performance trajectories and (v) performance perturbations. The grid spacing in (i), (ii) and (iii) is $C/4$. In (iv), each line is colored by cluster assignment and the black lines represent the cluster conditional-averages for performance or performance perturbations (Equations 3.2 and 3.3). The dashed rectangles denote the θ range (S_b) where the flow fields in (i),(ii) and (iii) were captured.

difference fields reveal opposing behaviors between the clusters (e.g., regions of lower-than-average relative velocities in one cluster are coincident with regions of higher-than-average relative velocities in the other). In line with the coefficient of variation fields (Figure 3.8), the differences are more pronounced for $\lambda = 1.5$ than for $\lambda = 2.5$. Yet, for both tip-speed ratios, performance trajectories are separated by their associated flow-field clusters and exhibit opposing behaviors around the phase

average (iv and v). More significantly, the flow-field clusters for both tip-speed ratios are correlated with differences in maximum performance (Figure 3.9iv), even though S_b does not fully span the performance peak. This suggests that the flow-field variability in S_b stems from variability in the growth and shedding of hydrodynamic structures that originate from the blade, but are unresolved in segment S_a due to their proximity to the surface. Finally, we note that, for $\lambda = 1.5$, the cluster-averaged performance perturbations reveal that cluster 1 and cluster 2 alternate phases of superior performance over the cycle, even though cluster 1 out-performs cluster 2 on a time-averaged basis.

For brevity, discussion of the relationship between the flow-field clusters in segments other than S_b and their associated performance is presented in supplemental info. In brief, despite the apparent contradiction between relatively high flow-field variability and relatively low performance variability in the downstream sweep (Figure 3.8), the flow-field clusters for segments in the downstream sweep are still connected to time and phase-averaged performance.

We now dive deeper into the two tip-speed ratio cases for segment S_b to describe how the flow fields differ between clusters and their relationship with performance. We primarily focus on the $\lambda = 1.5$ case since it exhibits stronger flow-field variability. We then utilize the $\lambda = 2.5$ case to highlight how, despite the lower flow-field variability and limited near-blade resolution, we are still able to extract useful insight from the flow-field clusters.

$\lambda = 1.5$

For this tip-speed ratio, the deep dynamic stall results in growth and shedding of a dynamic stall vortex in segment S_b. Difference fields for the cluster with higher time-averaged performance, cluster 1, highlight primarily lower-than-average velocities, with only small regions of higher-than-average velocity. The opposite behavior is seen for the poorer performing cluster, cluster 2. These velocity differences suggest several possible mechanisms: the dynamic stall vorticies for the two clusters differ in strength, in their location with respect to the blade (a consequence of different shedding timing), or both.

The difference in time-averaged performance between the two clusters is comparatively small (1.1% with respect to the time-average), but, as apparent in Figure 3.9a-iv, the performance peak for

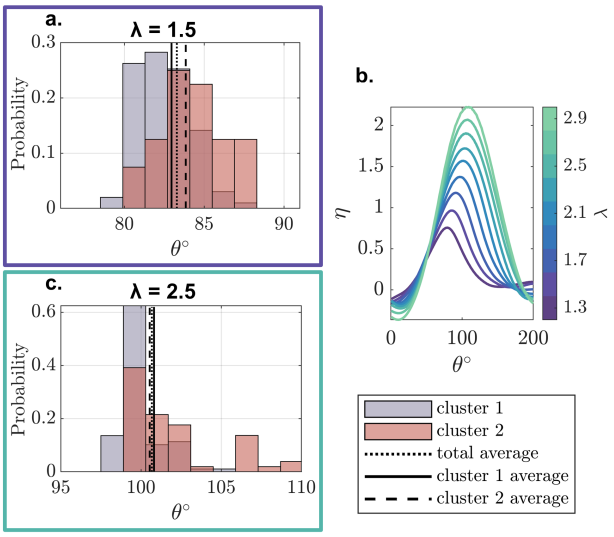

Figure 3.10: Histograms of cycle-specific phase associated with maximum performance for (a) $\lambda = 1.5$ (c) and $\lambda = 2.5$. (b) Phase-averaged coefficient of performance for select tip-speed ratios.

cluster 1 is slightly higher in amplitude and occurs slightly earlier in the cycle. The shift in phase of maximum performance is highlighted in Figure 3.10a. On average, maximum performance occurs at $\theta \approx 83°$ for cycles in cluster 1 and at $\theta \approx 83.9°$ for cycles in cluster 2. The distributions of the phase of maximum performance are statistically significant, as per the rejection of the null hypothesis for the Wilcoxon rank sum test (Section 3.2.4). These differences in the timing and amplitude of the performance peak between the clusters counter the phase-average trends over all tip-speed ratios (Figure 3.10b) where low tip-speed ratios have a performance peak earlier in the cycle and lower maximum and time-averaged performance.

To gain further insight into how flow fields differ between the two clusters, we first consider modal analysis. A key benefit of the PCA pre-processor is the ability to interpret the resulting clusters through their modes and modal coefficients. The directions of the largest variance in the data are described by the modes and sorted by the singular values. Thus the first mode describes the fluid dynamics with the highest variability and the variation described decays as mode number increases.

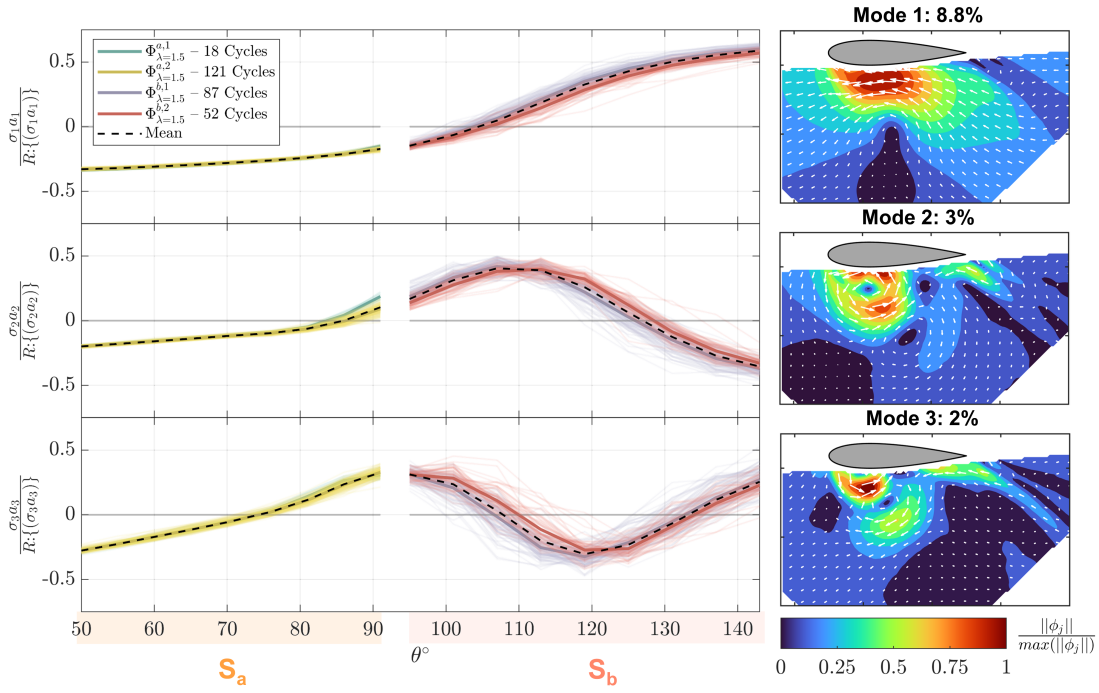

Figure 3.11: (left) Weighted activation profiles across each cycle, colored by the flow-field cluster assignments for $\lambda = 1.5$ are presented for S_a and S_b. The opaque thick lines are the conditional-averages for each cluster and the black dashed line is the phase-average over all cycles. (right) Magnitude fields for the first three modes with variance explained for each mode noted.

By considering the modal flow fields and their accompanying weighted activation profiles, we can identify the dynamics most associated with the variation and how their contribution changes with blade position and/or between clusters.

Figure 3.11 shows the first three modes and the variability in their weighted activation profiles within segments S_a and S_b. These three modes describe 14% of the flow-field variance within these segments (see supplementary info for a plot of the singular values). We interpret modes 1 and 2 as related to dynamic stall vortex shedding while mode 3 is attributed to near-blade vortex dynamics occurring earlier in the cycle. In this interpretation, mode 1 represents shedding dynamics that occur once the vortex core is at least a foil thickness away from the blade, while mode 2 occurs

earlier in the shedding process. The high variance explained by mode 1 is consistent with the velocity magnitude (Figure 3.8a and 3.9a-iii) and coefficient of variation fields (Figure 3.8a), which are dominated by the shedding of the dynamic stall vortex.

We observe that the weighted activation profiles for these three modes are well-converged in S_a but diverge between the flow-field clusters in S_b. In S_b, the better-performing cluster, cluster 1, has larger weighted activations in mode 1 and the weighted activations are shifted earlier in phase for mode 2. For mode 3, both clusters have similar mean-weighted activations everywhere except for $\theta = 90° - 120°$. This is consistent with low flow-field variability in segment S_a and increased variability in S_b (Figure 3.8c and Figure 3.9). At $\theta = 119°$, where the difference fields are most distinct, we see that the higher-than-average velocities closer to the blade for cluster 1 are captured by the higher mode 1 weighted activation. On the other hand, the lower mode 2 weighted activation for cluster 1 at this position captures the lower-than-average velocities farther from the blade.

To establish some physical intuition for the differences between the two clusters in segment S_b, we explore the chord-wise and chord-normal position of the dynamic stall vortex, (DSV_C and $DSV_\perp$ respectively), and the reversed flow fraction, U_Φ^{rev} (Figure 3.12a-c). As we do not have sufficient resolution to resolve the radial extent of the core of a more nuanced vortex model, the position of the vortex core is defined as the location of the maximum value of the swirling strength in individual flow fields reconstructed with 30 PCA modes. The mode truncation removed incoherent noise [69] resulting in cleaner swirling strength fields that significantly improved tracking performance.

For $\theta = 113° - 125°$, the chord-wise and chord-normal vortex positions are statistically higher for cluster 1 and $DSV_\perp$ slope changes earlier for cluster 1. This is indicative of earlier vortex shedding. These results are consistent with [67] who showed for a pitching foil that clusters based on pressure data were able to reveal earlier shedding of a dynamic stall vortex.

An increase in reversed flow fraction can indicate more flow separation on the blade and therefore more severe stall. We define this quantity as

$$U_\Phi^{rev}(\lambda, \theta, n, k, c) = \frac{\sum [\{u_{rel} | \Phi_{\lambda=l}^{k,c}\}\langle 0]}{NxNy} \times 100, \tag{3.5}$$

where the [ ] brackets represent Iverson Bracket Notation which, similar to the Kronecker Delta,

returns a value of 1 when the statement in the brackets is true and a value of 0 when false. Cluster 1 exhibits more reversed flow everywhere in S_b (statistically significant). This is consistent with earlier separation and the possibility that cluster 1 cases have stronger dynamic stall vorticies, as evidenced by the higher-than-average velocities near the blade.

In summary, we see clear differences between the clusters for modes that represent various periods of the dynamic stall process, and have shown that the dynamic stall vorticies have different velocity distributions and are shed at different times. Specifically, cycles in cluster 1 have better performance, more reversed flow, higher near-blade velocities in the dynamic stall vortex, and dynamic stall vortex cores that are further from the blade than cluster 2. These fluid dynamics are indicative of an earlier and potentially stronger stall which is consistent with the maximum performance occurring earlier in the cycle (Figure 3.10).

$\lambda = 2.5$

The higher tip-speed ratio case presents an opportunity to test the flow-field clustering method when there is less apparent flow-field variability due to the lighter dynamic stall and weaker vortex shedding that remains closer to the blade. Despite this, the difference in time-averaged performance between the two flow-field clusters is 3% with respect to the total time-average. This is higher than for $\lambda = 1.5$ and consistent with the higher absolute performance variability for $\lambda = 2.5$. Referring once again to Figure 3.9, the amplitude of the performance peak for the better-performing cluster, cluster 1, is slightly higher, but, unlike for $\lambda = 1.5$, there is no apparent phase shift (Figure 3.10c). This is consistent with the convergence in the phase of maximum performance at higher tip-speed ratios in Figure 3.10b. Despite the relatively low variability, the flow-field clustering results in lower-than-average velocities at the trailing edge of the blade and slightly higher-than-average velocities near the leading edge for cluster 1, while the opposite is true for cluster 2.

The first three modes capture nearly 12% of the total variance and depict spatial structures on the order of a foil thickness that remain close to the blade and in the wake (Figure 3.13). We interpret mode 1 as pertaining to attached flow on the blade throughout segment S_a, followed by an increase in reversed flow at the trailing edge as $\sigma_1 a_1$ crosses zero (representing a change in sign

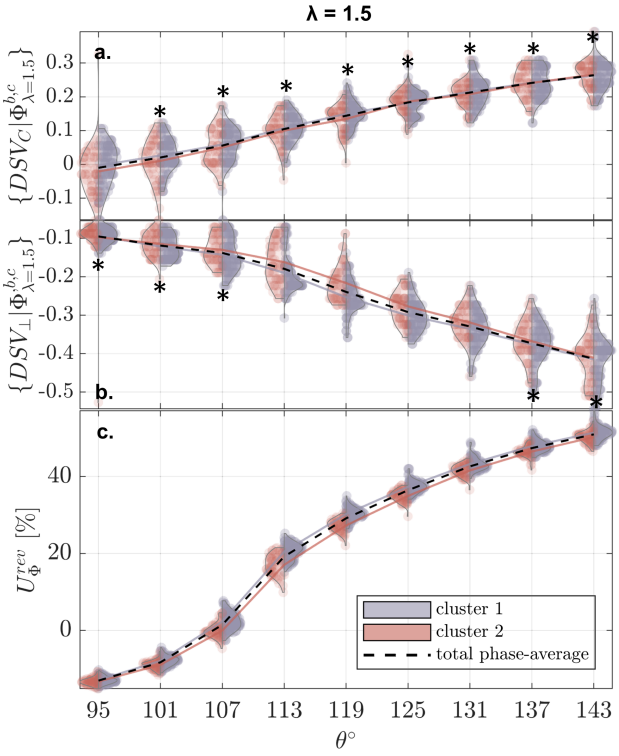

Figure 3.12: Location of the dynamic stall vortex core in the chord-wise direction, DSV_C, (a) and in the chord-normal direction, $DSV_\perp$ (b) for both clusters. Vortex positions are normalized by the chord length, C. (c) Reversed flow fraction. The solid lines are the conditional-averages associated with each cluster and the violin plots (*violinplot* MATLAB function from [2]) at each θ combine box plots and smoothed histograms to highlight the underlying distribution of the populations. The $*$ denote phases where the result of the Wilcoxon rank sum test show we cannot reject the null hypothesis that the clusters are samples from continuous distributions with equal medians at the 5% significance level (i.e., the difference between the two distributions may not be statistically significant).

of the mode), and the change in direction and magnitude of the relative velocity (Figure 3.9b-iii). Mode 2 represents increased flow along the entire blade when the weighted activations are positive, but enhanced separated flow at the trailing edge when negative. Similarly, mode 3 describes subtle

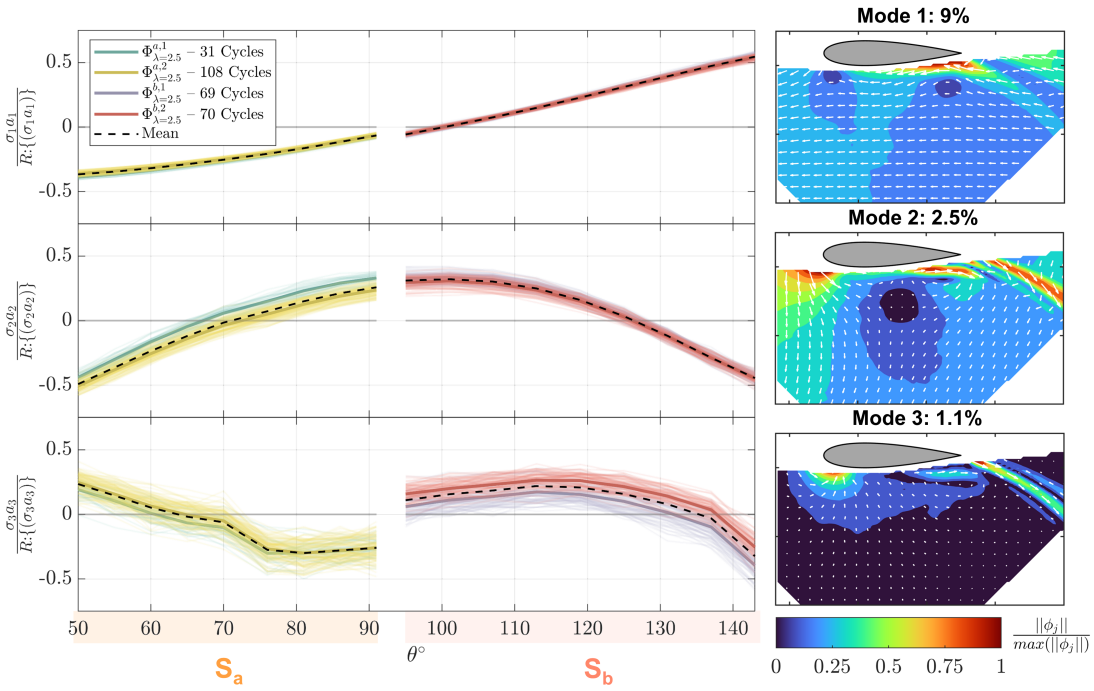

Figure 3.13: (left) Weighted activation profiles across each cycle, colored by the flow-field cluster assignments for $\lambda = 2.5$ are presented for S_a and S_b. The opaque thick lines are the conditional-averages for each cluster and the black dashed line is the phase-average over all cycles. (right) Magnitude fields for the first three modes with variance explained for each mode noted.

changes in velocities along the blade. The discontinuity in mode 3 between segments is not likely the result of a rapid change in the dynamics. It is instead most likely a consequence of uncertainty in establishing the blade position between segments, which manifests as a slight misalignment between flow fields of different segments during the translation to the blade-centric reference frame. The $\lambda = 2.5$ case is more sensitive to this error because the energetic dynamics are located adjacent to the blade, and therefore more susceptible to occlusion by the common mask, much more so than for $\lambda = 1.5$. The weighted activation profiles reveal minimal deviations between the clusters, with the exception of mode 2 in S_a and mode 3 in S_b. For mode 3, the relatively lower weighted activation for cluster 1 captures the lower-than-average trailing edge velocities. These lower velocities are

indicative of more flow separation (theoretically limiting lift production) which contradicts the higher time-averaged performance for the cluster.

In summary, the $\lambda = 2.5$ case exhibits less flow-field variability in comparison to $\lambda = 1.5$, as well as more muted conditional-average difference fields and modes, and less distinct cluster-specific weighted activation profiles. Despite this, the flow-field clusters and their associated performance are distinct and meaningful.

3.3.3 Impact of Freestream Velocity Perturbations

For both tip-speed ratios, we observe a dichotomy between the flow-field and performance trends. The flow fields for cluster 1 show evidence of earlier and potentially stronger stall, but cluster 1 has higher time-averaged performance. While the flow-field and performance differences between the clusters could be the result of the stochastic dynamic stall process, an alternative hypothesis is that these variations are the result of freestream velocity perturbations. Any changes in the freestream velocity impact both the kinetic energy available in the flow and the instantaneous tip-speed ratio. Cycle-to-cycle variation in the rotation rate is negligible (standard deviations in ω are 0.02-0.03% of the time-average), so any perturbations in the freestream will result in cycle-specific tip-speed ratios that differ from the average. Figure 3.14 demonstrates that, for both tip-speed ratios, the instantaneous freestream velocities (advection-corrected as in Section 3.2.2) are correlated with the flow-field clusters. The difference between the mean of each cluster is 1.6% and 2.1% of the time-averaged velocity for $\lambda = 1.5$ and $\lambda = 2.5$, respectively, and are statistically significant. For both tip-speed ratio cases, cluster 1 has a higher conditionally-averaged inflow velocity. As a result, the blade is effectively operating at a lower tip-speed ratio for cluster 1 cycles while also encountering more kinetic energy in the flow.

Since the coefficient of performance, η_Φ, is defined using the time-average of the cubed freestream velocity measurements acquired at the tip-speed ratio set point, it does not account for cycle-to-cycle inflow variability. Consequently, we consider a cluster-specific kinetic power, proportional to the conditional-average of the cubed freestream velocities associated with each

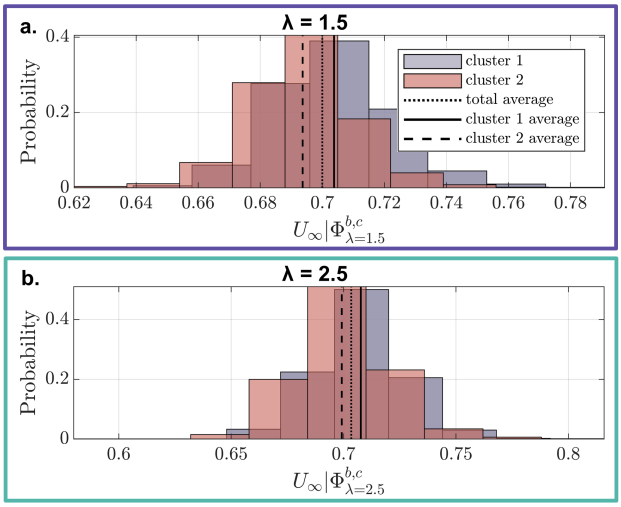

Figure 3.14: Histogram of freestream velocities for clusters derived from flow fields in S_b at (a) $\lambda = 1.5$ and (b) $\lambda = 2.5$.

cluster. Utilizing this, a cluster-specific coefficient of performance, η^*_Φ, is defined as

$$\eta^*(\lambda, \theta, n, k, c) = \frac{P}{\frac{1}{2}\rho\{\overline{U^3_\infty|\Phi^{k,c}_{\lambda=l}}\}LD}. \tag{3.6}$$

A comparison between the performance trajectories around the peak and histograms of cycle-specific, time-averaged performance for η_Φ and η^*_Φ are presented in Figure 3.15. For $\lambda = 1.5$, both the η_Φ and η^*_Φ trajectories around the peak are statistically significant between the clusters (Figure 3.15a-i,ii). However, the locally higher λ cluster, cluster 2, outperforms cluster 1 at maximum η^*_Φ. Similarly, the time-averaged distributions for both η_Φ and η^*_Φ are statistically significant between the clusters, but cluster 2 now outperforms cluster 1. These observations are now consistent with phase-averaged (Figure 3.10a) and time-averaged (Figure 3.3) performance trends across tip-speed ratios.

The results are much the same for the $\lambda = 2.5$ case. In comparison to $\lambda = 1.5$, we observe a better collapse in $\bar{\eta}^*_\Phi$ and η^*_Φ for the $\lambda = 2.5$ case despite its higher performance variability. This is likely because the angle of attack profiles become less dependent on the tip-speed ratio as the tip-speed ratio increases (Figure 2.1). This means that, nominally, the sensitivity of the

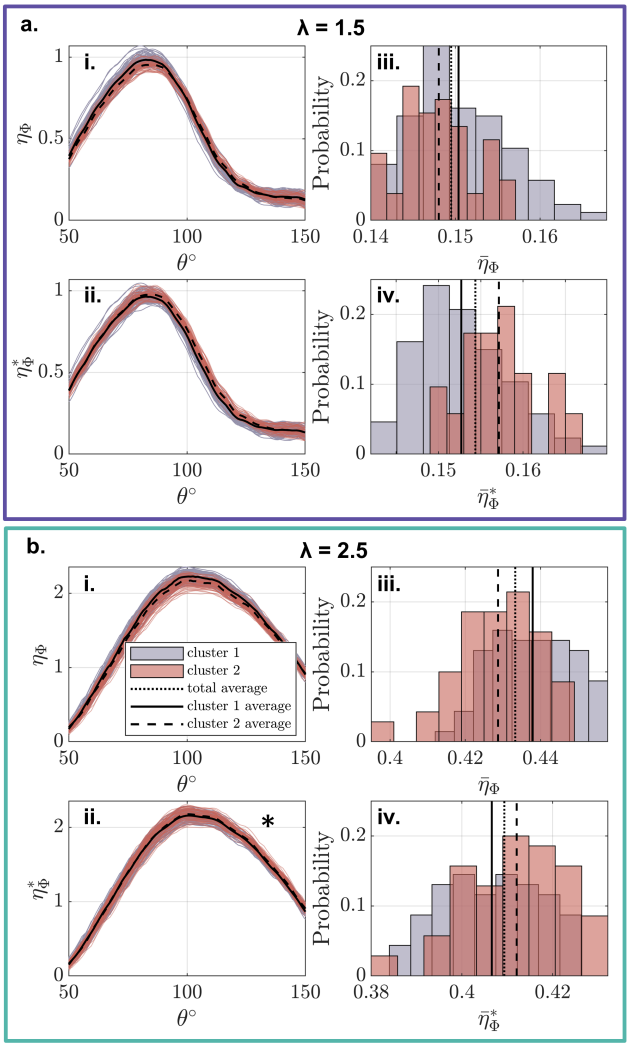

Figure 3.15: (a) $\lambda = 1.5$ and (b) $\lambda = 2.5$. Individual (i) coefficient of performance and (ii) cluster-specific coefficient of performance trajectories around the peak for the two clusters. The solid lines are the phase-average for cluster 1 and the dashed lines are the phase-average for cluster 2. Cluster-specific histograms of (iii) cycle-specific, time-averaged coefficient of performance and (iv) time-averaged, cluster-specific coefficient of performance.

blade kinematics to inflow perturbations is inversely proportional to the tip-speed ratio. As a consequence, the fluid dynamics for $\lambda = 2.5$ are potentially less sensitive to inflow perturbations

than for $\lambda = 1.5$.

In summary, for both tip-speed ratios, performance based on a cluster-specific freestream kinetic power, η^*_Φ, confirms the hypothesis that the observed flow-field and performance differences between clusters are primarily caused by inflow velocity variations. This performance dependency on the inflow velocity is in agreement with the axial-flow literature which has consistently shown that turbine power output is correlated with inflow conditions [90]. Here, the increase in η_Φ observed for cluster 1 is a consequence of not accounting for the increased inflow kinetic energy, which increases turbine power output even as the actual efficiency is degraded by the lower cycle-specific tip-speed ratio. While these results suggest that it might be preferable to calculate efficiency on a cycle-specific basis, we found that this approach increases performance variability in this data set. Consequently, we find that cluster-specific performance is more robust to uncertainty in the advection correction (Section 3.2.2).

3.3.4 Cycle-to-Cycle Hysteresis

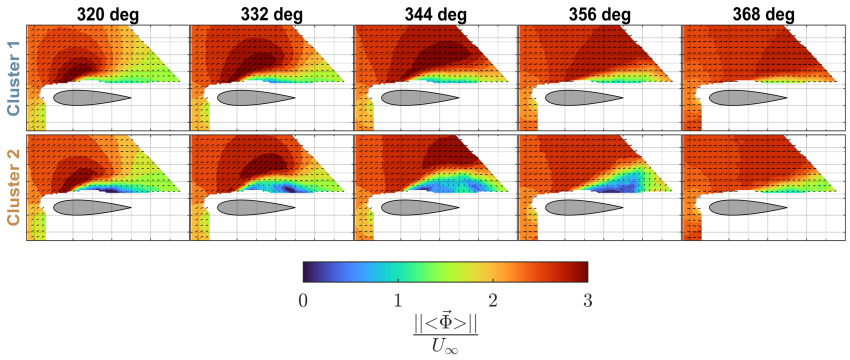

Figure 3.16: Cluster conditionally-averaged flow fields in S_e for $\lambda = 1.5$ as the blade transitions from the downstream to upstream sweep.

As previously noted (Figure 3.8c-d, Section 3.3.2), the relatively high cycle-to-cycle flow-field variation during the downstream sweep does not coincide with comparable performance variability. However, it is conceivable that flow-field variation at the end of one cycle could affect future cycles.

To explore this possibility, we consider cluster conditionally-averaged flow fields in Figure 3.16, focusing on S_e for $\lambda = 1.5$, a case with distinct differences between the two clusters. Flow recovery in cluster 2 appears slower, with more separated flow and lower velocities near the trailing edge at $\theta = 356°$. Despite this, we observe three factors that support a hypothesis of limited hysteresis between cycles. First, as the blade enters the next cycle ($\theta = 368°$), differences between the cluster 1 and cluster 2 flow fields has considerably diminished. Second, there is limited cycle-to-cycle performance variability at the beginning of the cycle ($\theta < 40°$ (Figure 3.8). Third, there is limited variation in the weighted activation profiles for the flow fields at the beginning of the next cycle (Figure 3.11, S_a). If hysteresis from the flow-field variability in the prior cycle was present, we would expect flow-field variability to persist through $\theta = 0°$ and to see attendant performance variability at the start of the cycle. Thus, it is unlikely that fluid dynamics in the previous cycle contribute to the observed variability in future cycles, especially in comparison to variation associated with the freestream velocity.

We note that this result is likely influenced by our choice of control scheme. Specifically, if turbine torque, rather than rotation rate, was the regulated quantity, the instantaneous rotation rate would vary within and between cycles, such that the blade kinematics would no longer be deterministic [86]. Under such a control scheme, we might see greater variation in the flow fields between cycles and stronger impacts on future cycles.

3.4 *Discussion and Conclusion*

Cycle-to-cycle performance and flow-field variability for cross-flow turbines are often implicitly neglected through time- and phase-averaging, but, as demonstrated here, are statistically significant. This variability is potentially caused by dynamic stall's stochastic nature, freestream velocity perturbations, and hysteresis from previous cycles. In this work, we explored the extent and sources of cycle-to-cycle variability using near-blade flow fields and performance metrics for sub-optimal, $\lambda = 1.5$, and near-optimal, $\lambda = 2.5$, tip-speed ratios. The flow-field clustering technique developed for this purpose proved sensitive to cycle-to-cycle variations and highlighted correlations between performance and flow-field variability. This technique was effective for both tip-speed ratios despite

the lower flow-field variability for $\lambda = 2.5$, where dynamic stall is weaker.

Overall, performance and hydrodynamic variability were found to be non-coincident in phase and differ in magnitude. Across all phases, the coefficient of variation in performance ranges from $4 - 20\%$. While an imperfect comparison, the phase-specific flow-field coefficients of variation are as high as 110%, an order of magnitude greater. Performance variability is highest around the maximum performance within a cycle, but, because of limits to near-blade flow-field resolution, observable flow-field variability is minimal until beyond maximum performance. For $\lambda = 1.5$, flow-field variability increases during the growth and shedding of the large dynamic stall vortex, and, for $\lambda = 2.5$, during the growth of the separated flow region at the trailing edge. Despite this lag in the flow-field variability, clusters based on observed flow fields throughout the rotation are correlated with time- and phase-averaged performance for both tip-speed ratios. This is not evident when considering only aggregate, statistical measures of variability.

Hysteresis and dynamic stall stochasticity may contribute to variability, but freestream velocity perturbations dominate the observed cycle-to-cycle variation in both the flow fields and performance. Given that the high flow-field variability at the end of the turbine rotation is not accompanied by high variability at the beginning of the rotation, it is unlikely that hysteresis impacts are substantial. While we cannot completely disentangle the impacts of freestream velocity perturbations and dynamic stall stochasticity, the cycle-specific freestream velocities are correlated with the flow-field clusters. These velocity perturbations are shown to impact the kinetic energy available in the flow and to perturb λ enough to influence the dynamic stall process. For $\lambda = 1.5$, the better-performing cluster for $\theta = 95 - 143°$ exhibits higher inflow velocities, a higher reversed flow fraction, earlier dynamic stall vortex shedding, and a performance peak occurring slightly earlier in the cycle. All of these behaviors are consistent with the locally lower λ, however, the higher performance is counter to the trend where a lower λ is associated with lower maximum and time-averaged performance. This contradiction is also present for the $\lambda = 2.5$ case. When performance is calculated with a cluster-specific kinetic power, the apparent contradiction is resolved and the locally higher tip-speed ratio cluster outperforms the other. This suggests, for these conditions, the change in the available kinetic power in the inflow has a greater influence than the perturbation

to the local tip-speed ratio.

A clear performance and hydrodynamic dependence on assigned cluster is observed, despite the freestream turbulence intensity of 1.8-2.1%, which is relatively low in comparison to field conditions [91]. That said, the differences in time-averaged performance between clusters are small (1-3% relative to the time-average of all data). Therefore, for these conditions, phase-averaging flow fields and performance is an effective way to investigate general trends. This work demonstrates that clustering is useful for more nuanced analyses that seek to understand the connections between observed flow fields and turbine performance. We must note that, in future studies, it would be important to consider the number of clusters as a free parameter. Here, two clusters proved appropriate, but this may not be optimal for all cases. For the current data set, two clusters produce unique phase-averaged weighted activation profiles in the principle component analysis.

The flow-field clustering approach contributes to our understanding of the mechanisms responsible for the performance and hydrodynamic variability of cross-flow turbines. It provides a more comprehensive picture of the phase-varying flow fields than aggregate, statistical representations, and provides conditionally averaged groups that are not based on subjective, hand-engineered metrics. We observe physically meaningful clusters representing a series of distinct flow-field evolutions. These clusters are correlated with performance, and reveal variations in timing of the dynamic stall process. The specific mechanisms underlying cycle-to-cycle variability may change for different inflow conditions (e.g., Reynolds number), turbine geometry, and kinematics, as well as for other non-turbine systems experiencing dynamic stall.

Chapter 4

THE INFLUENCE OF THE DOWNSTREAM SWEEP ON CROSS-FLOW TURBINE PERFORMANCE

The work in this chapter is co-authored by Aidan Hunt, Brian Polagye, and Owen Williams. Material preparation and data collection were performed by the author and Greg Talpey. All data analysis, visualization creation, and code base development were performed by the author with support from Aidan Hunt. The manuscript was written by the author. Brian Polagye and Owen Williams advised throughout this project and were involved in the framing and editing of the final manuscript.

4.1 *Introduction*

The drivers of cross-flow turbine performance are not well understood especially during the downstream sweep where the inflow is substantially modified by power extraction in the first half of the rotation. The upstream sweep clearly influences overall turbine efficiency, but our knowledge of cross-flow turbine operation is fundamentally incomplete without a full understanding of the dynamics in the downstream sweep. Prior works [9, 11, 18, 53] have found substantial differences in performance between the upstream and downstream sweeps. Here we specifically investigate the downstream sweep, which has received significantly less dedicated research attention. In doing so, we aim to illuminate its importance on cross-flow turbine performance and to clarify the drivers of downstream sweep performance.

Most research that has focused on interpreting and optimizing cross-flow turbine performance has primarily considered the power-generating phases of the upstream sweep, but a limited number of works discuss the fluid dynamics and/or performance differences between the upstream and downstream sweeps. Rezaeiha et al. [18] showed computationally that for six tip-speed ratios,

time-averaged performance contributions from the downstream sweep are substantially smaller than upstream, and that downstream performance degrades with increasing tip-speed ratio, while upstream performance improves. They explain the reduction in downstream performance with increasing tip-speed ratio as a consequence of greater momentum removal in the upstream sweep. Because the upstream sweep contributes the most to power production, they concluded it is most important for overall turbine performance, and, as such, should be the focus for power-enhancement strategies. However, Mulleners et al. [92] experimentally applied an active pitch controller and found performance at a high tip-speed ratio could be improved predominately by changes in power production in the downstream sweep. Recently, Le Fouest et al. [46] experimentally investigated the time-scales associated with dynamic stall and cross-flow turbine forcing. They attributed changes in the fluid dynamics and performance between the upstream and downstream to differences in dynamic stall development stemming from the asymmetry of the nominal angle of attack trajectories between the upstream and downstream sweeps. However, their description does not explicitly include the influence of induction, which modifies the nominal kinematics.

In addition, several groups have attempted to explain performance variations for different turbine geometries through observed changes in the upstream and downstream regions. Hunt et al. experimentally [3] and Rezaeiaha et al. computationally [21] highlight opposing trends in performance between the upstream and downstream sweeps as a function of the preset pitch angle. Hunt et al. emphasize that the optimal preset pitch angle, in terms of overall turbine performance, is not equal to that which maximizes the power generated during the upstream sweep, but rather represents a compromise between improvements to the upstream sweep and degradation in the downstream sweep. Li et al. [20] discuss how force coefficients computed from experimental surface pressure measurements differ between the upstream and downstream sweeps for different turbine solidities (varied by changing the blade count, N). They hypothesize that pressure differences across the blade decrease in the downstream sweep because the magnitudes of the angle of attack and relative velocity are reduced by induction. Similarly, Rezaeiha et al. [19] computationally highlight opposing upstream/downstream performance trends with solidity (varied by changing c/r and N). As in their other work [18], decreased power generation in the

downstream sweep at higher solidities is attributed to reductions in available momentum.

These prior works discuss different trends between the upstream and downstream sweeps, suggest linkages between them, and pose three explanatory mechanisms for downstream performance degradation relative to upstream: (1) reduced momentum available in the downstream sweep [18, 19], (2) different blade kinematics (angle of attack, relative velocity) throughout the downstream sweep [20], and (3) the near-blade dynamics in the downstream sweep associated with dynamic stall and flow recovery, interactions with previously shed coherent structures, and the reversal of the pressure and suction sides of the blade [46]. All three mechanisms are inextricably linked through induction, but prior work has not described the relationships between them or addressed the relative importance of these mechanisms.

Here, experimental turbine performance is measured in concert with phase-locked particle image velocimetry (PIV) flow fields for a one-bladed turbine to directly characterize the dynamics and performance contributions of the downstream sweep. The chapter is laid out as follows. Section 4.2 presents the methodology for the turbine performance and flow-field measurements. Section 4.3 describes how performance, induction, and the near-blade dynamics differ between the upstream and downstream sweeps. Then, the explanatory mechanisms responsible for downstream performance degradation are explored, and the accuracy of the nominal formulations of the angle of attack and relative velocity in the downstream sweep are evaluated. The effect of induction on the kinematics and dynamics of cross-flow turbines is explored, and a new analytical model for a limiting case where in-rotor velocities are negligible is presented. The generalization of the observed downstream performance trends is then demonstrated in Section 4.4 by reanalyzing 54 additional unique performance experiments from [3] that parametrically vary preset pitch angle, chord-to-radius ratio, and the Reynolds number.

4.2 *Methods*

We explore the influence of the downstream blade sweep on cross-flow turbine performance using a one-bladed turbine. Since, in our experiments, turbine torque is measured at the center shaft, the use of a one-bladed turbine allows for isolation of the performance contributions for the upstream

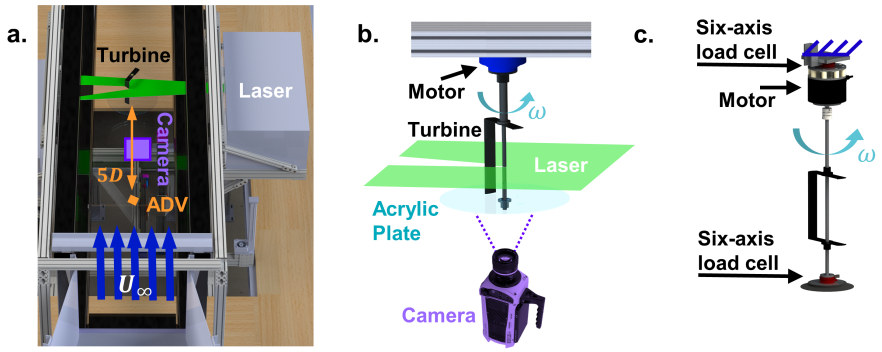

Figure 4.1: (a) Annotated PIV and performance experimental setup in the flume, (b) “PIV measurement" turbine setup with the camera and laser sheet arrangement, and (c) “performance measurement" turbine setup.

and downstream portion of the rotation (i.e., with a multi-bladed turbine, the torque contribution from each blade is ambiguous). Flow fields are investigated to contextualize the fluid dynamics that underly the observed performance trends. For this purpose, two-component, phase-locked, planar PIV data is obtained inside the turbine swept area at the blade mid-span for three tip-speed ratios, $\lambda = 1.4, 2.4, 3.4$.

4.2.1 Experimental Facility

Experiments were performed in the Alice C. Tyler flume at the University of Washington (Figure 4.1a). The data presented in this chapter utilized a mean dynamic water depth of 0.52 m. The channel cross-sectional area was 0.39 m^2 (0.75 m width). The water temperature was maintained at 39 ± 0.2 °C, giving a density of 993 kg/m^3, and a kinematic viscosity of 6.7×10^{-7} m^2/s. An acoustic Doppler velocimeter (Nortek Vectrino) operating at a 16 Hz sampling rate, positioned approximately 5 diameters upstream of the turbine rotor measured the inflow. The average U_∞ was 0.9 m/s with a turbulence intensity, of 1-2%. These conditions corresponded to a depth-based Froude number, of 0.4.

4.2.2 *Cross-flow Turbines and Performance Characterization*

Two experimental turbine setups were used in these experiments: the "PIV measurement" setup (Figure 4.1b) and the "performance measurement" setup (Figure 4.1c). In either configuration, turbine rotation rate was regulated by a servomotor to achieve a desired λ for a given test. Blade position was measured by the servomotor encoder with a resolution of 2^{18} counts/rotation and ω was computed by differentiation. MATLAB Simulink Desktop Real-Time was used for data collection and turbine control. For each control set point (i.e., a single λ), all data were acquired for 60 seconds at 1 kHz. The "PIV measurement" test setup utilized a servomotor (Yaskawa SGMCS-02B) rigidly coupled to the flume cross beam and controlled with a drive (Yaskawa SGDV-2R1F01A002). The turbine utilized for PIV measurements is identical to that in Section 3.2.2. Forces and torques were not measured with this test setup, and this turbine is sub-optimal for performance measurements due to high drag on the acrylic plate (particularly at high rotation rates).

In the "performance measurement" test setup, forces and torques were measured by a pair of six-axis reaction load cells (above rotor: ATI Mini45, below rotor: ATI Mini40). This setup used a servomotor (Yaskawa SGMCS-05B) and the same drive as for the "PIV measurement" setup. To improve performance measurements, the support structures in the "PIV meausurement" turbine were replaced by NACA 0008 foil struts supporting each end of the blade span. The turbine solidity,

$$\sigma = \frac{Nc}{2\pi r}, \tag{4.1}$$

was 0.49. The blockage ratio, $\beta = \frac{SD}{A_C}$ (where S is the blade span), was 10.3% and the Reynolds number, $Re_c = \frac{U_\infty c}{\nu}$, was 5.5×10^4. As in Chapter 3, blade-level performance was isolated by subtracting phase-averaged performance for the turbine support structure (blade removed, at the same operating conditions) from the full turbine performance measurements. All torque measurements were filtered with a low-pass, zero-phase, Butterworth filter to remove high-frequency electromagnetic interference from the servomotor. The 30 Hz cutoff frequencies used for the turbine and support structure performance data are approximately 10 harmonics faster than the blade passage frequency so the filter is unlikely to remove any hydrodynamic torque.

The time-varying hydrodynamic power, P, was non-dimensionalized as the coefficient of per-

formance, C_P, defined as,

$$C_P(\lambda, t) = \frac{P(t)}{\frac{1}{2}\rho U_\infty^3 DS}, \tag{4.2}$$

where ρ is fluid density. Throughout, we refer to the coefficient of performance through the shorthand of "performance". The hydrodynamic torque, Q, was non-dimensionalized as

$$C_Q(\lambda, t) = \frac{Q(t)}{\frac{1}{2}\rho U_\infty^2 DSr}, \tag{4.3}$$

and the torque and performance coefficients are directly related by the tip-speed ratio as

$$C_P = C_Q \lambda. \tag{4.4}$$

Time-averages of any quantity, X, were calculated over an integer number of rotations for a single λ set point and represented as $\overline{X}$. We also present averages that are conditional on θ segments. For example, the upstream segment-averaged performance coefficient was computed by averaging all of the data points in the time-series that were measured for $0° \geq \theta < 180°$. A corresponding calculation was used to define a segment-averaged downstream performance coefficient. In this work, the upstream and downstream segment averages are scaled by 1/2 such that their sum is equal to the time-averaged performance for a full rotation. Phase averages of any quantity, X, for a single azimuthal position across multiple cycles at a λ set point are represented as $\langle X \rangle$. Since the performance data is captured continuously, we utilized an azimuthal bin of 1° for phase-averaging.

4.2.3 PIV Measurement

Two-dimensional, two-component, phase-locked flow-field measurements were obtained in a streamwise plane at the blade mid-span as described in Chapter 3. The general arrangement of the PIV laser and cameras is the same as in Section 3.2.3 and is shown in Figure 4.1a. The laser sheet was approximately 2 mm thick horizontal light sheet in the cross-stream direction. The flow seeding produced particle images of approximately 3 pixels in diameter. The PIV data utilized in this chapter were taken during two different experiments. The first experiment captured flow-field data for $\lambda = 1.4$ and $\lambda = 2.4$, and utilized a 60 mm lens at f#16 resulting in a calibration of 7.9

pixels/mm and a field of view, FoV, of 32.4 x 20.3 cm [8c (1.9D) x 5c (1.2D)]. The second experiment captured flow-field data for $\lambda = 3.4$ and utilized a 50 mm lens at f#4 resulting in a calibration of 8.22 pixels/mm and 31.1 x 19.5 cm [7.6c (1.8D) x 4.8c (1.1D)] FoV. The limited streamwise extent of the laser sheet necessitated shifting the turbine by $\approx \frac{1}{2}D$ upstream to illuminate and capture the downstream blade sweep (logistically preferred to shifting the laser). Cross-stream FoV positioning relied on camera movement with a motorized, three-axis gantry. This gantry also allowed for fine adjustments in the streamwise direction.

Sequences of 59 image pairs were acquired per rotational cycle with prescribed angular displacements of approximately 3° between frames for $\theta = 9° - 176°$ and $\theta = 183° - 353°$. Twenty image pairs were captured at each phase over twenty rotations. As described in Section 3.2.3, PIV measurements were conducted with the turbine spinning in both clockwise and counter-clockwise directions to minimize the influence of shadows, and matte black paint was applied to minimize laser reflections at the blade surface.

PIV processing was performed as described in Section 3.2.3. The data processing and experimental resolution resulted in approximately 40 vectors per chord length. Spurious vectors were removed with a universal outlier median filter [87] utilizing a 9x9 filter region and a threshold value of 1.5 for the $\lambda = 1.4$ case and 2.5 for the $\lambda = 2.4$ and $\lambda = 3.4$ cases. Flow fields from both rotation directions were combined in post-processing. To produce the composite fields, the center of rotation was first located and aligned between the different FoVs as outlined in Section **??**. Then, the phase-averaged flow fields were interpolated to a common grid and the two rotation directions at each phase with the same FoV were averaged.

4.2.4 Flow-Field Analysis

The flow-field analysis in this work utilizes either segment-averaged velocity magnitude fields, $||\overline{\vec{V}}||$ in a flume reference frame, or phase-averaged relative velocity fields in the blade-centric reference frame, $||\langle\vec{U_{rel}}\rangle||$. The $||\overline{\vec{V}}||$ fields were computed separately for the upstream and downstream sweeps and are an average of the composite flow fields at all blade positions. Any regions of data missing in $\geq 20\%$ of the composite flow fields (regions that are in the masked areas in both rotation

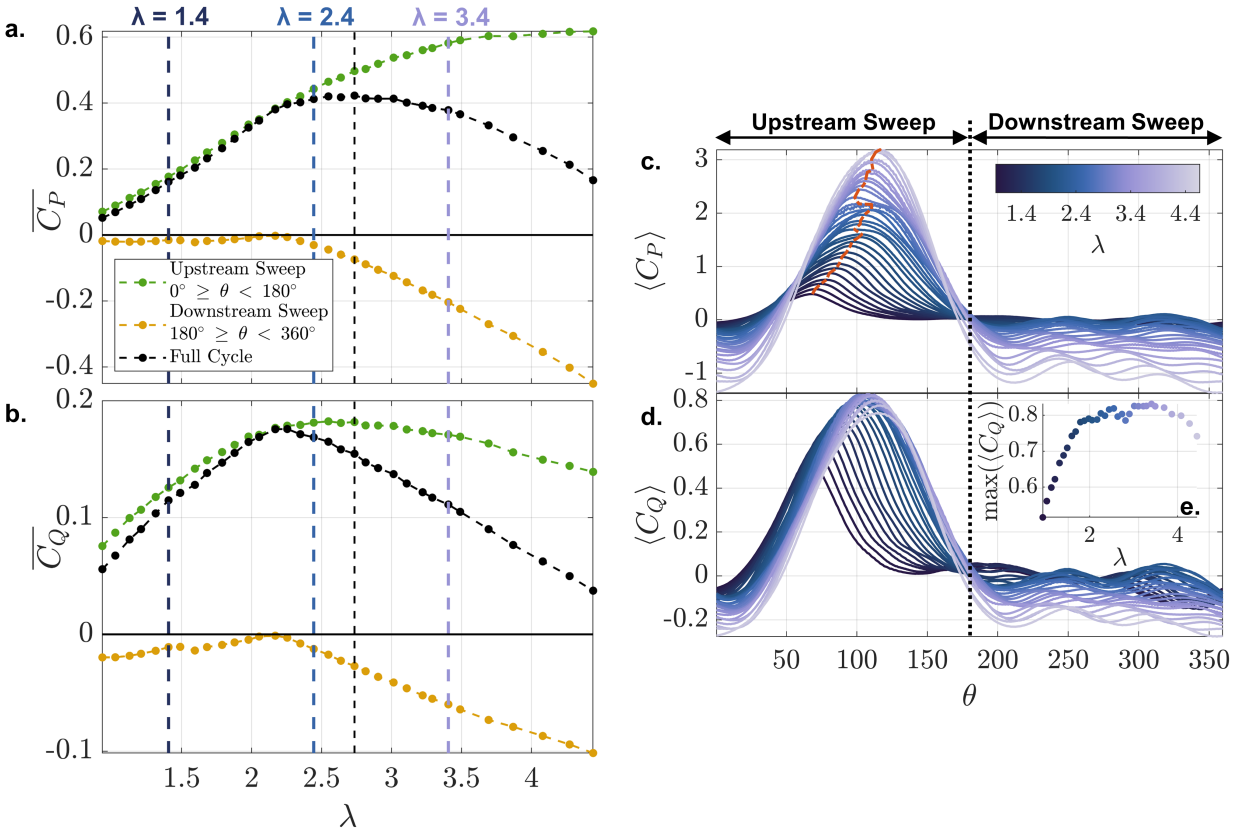

Figure 4.2: (a) Time- and segment-averaged coefficient of performance and (b) time- and segment-averaged coefficient of torque. The upstream and downstream segment-averages are scaled by 1/2 such that their sum is equal to the total time-averaged performance. The vertical, black dashed line corresponds to the optimal tip-speed ratio and the colored, dashed lines denote the tip-speed ratios where flow fields were acquired. (c) Phase-averaged performance coefficient and (d) torque coefficient. (e) The value of the maximum torque coefficient as a function of tip-speed ratio. The orange dashed line in the upstream sweep in (c) tracks the phase of maximum performance.

directions) were ignored in the segment-average. The flow fields were translated to the blade-centric reference frame by first rotating the entire field about the center of rotation to a common blade orientation and then computing the $||\langle \vec{U_{rel}} \rangle||$ fields as the vector sum of the flume-reference velocity fields and the blade tangential velocity.

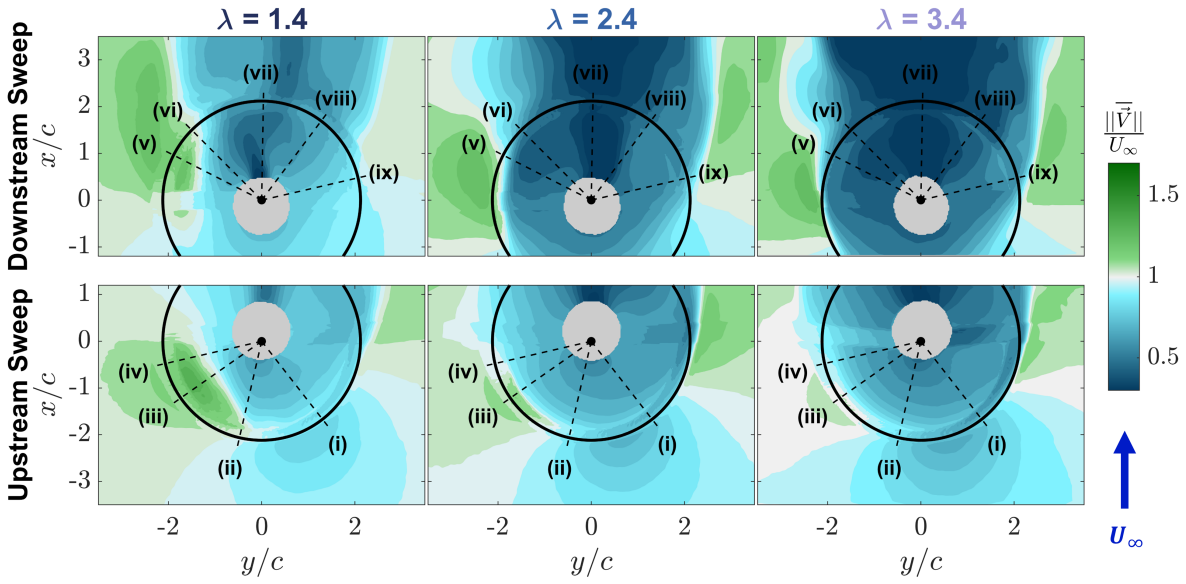

Figure 4.3: Segment-averaged horizontal velocity magnitude fields for the upstream and downstream sweeps for $\lambda = 1.4$, $\lambda = 2.4$, and $\lambda = 3.4$. Freestream flow is from the bottom to the top. The colorbar has been truncated at 0.3 and 1.7 for visualization. The black circles represent the blade sweep. The radial dashed lines correspond to the locations of the phase-averaged flow fields presented in Figure 4.4c,d. The upstream sweep is averaged over $\theta = 9° - 176°$ while the downstream sweep is averaged over $\theta = 183° - 353°$.

4.3 *Results*

4.3.1 Performance and Torque Measurements

As shown in Figure 4.2a, time-averaged turbine performance increases with tip-speed ratio up to an optimal value ($\lambda_{opt} = 2.7$) beyond which performance begins to decrease. However, when the upstream and downstream contributions to this time-averaged performance are partitioned, it is clear that upstream sweep performance continues to increase beyond the optimal tip-speed ratio. In contrast, downstream sweep performance is approximately net neutral (i.e., segment-average $C_P \approx 0$) until around $\lambda = 2.4$, after which it begins to decrease at a faster rate than the upstream

performance increases. This indicates that the optimal tip-speed ratio for this turbine is strongly influenced by the onset of continuous performance degradation in the downstream sweep.

Figure 4.2b shows that the time-averaged torque coefficient in the upstream sweep slowly declines beyond the peak tip-speed ratio. Since turbine performance is the product of the torque coefficient and the tip-speed ratio (Equation 4.4), this indicates that the tip-speed ratio drives the upstream performance increase beyond λ_{opt}. Therefore, not only does the tip-speed ratio influence the kinematics, near-blade dynamics, and torque production, but the tip-speed ratio can compensate for moderate torque losses in the upstream sweep in terms of performance. In the downstream sweep, torque is increasingly negative, so the tip-speed ratio only exacerbates detrimental downstream performance (i.e., power consumption). Additional support for this conclusion is provided by the phase-averaged coefficients of performance and torque (Figure 4.2c-e). In the upstream sweep, the amplitude of the performance peak increases continuously with the tip-speed ratio (Figure 4.2c). As the tip-speed ratio increases, the upstream torque peak grows in width and amplitude and shifts to later in the cycle until the timing and amplitude of the peak become relatively independent of λ for $\lambda = 2 - 4$, beyond which peak torque begins to decrease (Figure 4.2d,e). In contrast to the upstream sweep, performance and torque contributions in the downstream sweep (Figure 4.2c,d) are relatively independent of phase and increasingly detrimental as the tip-speed ratio increases. For all experiments, the parasitic performance and torque at the end of the downstream sweep persist into the beginning of the upstream sweep.

While the significant influence of the downstream sweep is clear, these data cannot entirely identify the mechanisms for the continuous downstream performance degradation. As previously discussed, three explanatory mechanisms have been proposed in prior work: reductions in available momentum, changes to blade kinematics, and changes to the near-blade dynamics. To evaluate the relative importance of these mechanisms, we explore the extent of induction and near-blade flow structures. Turbine flow fields are analyzed for three contrasting performance cases (one sub-optimal, $\lambda = 1.4$, one near-optimal $\lambda = 2.4$, and one beyond-optimal, $\lambda = 3.4$). The $\lambda = 2.4$ case is slightly less than optimal ($\lambda = 2.7$) and corresponds to the point where the downstream performance switches from being consistently nearly net-neutral to decreasing monotonically.

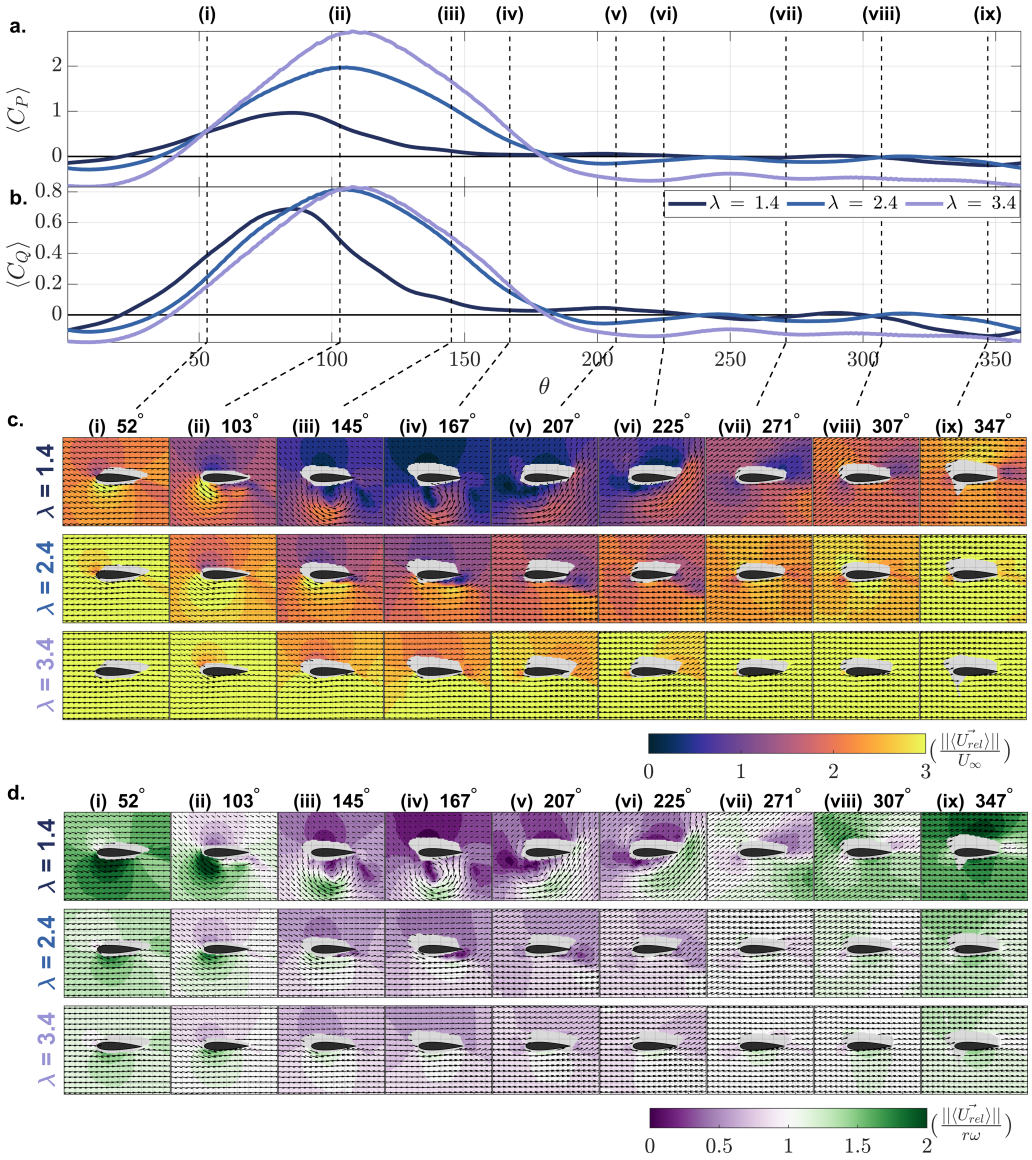

Figure 4.4: (a) Select phase-averaged torque (b) and performance corresponding to tip-speed ratios with PIV data ($\lambda = 1.4$, $\lambda = 2.4$, and $\lambda = 3.4$). The vertical dashed lines correspond to the locations of the phase-averaged flow fields presented in Figure 4.4c,d. Phase-averaged relative velocity fields normalized by (c) the freestream velocity and (d) the tangential velocity at these phases. Every 5$^{\text{th}}$ velocity vector is plotted and the axis grid spacing is $c/4$.

The in-rotor velocity, segment-averaged over the turbine swept area in the upstream and downstream regions, is shown in Figure 4.3 and seen to be slower than the freestream within the majority of the rotor area. These in-rotor velocities generally decrease as the tip-speed ratio increases. In all cases, there are isolated pockets of the upstream region of the turbine swept area with velocities higher than U_∞. We also observe velocities $\geq U_\infty$ in the bypass region between the turbine and the flume walls for all tip-speed ratios as a result of the divergence of the flow around the turbine and confinement. These results are generally consistent with linear momentum actuator disc theory for confined flow which predicts that flow should decelerate through the rotor but accelerate around it [57]. The most pronounced deceleration occurs in the downstream portions of the rotor and in the wake, where velocities generally decrease as λ increases and are as low as 8% of U_∞ for the highest tip-speed ratio. This demonstrates greater momentum loss through the turbine at higher tips-speed ratios and is consistent with Rezaeiha et al.'s [18, 19] conclusions from computational studies. Additionally, the width of the low momentum region and wake expands as the tip-speed ratio increases.

Changes to the free stream velocity from induction degrade the accuracy of the nominal descriptions for the relative velocity (Equation 2.2) and angle of attack (Equation 2.3) in the upstream and downstream sweeps. To evaluate the actual turbine kinematics in detail, we consider select phase-averaged, blade-centric flow fields in Figure 4.4 normalized by the freestream velocity, (c), and by the tangential velocity, (d). Corresponding phase-averaged performance and torque (which are a subset of the tip-speed ratios in Figure 4.2) are given in Figure 4.4a and Figure 4.4b, respectively. As with torque and performance, the flow fields depend strongly on λ and θ, and differ substantially between the upstream and downstream sweeps. Despite significantly lower in-rotor velocities at high tip-speed ratios (Figure 4.3), blade-relative velocities increase with tip-speed ratio at all phases (i.e., increasingly orange and yellow hues in Figure 4.4c) and converge towards the tangential velocity (i.e., increasingly lighter hues in Figure 4.4d), particularly in the downstream sweep. In other words, as λ increases, the higher tangential blade velocities outweigh the near-blade inflow velocities (which are reduced by increasing induction with λ), such that the relative velocity field is increasingly dominated by the tangential velocity. While this also clearly affects the angle

of attack, the heterogeneous nature of the relative velocity field defies a consistent definition for this kinematic term.

We now consider the influence of the near-blade dynamics. Overall, the complexity of the near-blade dynamics and the tip-speed ratio are inversely proportional for the three cases, as apparent by the weakening coherent structures throughout the turbine rotation at higher tip-speed ratios. This is in qualitative agreement with prior experiments [11, 13] and simulations [9, 16, 18]. The $\lambda = 1.4$ case has the most complex near-blade dynamics which include the roll-up and shedding (Figure 4.4c: ii-iv) of a strong dynamic stall vortex in the upstream sweep, as well as prolonged post-stall flow separation (v-vi) and more persistent separated flow (vii-ix) during the downstream sweep. The $\geq U_\infty$ velocity region between $\theta = 90° - 180°$ for the $\lambda = 1.4$ upstream segment-average (Figure 4.3) is a signature of the strong dynamic stall vortex while the blade is in that region. In contrast, the higher tip-speed ratio cases exhibit less complex near-blade dynamics, as evidenced by smaller vortex structures, limited flow separation (i-iv), faster post-stall flow recovery (v-vi), and minimal separated flow (vii-ix) in the downstream sweep.

The observed variation of the kinematics and near-blade dynamics with tip-speed ratio are qualitatively explanatory of the increased upstream torque production for the $\lambda = 2.4$ and $\lambda = 3.4$ cases. As the tip-speed ratio increases, dynamic stall weakens, stall onset is delayed to later in the cycle, and the relative velocity incident on the blade increases (Figure 4.4c). In aggregate, these mechanisms increase the amplitude of the torque peak and shift that peak later in the cycle until the phase of maximum torque becomes nearly independent of θ (Figure 4.2c). Similar trends are observed in the downstream sweep, where the phase-averaged flow fields indicate more attached flow and higher relative velocities as the tip-speed ratio increases. A trend towards attached flow is normally associated with a decrease in the drag coefficient and favorable lift generation, but, contrary to the upstream sweep, downstream torque production and performance contributions are initially minimal, then decrease linearly with λ (Figure 4.2a,b). Notably, the downstream near-blade dynamics are the most different between $\lambda = 1.4$ and $\lambda = 2.4$, but the attendant segment-averaged torque and performance differences are minimal as a consequence of opposing torque contributions across phase (Figure 4.4b). In contrast, while the near-blade dynamics are relatively unchanged

between $\lambda = 2.4$ and $\lambda = 3.4$, performance significantly decreases. This apparent mismatch between the performance trends and the near-blade flow fields indicates the near-blade dynamics are not likely explanatory of the increasingly detrimental downstream torque contribution in the downstream region.

Instead, the increasingly detrimental performance in the downstream sweep is primarily a consequence of reductions to available momentum and changes to the kinematics (i.e., a combination of two mechanisms). We note that even in the absence of induction, blade-relative velocities will converge to the tangential velocity at sufficiently high tip-speed ratios. This insight suggests the existence of a limiting case at a sufficiently high tip-speed ratio, λ_{lim} for which $U_{rel} = r\omega$. This condition is equivalent to the the no-inflow condition described by Migliore and Wolfe [17]. Cross-flow turbine performance depends, at the blade level, on the tangential projection of the resultant force (combination of lift and drag acting at $c/4$) in the direction of rotation, pitching moment (arising from a center of pressure displaced from $c/4$), rotation rate, and turbine radius to $c/4$. At λ_{lim}, the lift is perpendicular to the rotation direction (Figure 4.5a), has no tangential component, and is therefore unable to affect torque. Even for low drag coefficients associated with fully attached flow, the drag force directly opposes the rotation direction and increases with the tangential velocity. As the tip-speed ratio and induction increase, the in-rotor velocities decrease, and more of the downstream sweep begins to approach the limiting case (Figure 4.4d). In summary, at high tip-speed ratios, the orientation of lift and drag becomes increasingly unfavorable for power generation in the downstream sweep, and detrimental drag is magnified by increasingly high relative velocities. Therefore, induction adversely limits power production in the downstream sweep not only because less momentum is available, but lift and drag act in less favorable directions. The pitching moment contribution will either enhance or detract from this downstream performance degradation, but further work is necessary to quantify its effect.

Finally, the nominal kinematic model (Equations 2.2 and 2.3) poorly describes the kinematics throughout the blade rotation. Figure 4.5b highlights how the measured relative velocities differ from the nominal model, as well as the challenges of computing representative values for experimental relative velocity and angle of attack due to strong spatial variation. In contrast to the

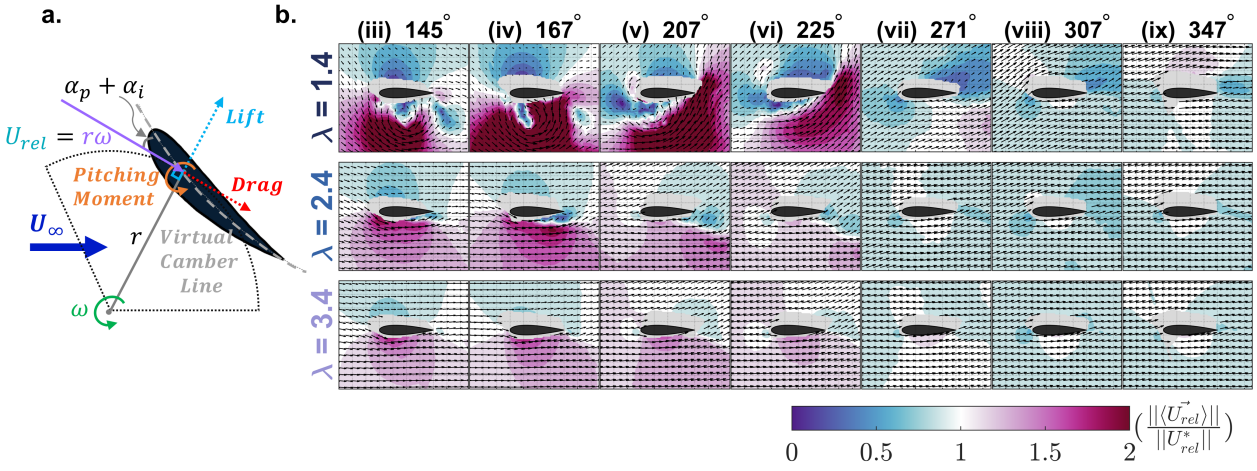

Figure 4.5: (a) Force and kinematic schematic for the limiting case where the relative velocity is equal to the blade tangential velocity. The blade shape reflects an exaggeration of virtual camber and neither the blade chord or radius are to scale. (b) Phase-averaged relative velocity fields normalized by the nominal relative velocity (Equation 2.2). Every 5th velocity vector is plotted and the axis grid spacing (visible in grey regions) is $c/4$.

hypothesis by Li et al. [20], that the relative velocity magnitude is reduced in the wake, the relative velocities incident on the leading edge of the blade in the low-momentum region (vi-viii) are not always smaller than the nominal predictions. Notably, opposing differences with respect to the nominal values between the pressure and suction sides of the blade throughout the rotation mean spatial averages of the relative velocity magnitude could roughly match the nominal model, and care must be taken when considering alternate methods.

4.3.2 Modeling the Downstream Sweep

Given the inability of the nominal kinetic model to describe the downstream sweep, we introduce an alternative analytical model for the limiting case (based on that derived for the no-inflow condition in [17]) for downstream performance at high tip-speed ratios where induction is most pronounced. Under these conditions U_{rel} and α are invariant to θ (steady-state aerodynamics). However, even

for the limiting case, cross-flow turbines are subject to virtual camber, C_v, and virtual incidence [16, 17] and the pitching moment is non-zero. At the high tip-speed limit, virtual incidence and camber are functions c/r and α_p. In the limiting case, this results in a foil that is virtually cambered in the direction shown in Figure 4.5a. Consequently, the aerodynamic coefficients are functions of the preset pitch angle and virtual geometric changes (camber and incidence) induced by the foil rotation. Depending on the amount of virtual camber, the lift vector likely acts towards the axis of rotation during the downstream sweep even for small negative values for the effective angle of attack (the sum of the angle of attack and the virtual incidence).

The limiting case model is defined as follows: U_{rel} is equal to $r\omega$, α is equal to the sum of α_p and the virtual incidence, and all steady-state aerodynamic coefficients are determined based on the virtually cambered foil geometry. Under these conditions, cross-flow turbine torque, Q_{lim}, for a given c/r and α_p, is a function of the drag coefficient, $C_D(C_v, \alpha)$, pitching moment coefficient, $C_M(C_v, \alpha)$, and tangential velocity as

$$Q_{lim} = C_D \frac{1}{2}\rho(r\omega)^2 Scr + C_M \frac{1}{2}\rho(r\omega)^2 Hc^2. \tag{4.5}$$

The corresponding coefficient of performance, $C_{P,lim}$ is (full derivation in Appendix B)

$$C_{P,lim} = \frac{r}{D}\left[-C_D\frac{c}{r} + C_M\left(\frac{c}{r}\right)^2\right]\lambda^3. \tag{4.6}$$

We note that r/D is not identically 1/2 because the radius is defined relative to the quarter chord and diameter is defined relative to the blade surface. The drag term is always detrimental to performance (negative torque) while the pitching moment term may either contribute or hinder performance depending on its sign (positive corresponding to a pitch-in – towards the center of rotation – moment in the direction of blade rotation, Figure 4.5a). We can make some estimates about the relative importance of the terms in Equation 4.6 using NACA 6418 airfoil data. This foil has a similar profile to virtual camber estimated for our geometry at the limiting case: maximum camber of $\approx 6\%$ occurring between the quarter and half chord locations (following the no-inflow formulation from [17]). The corresponding virtual incidence is $\approx 6°$, resulting in a $0°$ angle of attack. Under these assumptions, $C_D \approx 0.02$ and the pitching moment would be detrimental to

performance, $C_M \approx -0.1$. For $c/r = 0.49$, the drag-related term is approximately -0.01, and the pitching moment term is approximately -0.024, suggesting that the influence of virtual camber and pitching moment can be significant and detrimental to performance in the downstream sweep in the limiting case. We emphasize that this is only an order of magnitude analysis and a more complete evaluation would be beneficial. Preliminary calculations suggest that virtual camber may result in foils that depart from conventional NACA definitions in a number of ways, resulting in pressure gradients that may lead to transition or Reynolds number sensitivity, as well as relatively large changes in drag and pitching moment.

Finally, we observe that this model predicts downstream performance should scale with λ^3. Instead, we observe a linear relationship between λ and the performance degradation in the downstream sweep beyond $\lambda = 2.4$ (Figure 4.2a). This observation suggests that λ_{lim} is beyond the tip-speed ratio range tested for this turbine geometry and operating condition. This is not entirely surprising, given that the flow velocity is non-zero over significant portions of the downstream sweep, even for $\lambda = 3.4$ (Figure 4.3).

4.4 *Discussion*

4.4.1 Generalization to Other Geometries

To understand whether the observed performance trends discussed in Section 5.3 generalize to a broader set of turbine geometries and flow conditions, we apply the upstream and downstream segment-averaging framework described in Section 4.2.2 to 54 additional, unique, one-bladed turbine performance experiments from Hunt et al. [3]. In these experiments, the authors independently considered 5 chord lengths ($c/r = 0.25$ to 0.74), 6 preset pitch angles ($\alpha_p = -2°$ to $-12°$), and 3 diameter-based Reynolds numbers ($Re_D = 0.75 \times 10^5$ to 2.7×10^5). These experiments utilized the same blade aspect ratio, turbine diameter, and "performance measurement" test setup as described in Section 4.2.2, but the foil strut supports were replaced with circular plates to facilitate the different geometric variations. All performance data is processed as described in Section 4.2.2.

Contours of the segment-averaged performance within the upstream and downstream regions

at the optimal tip-speed ratio for each $c/r - \alpha_p$ combination are shown in Figure 4.6, with each column representing a different Re_D. Broadly, we observe contrasting performance trends between the upstream and downstream sweeps at the geometry-dependent optimal tip-speed ratios (Figure 4.6). Optimal performance in the upstream sweep increases with c/r, but decreases as α_p becomes more negative regardless of c/r. For both parameters, the opposite is true for the downstream sweep. As expected, optimal performance increases with Re_D in both the upstream and downstream sweeps. The characteristic performance curves in Figure 4.7a,b show that the segment-averaged trends are consistent with the experiment detailed in Section 4.3 (triangle markers; $Re_D = 2.3 \times 10^5$). Specifically, performance in the upstream sweep continues to increase well beyond the optimal tip-speed ratio for all experiments, and the optimal tip-speed ratio is driven by an approximately linear degradation in downstream performance (Figure 4.7a,b).

The optimal tip-speed ratio, as reported by Hunt et al. [3] and Rezaeiha et al. [19], is inversely proportional to turbine solidity (Equation 4.1). This relationship is evident in Figure 4.7c, for which N and r are constant and c varies. Rezaeiha et al. [19] show that induction increases with solidity, so we hypothesize that larger c/r turbines (higher solidity) have lower optimal tip-speed ratios because of increased induction that accelerates the convergence to the limiting case (Figure 4.5a). Beyond the optimal tip-speed ratio, the slope of downstream performance degradation is most closely correlated with the preset pitch angle (Figure 4.7d,e) and steepens for less negative preset pitch angles. This slope, $m_{\lambda_{opt}\rightarrow}$, is defined by the linear fit of $\overline{C_P}\frac{D}{c}$ (performance per blade area) for $\lambda \geq \lambda_{opt}$ when there are at least 3 points at and beyond λ_{opt}. The relationship between $m_{\lambda_{opt}\rightarrow}$ and α_p is not necessarily surprising since the aerodynamic coefficients are implicit functions of the angle of attack which is influenced by the preset pitch angle.

Two observations reaffirm the likelihood that the limiting case (Section 4.3.2) is not reached for any turbines in the current dataset and/or such a simple analytical model does not adequately describe the entirety of the downstream sweep. First, the approximately linear performance degradation beyond λ_{opt} differs from the λ^3 dependency in the limiting analytical model (Equation 4.6) for all geometries. Second, in the framework of the limiting kinematics, it is unexpected that $m_{\lambda_{opt}\rightarrow}$ steepens as α_p becomes less negative. Under steady-state, high tip-speed ratio kinematics, if

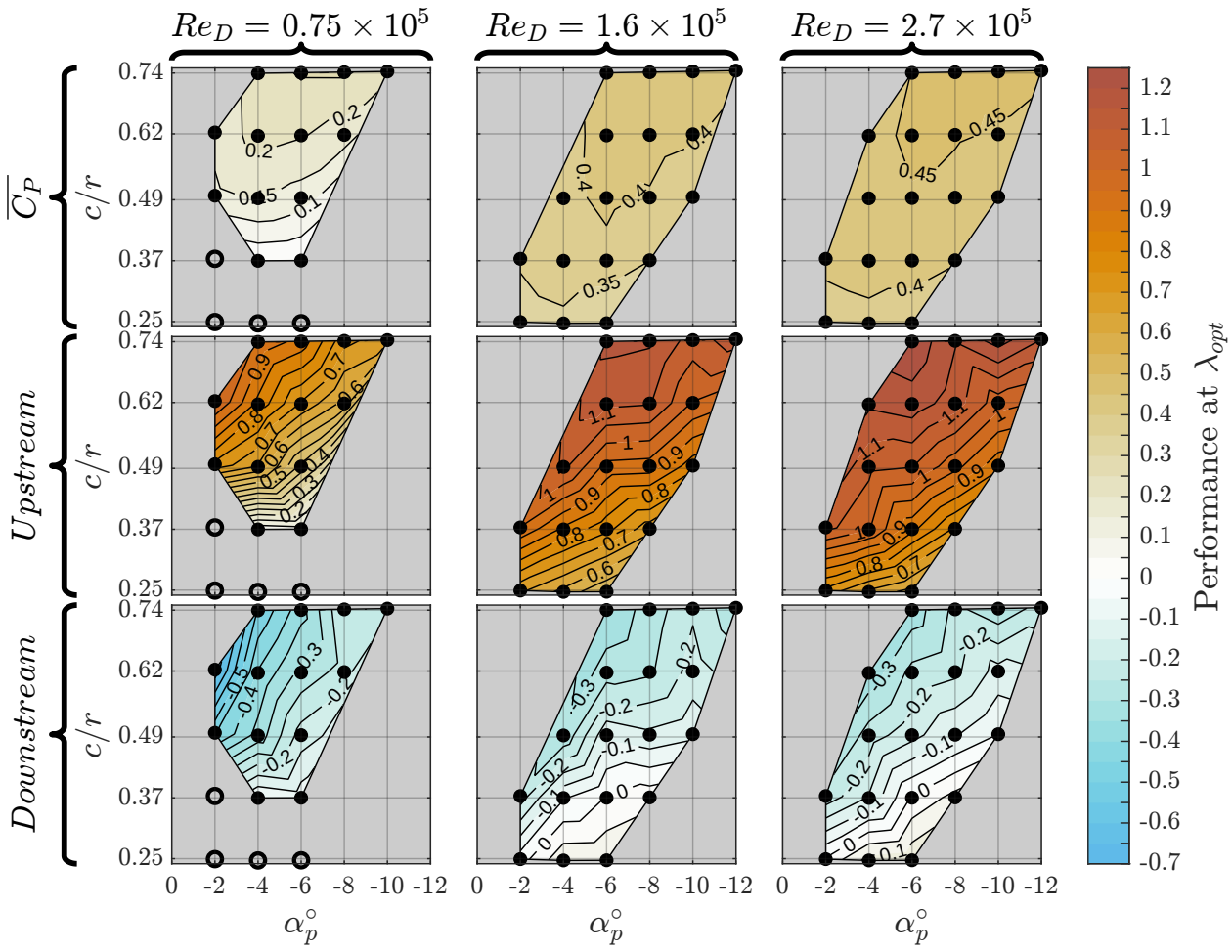

Figure 4.6: Total, upstream, and downstream segment-averaged performance at the optimal tip-speed ratio as a function of c/r, α_p, and Re_D for the 54 single-bladed combinations tested by Hunt et al. [3]. The optimal tip-speed ratio depends on the particular geometric configuration, but is largely invariant to Re_D. The unfilled circles indicate experiments that did not produce positive time-averaged performance for any tested λ.

the performance were drag-dominated in the downstream sweep, the slope would be expected to decline for less negative preset pitch angles (i.e., less negative angle of attack, less drag, less negative $m_{\lambda_{opt}\rightarrow}$). The inverse trend suggests that lift is still contributing to downstream torque and/or the pitching moment has a significant contribution at high tip-speed ratios.

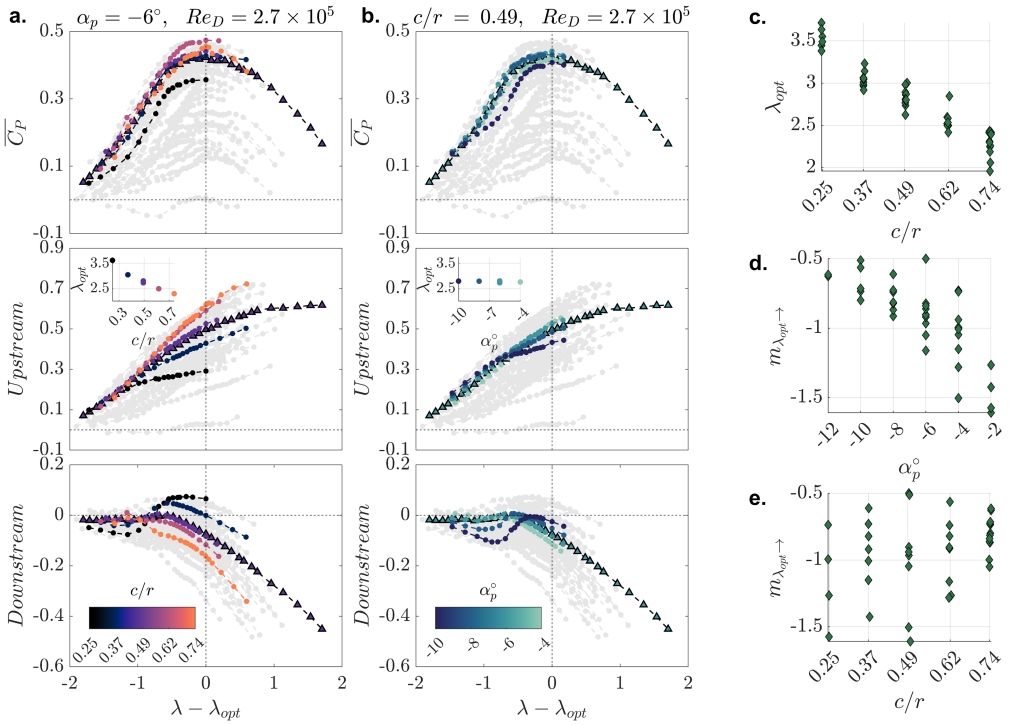

Figure 4.7: (a,b) Time and segment-averaged characteristic performance curves for all 55 unique turbine performance experiments. The triangles represent the one-bladed data collected for this work and the circles represent the 54 other one-bladed experiments from Hunt et al. [3]. The colored lines represent select data from two slices through the parameter space tested. In each column, a single parameter (a: c/r, and b: α_p) is varied, as indicated by the color bar. The gray lines represent all of the other experiments. Experiments that never produce positive blade-level performance are omitted for clarity. The optimal tip-speed ratio, λ_{opt}, is used to align the performance peaks of all experiments and is plotted against the selected parameter in the insets. (c) Relationship between the chord-to-radius ratio and the optimal tip-speed ratio for one-bladed turbines. (d) Relationship between the preset pitch angle and the slope of the linear fit to the coefficient of performance past the performance peak. (e) Relationship between the chord-to-radius ratio and the slope of the linear fit of the coefficient of performance past the performance peak.

The opposing performance trends between the upstream and downstream sweep with c/r observed in Figure 4.7a are likely a consequence of upstream momentum extraction and/or different force regimes: lift vs. drag/moment dominated. In terms of momentum extraction, the largest chord-length blades (higher turbine solidity) perform best in the upstream sweep, meaning they may also remove more momentum from the flow, limiting momentum available to the downstream sweep. This is consistent with conclusions drawn by Rezaeiha et al. [19]. In terms of different force regimes, the upstream sweep is lift-dominated for all tip-speed ratios (evidenced by positive performance), while the downstream sweep is drag/moment-dominated at high tip-speed ratios (evidenced by negative performance). Therefore, having a larger blade chord (more blade area) is beneficial in the upstream sweep (increased lift force) but likely detrimental in the downstream sweep (increased drag force). Once again the pitching moment may either enhance or detract from detrimental torque in the downstream sweep. The significance of the pitching moment influence would depend on c/r through virtual camber and incidence (affecting the pitching moment coefficient) and the moment magnitude (dependence on Sc^2).

The different α_p experiments in Figure 4.7b also show opposing performance trends between the upstream and downstream sweeps that are correlated with $\lambda - \lambda_{opt}$. More negative preset pitch improves performance in the upstream sweep until $\lambda - \lambda_{opt} = -1$, at which point the trend switches and the less negative preset pitches begin to perform best. Downstream performance is less detrimental for less negative preset pitch angles at low λ, and for more negative preset pitch angles at high λ. In the upstream sweep, the tip-speed ratio dependency is likely related to a transition from a dynamic stall regime where stall is induced by the shedding of the dynamic stall vortex (low λ) to a regime where stall is induced by the kinematics (high λ). Specifically, at low tip-speed ratios, a reduction in the angle of attack (from more negative preset pitch angles) likely delays the shedding of the dynamic stall vortex to later in the cycle, increasing upstream performance. At high tip-speed ratios, stall is induced by the beginning of the pitch-down motion at the maximum angle of attack. This timing is independent of the preset pitch angle. Therefore, for the upstream sweep, the high tip-speed ratio cases likely benefit from less negative preset pitch angles because of higher lift coefficients associated with smaller reductions in the maximum angle of attack magnitude.

The opposing trends between the upstream and downstream sweeps likely result, in part, from the reversal of the pressure and suction sides of the blade between the upstream and downstream sweeps. By our sign convention (Equation 2.3), this means negative preset pitch angles decrease the angle of attack magnitude in the upstream sweep, but increase it in the downstream sweep. As with c/r, the opposing trends between the upstream and downstream sweeps for α_p could also result from reductions in downstream momentum. For example, optimal preset pitch angles for the downstream sweep are generally detrimental to upstream power production, theoretically leaving more momentum available to the downstream sweep. The opposite would be true for upstream optimal preset pitch angles.

4.4.2 Improving Downstream Sweep Performance

Performance in the upstream sweep continues to increase beyond the optimal tip-speed ratio (Figure 4.2a). Therefore, even if it is not possible to produce power in the downstream sweep, it may be possible to improve overall turbine performance by reducing detrimental downstream torque. At high tip-speed ratios, at least two mechanisms could improve downstream torque:

(1) entrain flow or momentum into the rotor (reducing induction, increasing λ_{lim}) in either the upstream or downstream sweep.

(2) limit parasitic torque by reducing the drag coefficient, altering the pitching moment and/or increasing lift. We note that each of these methods will limit parasitic torque, but because of the directionality of lift at high tip-speed ratios, changes to drag or pitching moment may have a larger impact.

Control strategies such as active pitch control have the potential to improve downstream performance [92]. Active pitch control strategies alter the turbine kinematics by varying the preset pitch angle throughout the rotation. This affects the amplitude, slope, and shape of the angle of attack trajectory and, therefore, the character of the near-blade dynamics and, by extension, the lift, drag and pitching moment coefficients. In the downstream sweep, the in-rotor velocity (unless there are significant changes in induction from changes to the upstream sweep) and the tangential velocity do not depend on the blade pitch angle, so active pitch control will not affect the relative

velocity vector or the direction of lift and drag. However, the ability to augment the aerodynamic coefficients throughout the rotation is still important and each blade can be actuated independently, facilitating individualized control between the upstream and downstream sweeps.

4.5 *Conclusion*

To date, research on optimizing cross-flow turbine performance has largely focused on the fluid dynamics of the upstream blade sweep, where most of the power is produced. In this work, we utilize turbine performance and torque measurements in concert with phase-locked PIV flow fields to directly characterize the dynamics and performance of the downstream sweep and to investigate the influence of the downstream sweep on overall cross-flow turbine performance. Performance and torque data are compared for 55 unique combinations of chord-to-radius ratio ($c/r = 0.25$ to 0.74), preset pitch angle ($\alpha_p = -2°$ to $-12°$), and Reynolds number ($Re_D = 0.75 \times 10^5$ to 2.7×10^5). Corresponding flow fields are presented for one of these experiments ($c/r = 0.47$, $\alpha_p = -6°$, and $Re_D = 2.2 \times 10^5$) at tip-speed ratios corresponding to sub-optimal, $\lambda = 1.4$, near-optimal, $\lambda = 2.4$, and beyond-optimal, $\lambda = 3.4$, turbine performance.

Across all experiments, the time-averaged performance in the upstream sweep continues to increase well beyond the optimal tip-speed ratio for complete cycles. In contrast, beyond the optimal tip-speed ratio, time-averaged performance in the downstream sweep decreases approximately linearly, at a faster rate than the upstream performance increases. This indicates that the optimal tip-speed ratio, and overall turbine efficiency, is strongly influenced by performance degradation in the downstream sweep. During the upstream sweep, the magnitude of the torque peak converges with increased tip-speed ratio, representing a balance between the lift, drag, and pitching moment coefficients, the relative velocity, and the projection of the aerodynamic forces into the direction of rotation. Therefore, the increased performance at high tip-speed ratios in the upstream sweep is the result of the tip-speed ratio multiplier and not higher torque production. In contrast, parasitic torque becomes continuously more detrimental in the downstream sweep. Additionally, we identify contrasting performance trends between the upstream and downstream sweep with c/r and α_p, indicating that geometric parameters can have different impacts on the upstream and downstream

sweeps. Specifically, we observe that it is common that the parameters that are optimal for upstream performance are not optimal for overall turbine performance.

Flow-field measurements suggest faster flow re-attachment during the downstream sweep at higher tip-speed ratios. While this would be expected to reduce drag, we observe increasingly parasitic torque. These trends indicate the near-blade dynamics are not likely the mechanism most responsible for the continuous downstream performance degradation. Instead, reductions to available momentum and changes to the blade kinematics due to induction are most explanatory. In addition to reducing the momentum available to the downstream sweep for power production, induction limits how effectively blades convert the available momentum into torque by orienting lift and drag into increasingly unfavorable directions. Specifically, induction drives the convergence to a limiting case where the relative velocity incident on the blade is equal to the tangential velocity, such that lift acts normal to the direction of rotation and drag directly opposes rotation. A pitching moment arising from rotation-induced virtual camber may further oppose rotation, but more detailed analysis is required to understand its relative magnitude and parametric dependencies. While it is unlikely the limiting case is reached for any of the experiments investigated in this work, lift and drag act in increasingly unfavorable directions as induction and the tip-speed ratio increase, resulting in diminished beneficial torque from lift production and higher parasitic drag.

Improvements to downstream torque will increase overall turbine torque generation and the optimal tip-speed ratio – if this can be done without degrading upstream sweep performance. Because the performance coefficient is the product of the torque coefficient and the tip-speed ratio, any improvements in torque are amplified in performance by the multiplication with higher optimal tip-speed ratios. Overall, the downstream sweep is critical to cross-flow turbine performance, and understanding it is necessary to improve power production, as well as decipher the potential benefits of alternative turbine geometries and advanced control strategies.

Chapter 5

EXPERIMENTAL IDENTIFICATION OF BLADE-LEVEL FORCES AND MOMENTS FOR CROSS-FLOW TURBINES

The work in this chapter is co-authored by Katherine Van Ness, Jennifer Franck, Brian Polagye, and Owen Williams. Experimental data collection was performed by Kate Van Ness and Greg Talpey. CFD simulations were performed by Jennifer Franck. All data analysis, visualization creation, and code base development were performed by the author. The manuscript was written by the author. Brian Polagye and Owen Williams advised throughout this project and were involved in the framing and editing of the final manuscript.

5.1 *Introduction*

The net mechanical power produced by a cross-flow turbine is the sum of the fluid power generation/consumption by the blades and consumption by any support structures such as the shaft and blade-shaft connections (e.g., plates, struts). In aggregate, these contributions are difficult to parse, but doing so can provide valuable insight into the fundamental operation of these devices. For example, it is entirely possible that two kinematic trajectories or rotor geometries could produce similar resultant force magnitudes at the blade, but substantially different torque. This is because torque arises from the combination of the force tangential to the bade path and pitching moment, which do not necessarily trend with the resultant force magnitude. Further, numerical research on cross-flow turbines is commonly performed with only the blades in the simulation domain [9, 10, 16, 19]. Thus, isolating blade-level forces is helpful for validation and comparison between experimental and numerical results. Information about blade-level forcing can also inform structural design of blades and their mounting to the central shaft. Specifically, the location, magnitude, and direction of the blade resultant force affect loads on mounting points and internal blade structure. At the

same time, it can be difficult to directly measure blade-level forces and torques. Le Fouest et al. [11, 46, 48] have measured forces on a laboratory-scale cantilevered blade with a custom array of strain gauges, as have McAdam et al. [93] and Bharath et al. [94] for larger turbines in the lab and deployed in the field respectively. Similarly, Li et al. [20, 95] have measured blade-level forces from pressure tap measurements in cross-flow turbine wind tunnel tests. However, in the majority of cross-flow turbine experiments [3, 7, 23, 63–65, 86], measurements are at the axis of rotation because this can be done more readily with off-the-shelf instrumentation. For a cross-flow turbine, relevant forces and torque consist of a thrust force in the flow direction, F_x, a lateral force perpendicular to the flow direction, F_y, and a torque about the axis of rotation, Q. Here, we present a methodology for extracting blade-level forces and moments from experimental measurements at the axis of rotation. Application of this method is shown to provide fundamental insight into blade-level contributions to turbine performance.

5.1.1 Blade-level Power Production

At the blade-level, fluid power depends on the tangential projection of the resultant force in the direction of rotation, pitching moment, rotation rate, ω, and radial distance, r, to the quarter chord, $c/4$ (Figure 5.1c). The resultant force, $\vec{F}^{\star}_{\text{blade}}$, a combination of lift and drag, varies throughout the rotation and acts at varying chordwise positions (Figure 5.1b). Here * denotes forces or torque arising from the fluid-structure interaction between the rotating blades and inflow. We assume the resultant force is uniformly distributed along the blade span, and, for convenience, we can prescribe this force to act at $c/4$, by introducing a pitching moment, $M^{\star}_{\text{blade}}$, arising from the displacement of the center of pressure from $c/4$ (Figure 5.1b,c). The magnitude and azimuthal variation in these forces and moment depend on the free stream velocity and the blade's tip-speed ratio. As defined in Figure 5.1, the time-varying tangential, $F^{\star}_{\theta}$, and normal, $F^{\star}_{r}$, components of $\vec{F}^{\star}_{\text{blade}}$ are computed as

$$F^{\star}_{r,\text{blade}}(t) \;=\; F^{\star}_{x,\text{blade}}(t)\sin\theta(t) - F^{\star}_{y,\text{blade}}(t)\cos\theta(t), \tag{5.1}$$

and

$$F^{\star}_{\theta,\text{blade}}(t) = F^{\star}_{x,\text{blade}}(t)\cos\theta(t) - F^{\star}_{y,\text{blade}}(t)\sin\theta(t), \tag{5.2}$$

where the subscripts x and y represent the streamwise (thrust) and cross-stream (lateral) force components respectively. The time-varying torque produced by a blade is

$$Q^{\star}_{\text{blade}}(t) = F^{\star}_{\theta,\text{blade}}(t)r + M^{\star}_{\text{blade}}(t). \tag{5.3}$$

The tangential component of lift produces torque in the direction of rotation and the tangential component of drag opposes rotation (Figure 5.1b). The pitching moment may act with or against rotation depending on its sign, with positive corresponding to a pitch-in moment (towards the center of rotation) in the direction of blade rotation (Figure 5.1c). As discussed in Chapter 4 we hypothesize that the pitching moment is an important contributor to performance degradation in the downstream sweep. While the pitching moment for a symmetric foil in steady flow is zero, flow curvature and dynamic stall result in non-zero pitching moments throughout the turbine rotation [17, 43, 46, 96]. The significance of this term during startup of cross-flow turbines is demonstrated via Unsteady RANS simulations by Bianchini et al. [96] who show the pitching moment drives asymmetry between the upstream and downstream sweeps. Further, Le Fouest et al. [46] experimentally identified landmark dynamic stall events for a cross-flow turbine blade using direct measurements of the tangential and normal forces at the quarter chord and the pitching moment. Similarly, Dave et al [43] utilized Large Eddy Simulations to detail relationships between dynamic stall and cross-flow turbine forcing. In doing so, they attributed fluctuations in the pitching moment to dynamic stall effects at low tip-speed ratios, and to virtual camber effects at high tip-speed ratios. Despite the demonstrated non-zero values of the pitching moment in cross-flow turbines, this term is commonly neglected in discussions of cross-flow turbine performance and in low-order models, potentially as a consequence of its irrelevance to power production in axial flow devices [96]. This could also stem from a historical oversight as Strickland [97], who is credited for the first application of a momentum model with multiple stream tubes to cross-flow turbines, states that, “the pitching moment on the blade element ... is of no consequence for calculation of rotor performance”. A similar assumption carries through into Paraschivoiu’s development of a

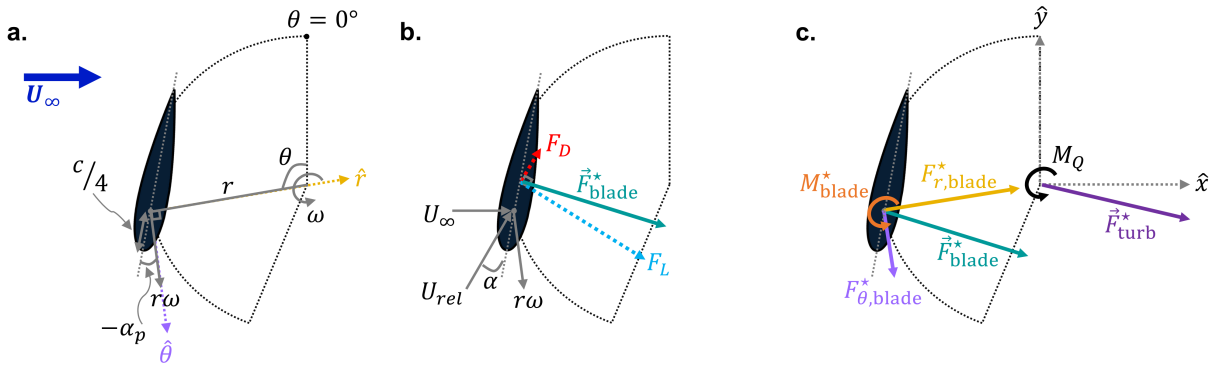

Figure 5.1: (a) Cross-flow turbine blade geometric definitions and blade-level coordinate system. (b) Kinematic definitions and directions of lift and drag. (c) Corresponding free body diagram and global coordinate system.

Double Multiple Streamtube model [26] and subsequent enhancements (e.g., [25, 27, 28, 98]). On the other hand, the pitching moment term is implicitly included in computational fluid dynamic simulations when torque is computed as the cross-product of the resultant force on the blade and the distance from the center of pressure. If the resultant force is translated to a reference location, such as the quarter chord, a pitching moment arises.

5.1.2 Estimating Blade-level Forces and Torques

A simple strategy to estimate blade-level torque from measurements at the axis of rotation involves superposition. Inspired by Li and Calisal [99] and Bachant and Wosnik [65], Strom et. al. [84] demonstrated that blade-level torque could be approximated by subtracting phase-averaged torque for the turbine support structures (same operating conditions with blades removed) from the full turbine torque measurements. This strategy was applied in Chapters 3 and 4 to isolate blade-level torque. This superposition principle relies on the assumptions that (1) the torque measured with the blades removed is reasonably representative of the oppositional torque from the support structures in a full turbine and (2) secondary interactions between the blades and support structures are minimal. However, the first assumption seems contradicted by the variable flow in and around the turbine

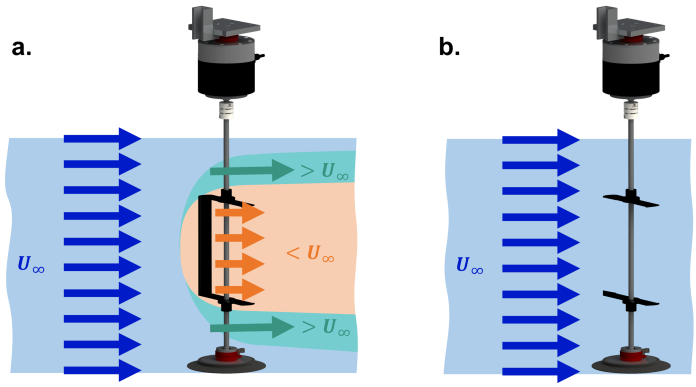

Figure 5.2: Conceptual representation of how the flow incident on the support structures may differ when (a) blades are present vs. (b) when absent.

due to induction, as discussed in Chapter 4. Specifically, the presence of the turbine substantially modifies the incoming flow such that flow is decelerated through the turbine and accelerated around it. While unknown *a priori*, induction means torques on support structures may vary substantially within the turbine span versus outside and differ when blades are present versus removed (Figure 5.2b). While assumption (1) is violated for the central shaft, because of the relatively low skin friction and small moment arm, this component of the support structure negligibly contributes to the torque acting on the turbine. In contrast, torque on the blade-shaft connections is substantial, assumption (1) is violated because of significant changes to induction, and assumption (2) is not guaranteed to be satisfied. Yet, this superposition strategy works surprisingly well for torque, as demonstrated by Strom et. al. [84] who highlighted a reasonable collapse in blade-level performance for a range of blade-shaft connection types. This result suggests torque on the blade-shaft connections may primarily be a function of the rotation rate, and/or velocities $> U_\infty$ on the outside of the blade-shaft connection are balanced by velocities $< U_\infty$ on the inside when the blades are present. We observed that the collapse is imperfect, potentially due to induction and/or secondary interactions.

If an analogous superposition approach were taken for forces measured at the axis of rotation,

it would be possible to estimate blade-level normal and tangential forces, as well as the pitching moment. However, estimating the blade-level hydrodynamic forces is likely more complicated because forces on the central shaft are appreciable, are anticipated to be the largest contribution to support structure force (verified in Section 5.3), and are expected to differ substantially with changes to induction. This work explores the efficacy of isolating blade-level force and moment components from turbine-level force and torque measurements at the axis of rotation for a single-bladed turbine. To do so we conduct experiments with four shaft configurations and test a new superposition strategy. The accuracy of estimated blade-level forces and moment are assessed through comparison to equivalent blade-only large-eddy simulations.

This chapter is structured as follows. Section 5.2 lays out the experimental setup, the procedure for isolating the blade-level hydrodynamic forces, and the simulation methods. In Section 5.3, we compare experimental force components to simulations. In Section 5.4, we discuss the efficacy of the method, highlight the value of considering the individual blade-level force components, and identify the importance of the pitching moment to turbine performance.

5.2 *Methods*

5.2.1 Experimental Setup and Data Processing

The experimental facility, turbine, and performance methods are identical to those presented in Chapter 4, though this work utilized only the "performance measurement" setup. To isolate blade-level contributions, turbine torques and forces for a single-bladed turbine were measured at the center shaft (i.e., with a multi-bladed turbine, the torque and force contribution from each blade are ambiguous). In addition to the "performance measurement" setup in Section 4.2, three other shaft configurations are tested. These are shown in Figure 5.3. The "Baseline" configuration consisted of a 1.27 cm diameter shaft and the other three configurations utilized 3.81 cm diameter collars fit over different portions of the "Baseline" shaft. The collars were placed outside of the turbine span and couplings, S' (29.1 cm for this turbine), for the "Outer" configuration, inside the turbine span for the "Inner" configuration, and along the entire shaft for the "Full" configuration. Because we

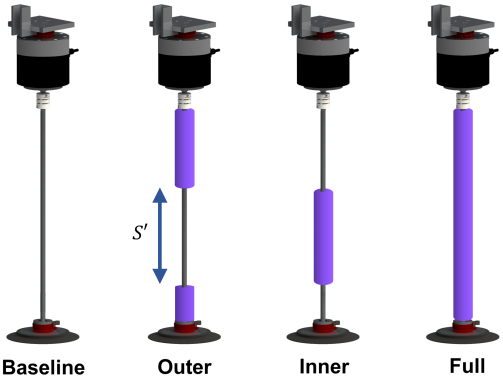

Figure 5.3: Schematics of the four different turbine shaft configurations tested: (a) “Baseline”, (b) “Outer”, (c) “Inner”, and (d) “Full”.

anticipate the force acting on the shaft to be appreciable, each of these arrangements are expected to generate different turbine-level forces.

Experimental conditions were adjusted to keep the depth-based Froude number, $Fr = U_\infty/\sqrt{gH} = 0.37$, turbine-level blockage ratio, $\beta = \frac{A_F}{A_C} = 12.7\%$, and Reynolds number, $Re_c = \frac{U_\infty c}{\nu} = 4.5\times10^4$ constant across the four shaft configurations. Here A_F is the frontal area of the turbine and all submerged components. The frontal area, mean dynamic water depth H, freestream velocity, and temperature (adjusts ν) for the different shaft configurations are summarized in Table 5.1. The turbulence intensity was 1-2% for all tests. Matching experimental conditions were used for the turbine experiments and the corresponding support structure and shaft-only tests.

5.2.2 Determination of Fluid Forces and Torques

Isolating the forces and torques arising solely from fluid-structure interactions in the experimental measurements is the first step to estimating blade-level quantities. This is accomplished by applying Newton’s second law, such that the sum of the forces and torques acting on the turbine at the center of rotation are

$$\sum \vec{F} = m\vec{a}_g \tag{5.4}$$

Table 5.1: Experimental parameters

Parameter	"Baseline"	"Outer"	"Inner"	"Full"
A_F (m^2)	0.047	0.054	0.047	0.054
H (m)	0.49	0.57	0.49	0.57
U_∞ (m/s)	0.8	0.86	0.8	0.86
Temperature	31	35	31	35
ν (m^2/s)	7.8432×10^{-7}	7.2363×10^{-7}	7.8432×10^{-7}	7.2363×10^{-7}
Re_c	4.5×10^4	4.4×10^4	4.5×10^4	4.5×10^4

and

$$\sum Q \;=\; J\dot{\omega} \tag{5.5}$$

where m is the mass of the rotating system, $\vec{a}_g$ is the acceleration of the center of mass, and J is the moment of inertia. The fluid torques, $Q^\star$, and forces, $\vec{F}^\star$, acting on the turbine and/or support structures may be computed from measurements as

$$\vec{F}^\star(t) \;=\; m\vec{a}_g(t) + \vec{F}_{\mathrm{m}}(t) \tag{5.6}$$

and

$$Q^\star(t) \;=\; J\dot{\omega}(t) + Q_{\mathrm{m}}(t) \tag{5.7}$$

where the subscript "m" denotes the sum of the forces and torque measured by the pair of load cells in the global coordinate frame (Figure 5.1). For solid body rotation, the components of $\vec{a}_g$ are $r_g\omega^2$ in the radial direction and $r_g\dot{\omega}$ in the tangential direction where r_g is the radius to the center of mass [100]. These components are expressed in the Cartesian coordinates as

$$a_{g,x}(t) \;=\; r_g(\omega(t)^2 \sin\theta(t) - \dot{\omega}(t)\cos\theta(t)), \tag{5.8}$$

and

$$a_{g,y}(t) \;=\; r_g(-\omega(t)^2 \cos\theta(t) - \dot{\omega}(t)\sin\theta(t)). \tag{5.9}$$

Under constant speed control, $\dot{\omega}$ is negligible, so after substituting and simplifying, Equations 5.6 - 5.7 reduce to

$$F_x^\star(t) \;=\; mr_g(\omega^2 \sin\theta(t)) + F_{x,\mathrm{m}}(t), \tag{5.10}$$

$$F_y^\star(t) \;=\; mr_g(-\omega^2 \cos\theta(t)) + F_{y,\mathrm{m}}(t), \tag{5.11}$$

and

$$Q^\star(t) \;=\; Q_{\mathrm{m}}(t). \tag{5.12}$$

The product of the rotating mass and radius to the center of mass, mr_g, is determined by conducting experiments in the absence of appreciable fluid forcing as described in Appendix C. The mr_g term is negligible for the axisymmetric experiments (i.e., support structure and shaft-only). Since the time integrals of $\cos\theta(t)$ and $\sin\theta(t)$ are zero, the time-averaged fluid forces are equivalent to the time-averaged measured quantities at the axis of rotation, regardless of rotational symmetry.

5.2.3 Non-dimensional Coefficients

We consider force and torque coefficients to determine blade-level quantities via the superposition of independent experiments (Appendix D). These coefficients are determined from the fluid torque and forces and may be computed for any component (e.g., turbine, support structures). For a given turbine geometry, matched relevant non-dimensional parameters (i.e., Reynolds number, Froude number, blockage), and constant speed control operation, the non-dimensional forcing on the turbine is a function of the tip-speed ratio. Any force component, such as $F_x^\star$ $F_y^\star$, $F_r^\star$, or $F_\theta^\star$, may be non-dimensionalized as

$$C_{F,i}(\lambda, t) \;=\; \frac{F_i^\star(t)}{\frac{1}{2}\rho U_\infty^2 DS}. \tag{5.13}$$

In contrast, the pitching moment is non-dimensionalized, in a manor akin to other aerodynamic coefficients, as

$$C_M(\lambda, t) \;=\; \frac{M^\star(t)}{\frac{1}{2}\rho (r\omega)^2 Sc^2}. \tag{5.14}$$

The tangential velocity is used instead of the relative velocity in Equation 5.14, as the latter changes with blade position and is unknown *a priori* (Chapter 4). The torque coefficient is defined in

Equation 4.3 and the performance coefficient for a turbine operating at constant speed is defined in Equation 4.2. Throughout this chapter, we refer to the performance coefficient using the shorthand of "performance".

From Equations 5.1, 5.2, and 5.13, the normal and tangential force coefficients may be expressed in terms of streamwise and cross-stream force coefficients as

$$C_{F,r} = C_{F,x} \sin\theta(t) - C_{F,y} \cos\theta(t) \tag{5.15}$$

and

$$C_{F,\theta} = -C_{F,x} \cos\theta(t) - C_{F,y} \sin\theta(t). \tag{5.16}$$

The torque coefficient is a function of the tangential force and pitching moment coefficients as

$$C_Q = C_{F,\theta} + C_M \lambda^2 \left(\frac{c^2}{Dr} \right). \tag{5.17}$$

In Equation 5.17, the $\lambda^2 \frac{c^2}{Dr}$ term arises due to the different velocity and length scales in the normalization of these factors (Equations 5.13 and 5.14). Finally, the torque and performance coefficients are directly related by the tip-speed in Equation 4.4.

In experiments, C_Q is computed from the fluid torque (Equation 4.3), while $C_{F,r}$ and $C_{F,\theta}$ are computed from the fluid force coefficients (Equations 5.15 and 5.16). The pitching moment coefficient is then solved for by re-arranging Equation 5.17. The $(U_\infty)^2$ term in Equations 5.13 and 4.3 (and in λ^2), as well as the $(U_\infty)^3$ term in 4.2 (and in λ^3) were computed by time-averaging of all of the squared or cubed freestream velocity measurements acquired at a tip-speed ratio set point respectively. This approach assumes that azimuthal variations in forces and torque dominate over fluctuations in the free stream and would likely be inaccurate if applied to field measurements or experiments with higher turbulence intensities.

Oscillations were observed in the turbine-level tangential force coefficient at frequencies higher than blade passage (Figure 5.4a). These oscillations were not present in the turbine-level torque coefficient, so they are unlikely related to fluid forcing on the blade. However, these could arise from turbine kinematics inducing vortex shedding off the turbine shaft (Figure 5.4c) and/or a fluid-structure coupling induced by the turbine forcing. A high-pass, zero-phase, Butterworth filter with

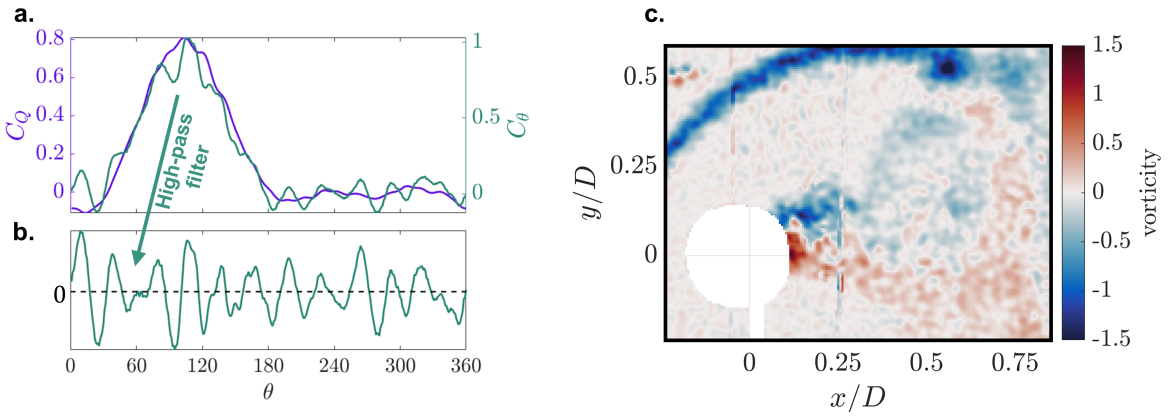

Figure 5.4: (a) Phase-averaged tangential force and torque coefficients for $\lambda = 2.4$ (b) Corresponding isolated phase-averaged secondary force oscillations. (c) Phase-averaged vortex shedding off of the central turbine shaft at $\lambda = 2.4, \theta = 201°$. Vorticity field is computed from PIV data from Chapter 4

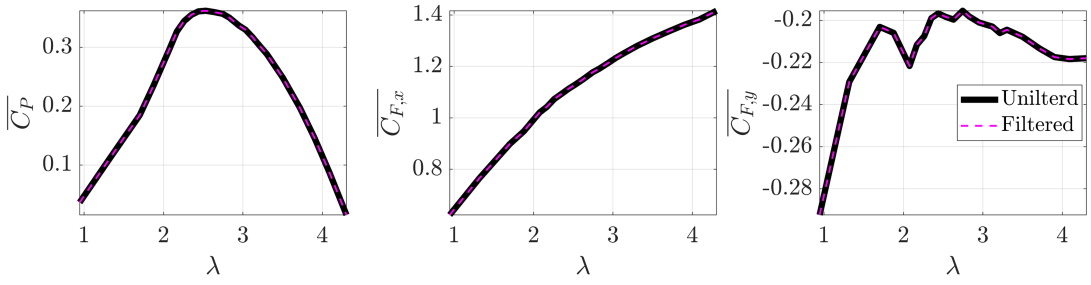

Figure 5.5: Comparison between filtered and unfiltered, time-averaged (a) performance (b) thrust force, and (c) lateral force coefficients

an 11 Hz cutoff frequency produced a time series dominated by the oscillations (Figure 5.4b). Consequently, an equivalent low-pass filter effectively removed the spurious oscillations and high-frequency electromagnetic interference from time series data. Because the spurious oscillations had near-zero time-average values, this filtering had a negligible effect on the time-averaged values (Figure 5.5).

5.2.4 *Determination of Blade-level Forces and Torque*

Figure 5.6 describes the proposed superposition strategy for determining blade-level forces and torque. A comparison between this method and the superposition strategy of Strom et al. [84], applied to blade-level forcing and torque, is presented in Appendix D. This "Scaled Shaft" strategy models the support structure contribution as a summation of the forces and torque incurred by the blade-shaft connections (i.e., struts) and the shaft, weighted by probable fluid forcing. This method is implemented on a non-dimensional basis where $\boldsymbol{C}$ represents the vector of non-dimensional coefficients: C_Q, $C_{F,x}$, and $C_{F,y}$. The contribution from the struts, $\boldsymbol{C}_{\text{struts}}$, is isolated by subtracting shaft-only force and torque coefficients, $\boldsymbol{C}_{\text{shaft}}$, from force and torque coefficients with all the support structures present, $\boldsymbol{C}_{\text{sups}}$ (i.e., $\boldsymbol{C}_{\text{struts}} = \boldsymbol{C}_{\text{sups}} - \boldsymbol{C}_{\text{shaft}}$). The shaft-only forces and torque are assumed to be evenly distributed along the submerged portion of the shaft. To estimate blade-level forces, the force contribution from the shaft within the turbine swept area is assumed to be negligible due to low incident velocities (Chapter 4). The proportion of force on the shaft outside of the turbine span (accounting for any differences in H for when the blades are present versus when they are absent) is then evaluated as $\boldsymbol{C}_{\text{shaft}} \frac{H_\Psi - S'}{H_\Upsilon}$ where the subscripts Ψ and Υ denote the turbine experiments and the

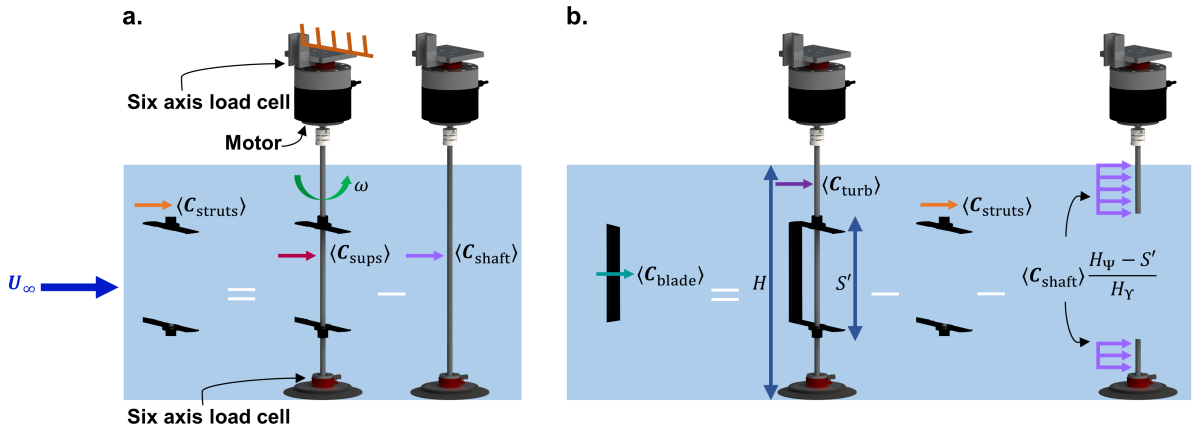

Figure 5.6: (a) Schematic of isolation of forcing on the struts. (b) Schematic of isolation of the blade level forcing for the "Scaled Shaft" strategy.

shaft-only experiments respectively. For configurations with heterogeneous shaft diameters, $\boldsymbol{C}_{\text{shaft}}$ corresponds to the portion of the shaft outside the turbine swept area. For example, the "Baseline" shaft-only data is used for both the "Baseline" and "Inner" configurations. The blade-level force and torque coefficients are then computed as

$$\langle \boldsymbol{C}_{\text{blade}} \rangle = \langle \boldsymbol{C}_{\text{turb}} \rangle - \langle \boldsymbol{C}_{\text{struts}} \rangle - \langle \boldsymbol{C}_{\text{shaft}} \rangle \frac{H_\Psi - S'}{H_\Upsilon}. \tag{5.18}$$

Further details of the derivation of Equation 5.18 are provided in Appendix D. Since data for each component of the superposition is collected in separate experiments, phase averages (average for a single azimuthal position across multiple cycles at a single λ represented as $\langle \cdot \rangle$) are used to estimate $\langle \boldsymbol{C}_{\text{blade}} \rangle$. For turbines rotating at a constant speed, time averages for any quantity "X" (experimental or simulation) are equal to the spatial average of $\langle X \rangle$ and represented as $\overline{X}$. For variable rotation rates, this average would need to be weighted by the inverse of rotation rate at each azimuthal position.

5.2.5 Simulation Methods

To assess the blade-level experimental results, a large-eddy simulation (LES) of a single blade (no struts or central shaft) was performed at matching conditions to the experiments. Specifically, the simulations consisted of a single NACA 0018 blade mounted at $c/4$ with -6° pre-set pitch and a c/r of 0.5.

The simulations solved the low-pass spatially filtered Navier-Stokes Equations, with a local dynamic k-Equation sub-grid scale (SGS) closure model. The computational methodology was a second-order finite volume scheme implemented within the OpenFOAM libraries. Time-stepping was performed with a second-order backwards scheme in increments limited by the Courant-Friedrichs–Lewy (CFL) condition of $CFL < 1$, producing high-fidelity time-accurate flows.

The turbine was rotated by means of an arbitrary mesh interface (AMI), or a slip boundary, between the rotating mesh of the turbine and the outer mesh (Fig. 5.7). The inflow had a uniform velocity profile at the inlet and a constant pressure at the outlet. The three-dimensional domain was periodic in the spanwise direction with a computational width of $0.2c$. Slip walls were implemented

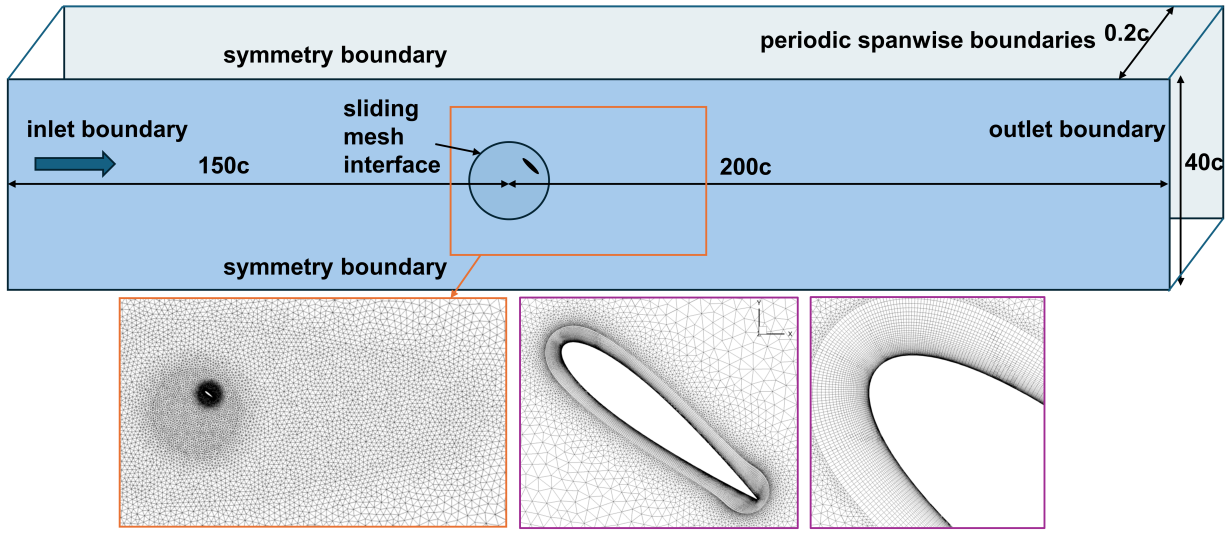

Figure 5.7: Computational domain, boundary conditions, and images of the mesh resolution close to the blade.

on edges of the domain (orthogonal to the freestream flow direction) that impose an equivalent 2D blockage with respect to the width of the computational domain, W, such that $D/W = 0.106$.

The mesh was a body-fitted and structured close to the blade with $y^+ < 1$ on the suction surface of a non-rotating mesh. Outside the boundary layer region, the mesh transitioned to an unstructured format to reduce computational costs. The computational methodology closely follows that previously reported [10, 43]. Mesh independence and SGS model sensitivity are discussed in [10].

The simulations had a Reynolds number of $Re_c = 45,000$ and were performed at $\lambda = 1.4, 1.9, 2.4, 3.3$ and 4.3 by increasing the rotational speed of the blade region and holding all other parameters constant. The blade forces were computed in the frame of reference of the computational domain $(x - y)$ by integrating the normal and viscous stresses over the blade profile at

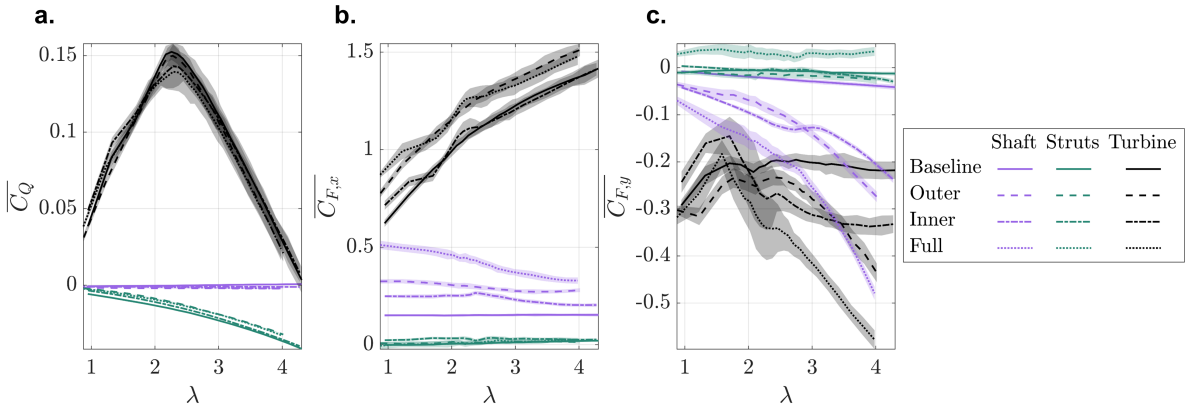

Figure 5.8: Comparison between experimental time-averaged (a) performance (b) thrust force, and (c) lateral force coefficients for the shaft, the struts, and the full turbine. The shaded areas describe the standard deviation of time-average performance over individual cycles at each λ.

every time-step. These were converted to normal and tangential components through a coordinate transform based on blade orientation. The torque coefficient was computed by the cross-product of the resultant force on the blade and the distance from the center of pressure to the rotational axis. The tangential and normal force coefficients are computed via Equations 5.15 and 5.16. As for experiments, the pitching moment coefficient of the blade can thus be solved from Equation 5.17.

5.3 *Results*

Experimental time-averaged torque and forcing for the turbine, struts, and shaft for the four shaft configurations are presented in Figure 5.8. The shaft has a minimal influence on $\overline{C_Q}$, with most of the parasitic torque stemming from the struts (Figure 5.8a). Because of this, the spread in $\overline{C_Q}$ for the different shaft types is on the order of the standard deviation of time-averaged performance of individual cycles (Figure 5.8a). There are no appreciable interactions between the shaft and strut (i.e., changing the shaft size does not appreciably affect strut torque or force). In contrast, as hypothesized, thrust and lateral forcing on the shaft is significant, depends on the shaft configuration, and is the largest contributor to forcing on the support structure (Figure 5.8b,c). Therefore, the

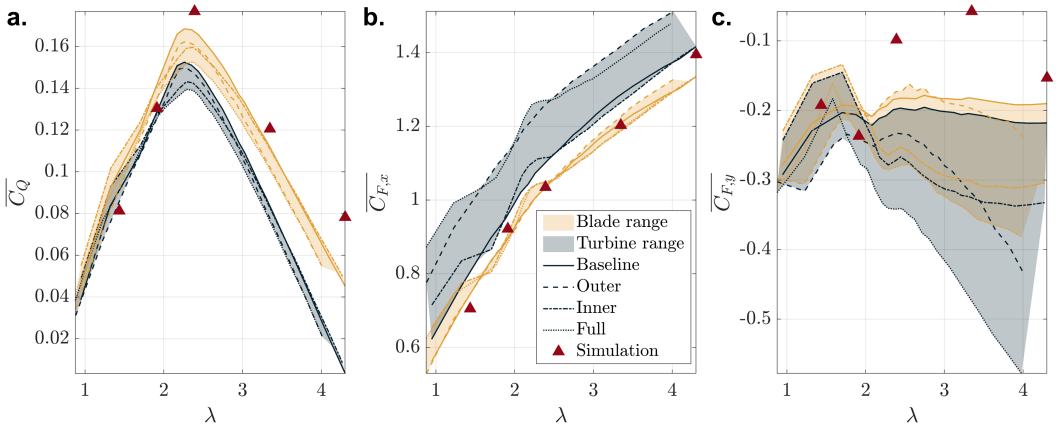

Figure 5.9: Time-averaged (a) torque (b) thrust force, and (c) lateral force coefficients for the full turbine, the blades, and the simulations. The spread of the colored area corresponds to the range of the time-averaged values of the different shaft configurations (Figure 5.3).

different shaft configurations provide a useful test case for isolating blade-level forces from turbine-level measurements. In agreement with canonical rotating shaft work [101], the thrust force coefficient (proxy to cylinder drag) decreases and the magnitude of the lateral force coefficient (proxy to cylinder lift from the Magnus effect) increases as the tip-speed ratio increases. Cases with the same shaft diameter outside of the blade span, such as the "Baseline" and "Inner" cases, have comparable turbine-level thrust despite a 200% increase in the shaft diameter inside the blade span for the "Inner" case. This supports the assumption underpinning the "Scaled Shaft" superposition strategy: forcing on the shaft within the blade span is relatively inconsequential in the turbine-level force balance.

5.3.1 Comparison of the Torque, Thrust, and Lateral Force Coefficients

Experimental time-averaged torque and forces at the turbine and blade levels for the different shaft configurations are compared to the simulation results in Figure 5.9. Blade-level torque is elevated relative to turbine-level torque once parasitic support structure torque is accounted for, thrust decreases when shaft loads are accounted for, and lateral forces increase when the induced

lift on the spinning cylinder are accounted for. Additionally, the spread (shaded areas) between the different shaft types is substantially reduced for the blade-level thrust and lateral coefficients relative to the turbine-level forcing. Despite induction differences and potential secondary interactions between the turbine components neglected in the superposition, we observe a nearly complete convergence in blade-level thrust. The remaining spread in blade-level thrust between the shaft types is comparable to the standard deviation of time-averaged performance between cycles (Figure 5.8a,b). Time-averaged thrust is always positive, increases with tip-speed ratio, and is significantly larger than the lateral force. The time-averaged lateral force is always negative and, at the blade level, is less sensitive to the tip-speed ratio than thrust. For torque and force coefficients, coefficients from direct blade-level simulation are closer to estimated blade-level values from experiment than the turbine-level values. Simulation and blade-level experimental values diverge for torque and thrust beyond $\lambda = 1.9$ and agreement in the lateral force coefficient is worse for $\lambda > 1.9$. In experiments, the time-averaged lateral shaft force is comparable to the turbine lateral force, particularly for $\lambda > 1.9$ (Figure 5.8). Therefore, the lateral force coefficient may be the more sensitive to imperfect assumptions about shaft forces in the superposition strategy.

Phase-averaged coefficients from experiments and simulations are compared in Figure 5.10 for five tip-speed ratios. Aside from differences in thrust at low tip-speed ratios, the turbine- and blade-level coefficients appear nearly identical in the phase averages. This is partially a consequence of axis scale, where the range of values experienced throughout the cycle masks differences in the phase averages that are on the order of those in the time averages. Thrust is positive throughout the rotation (except for in the downstream sweep at $\lambda \geq 3.3$) and the lateral force oscillates about zero. While lateral forcing on the shaft is a large contribution to turbine time-averaged lateral forcing (Figures 5.8 and 5.9), the phase-average lateral forcing on the turbine is dominated by the blades. For some tip-speed ratios, the differences between the blade-level and simulation data are larger in the phase averages than in the time averages (e.g., C_Q, C_X, and C_Y at $\lambda = 1.9$). In these cases, the time-averaged agreement between simulations and the experiments results from amplitude differences throughout the rotation canceling out. In general, the agreement in the trends across phase between the experiments and simulations are excellent for all coefficients.

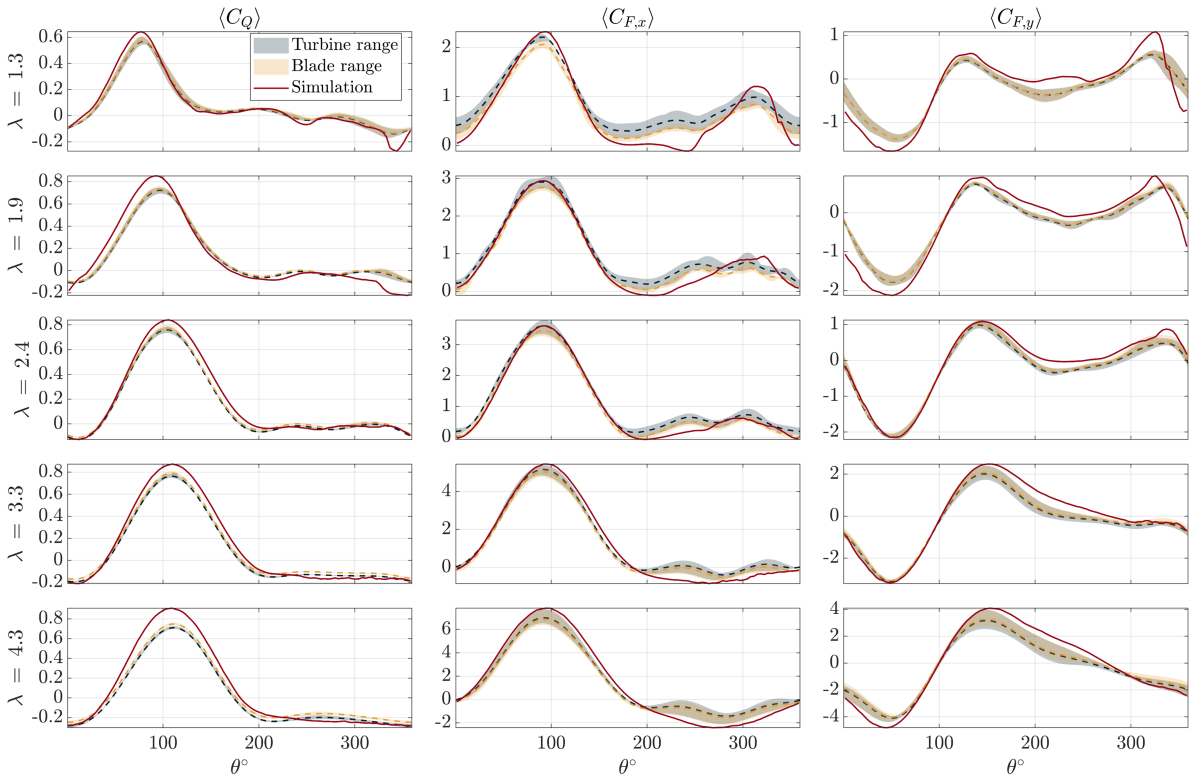

Figure 5.10: Phase-averaged, torque, thrust force, and lateral force coefficients. The colored area corresponds to the spread between phase-averages for the different shaft types and the dashed line represents the average of the different shaft types (Figure 5.3). Note: because of data availability the $\lambda = 1.3$ experiments are compared with simulation data at $\lambda = 1.4$. The experimental turbine and blade ranges for $\lambda = 1.3$ utilize "Outer" and "Full" data at $\lambda = 1.2$. For $\lambda = 4.3$ the turbine and blade ranges utilize "Outer" and "Full" data at $\lambda = 4$.

5.3.2 Comparison of the Tangential Force and Pitching Moment Coefficients

Given the strong agreement in the time- and phase-averaged torque, thrust, and lateral force coefficients between the experiments and simulation results, we now consider the phase-averaged coefficients contributing to torque generation (Equation 5.17). The tangential force and pitching moment coefficients are presented in Figures 5.11 and 5.12, respectively. Accounting for the shaft

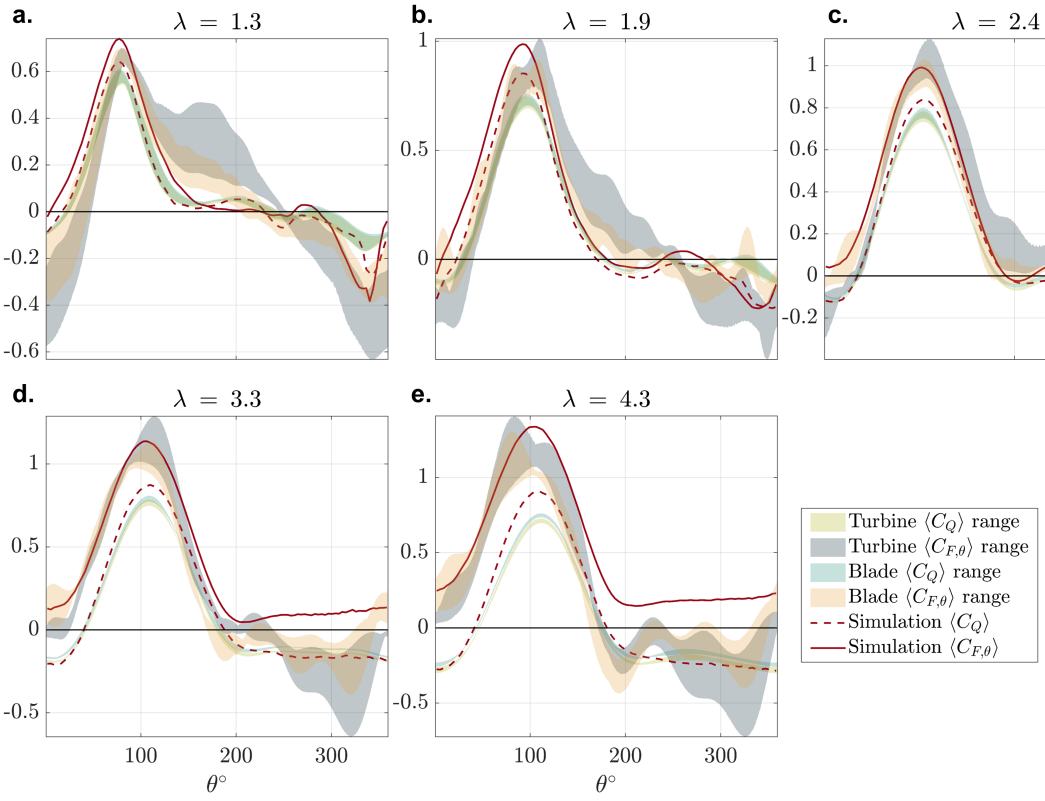

Figure 5.11: Phase-averaged torque and tangential force coefficients. The colored area corresponds to the phase-averaged spread between the different shaft configurations (Figure 5.3). Note: because of data availability the $\lambda = 1.3$ experiments are compared with simulation data at $\lambda = 1.4$. The experimental turbine and blade ranges for $\lambda = 1.3$ utilize "Outer" and "Full" data at $\lambda = 1.2$. For $\lambda = 4.3$ the turbine and blade ranges utilize "Outer" and "Full" data at $\lambda = 4$.

and support structures through the blade-level force estimation reduces the spread in the tangential force and pitching moment coefficients for the different shaft configurations across all tip-speed ratios, consistent with expectations for blade-level forcing being independent of shaft configuration. Further, the blade-level computation generally improves the agreement with simulations.Differences between the experimental turbine- and blade-level tangential force and pitching moment coefficients are sizeable. This demonstrates the importance of isolating blade-level forces to estimate these

terms from experimental data.

The blade-level and simulation tangential force coefficients have good quantitative agreement at all phases until about $\lambda = 2.4$ (Figure 5.11a-c). Beyond this tip-speed ratio, the results diverge in the downstream sweep where the simulation values become increasingly positive and the experimental values increasingly negative (Figure 5.11d-e), potentially due to differences in drag (see Section 5.4). For both the experiments and simulations, the tangential force coefficient follows the torque coefficient, but with an amplitude offset that increases with the tip-speed ratio. This offset is a consequence of the pitching moment contribution to torque (Equation 5.17).

The blade-level pitching moment coefficients have good quantitative agreement between experiments and simulations, particularly for the upstream sweep (Figure 5.12). As for the tangential force coefficient, agreement with simulation is improved for blade-level estimates, with the closest agreement for $\lambda = 1.3-2.4$ (Figure 5.12a-c). For these tip-speed ratios, there is good agreement for the majority of the rotation, but there are regions where the simulation values are always negative while some shaft configurations have positive blade-level C_M values. This occurs in the first half of the upstream sweep for $\lambda = 1.3$ (a) and $\lambda = 1.9$ (b), and the later half of the downstream sweep for the $\lambda = 2.4$ case (c). For $\lambda \geq 2.4$ (d-e), the simulation and experimental results begin to diverge beyond $\theta = 100°$ where the simulation data have smaller amplitudes and are more negative but still share commonalities with experimental trajectories.

Because of the relatively large range in estimated pitching moment in experiments, particularly prior to isolating blade-level tangential force, trends in the pitching moment across tip-speed ratio are not obvious. For clarity, phase-averaged blade-level pitching moments for the "Baseline" shaft and the simulation data are presented in Figure 5.12f,g. As the tip-speed ratio increases, the range of pitching moments experienced throughout the rotation decreases and the pitching moment approaches a constant, negative value. This trend agrees with results by Le Fouest et al. [11] and are consistent with decreased dynamic stall severity at higher tip-speed ratios. Virtual camber and convergence towards more steady-state aerodynamics likely explain the trend towards a negative value on average. As discussed in Chapter 4, as the tip-speed ratio increases, induction increases and intracycle variations in the relative velocity and angle of attack are reduced, particularly in the

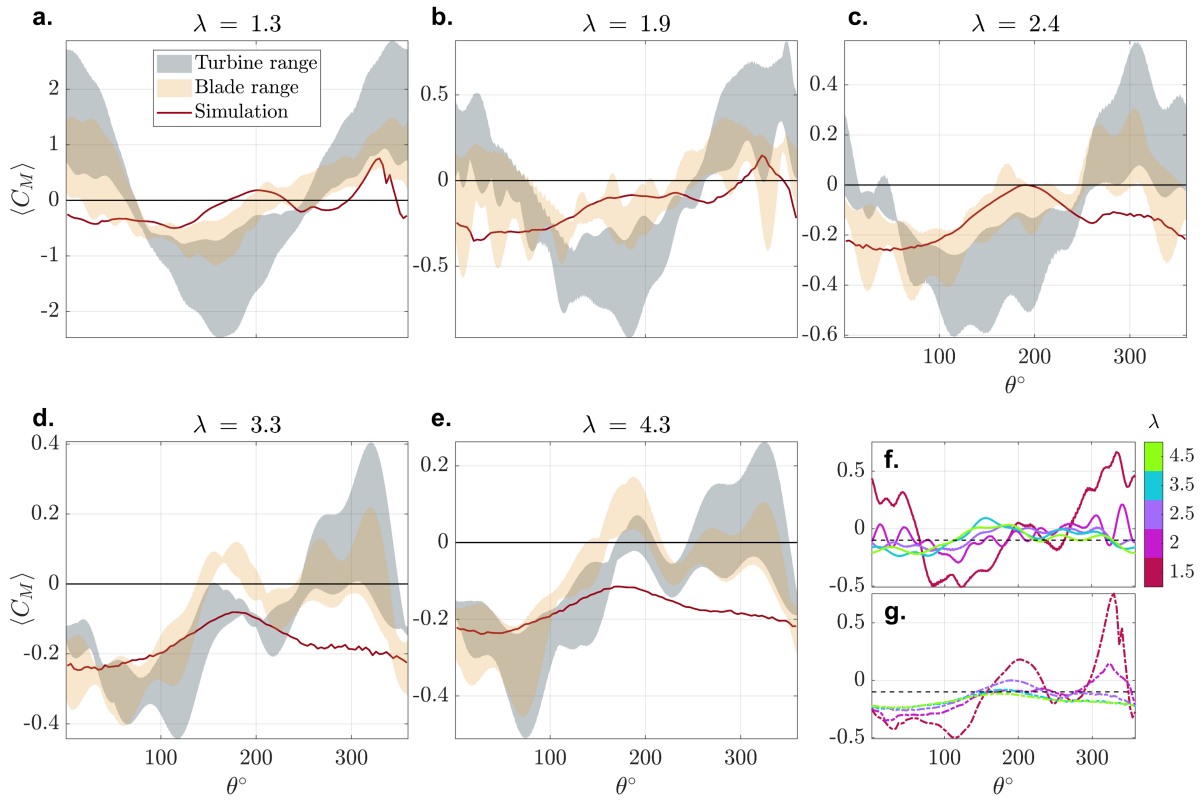

Figure 5.12: (a-e) Phase-averaged pitching moment coefficient. The colored area corresponds to the phase-averaged spread between the different shaft configurations (Figure 5.3). (f) Experimental pitching moment as a function of λ for the "Baseline" shaft and (g) the same from simulation. The pitching moment for a NACA 6418 under low-to-moderate angles of attack is plotted (dashed line, $C_M \approx -0.1$) for reference in (f) and (g). Note: because of data availability the $\lambda = 1.3$ experiments are compared with simulation data at $\lambda = 1.4$. The experimental turbine and blade ranges for $\lambda = 1.3$ utilize "Outer" and "Full" data at $\lambda = 1.2$. For $\lambda = 4.3$ the turbine and blade ranges utilize "Outer" and "Full" data at $\lambda = 4$.

downstream sweep. Under these conditions, the relative velocity is determined by the tip-speed ratio and the angle of attack is determined by the preset pitch angle and virtual incidence. It is hypothesized in Chapter 4 that, at high tip-speed ratios, the pitching moment would converge toward

a modest negative value in the downstream sweep. The experimentally-estimated pitching moment values in the downstream sweep at the highest tip-speed ratios are consistent with this hypothesis, as they closely match a NACA 6418 at low-to-moderate angles of attack, $-4 \geq \alpha \leq 12$ (Figure 5.12f). This foil has a profile similar to virtual camber estimated for the high tip-speed ratio limit: maximum camber of $\approx 6\%$ occurring between the quarter and half chord locations (following the zero inflow formulation from [17]).

While there are differences between the simulation and the experiments, the overall agreement is encouraging. Blade-level thrust between the shaft types nearly collapses in the time average. The phase-averaged collapse in blade-level forcing between the shaft types is imperfect but is significant in comparison to phase-average differences in turbine-level forcing. These results support the suitability of the "Scaled Shaft" strategy for isolating blade-level torque and force components from measurements at the axis of rotation.

5.4 *Discussion*

Having established the general suitability of the superposition strategy, we now discuss overall trends, contributions, and implications of the estimated blade forces and moments. We focus on the "Baseline" shaft case and the simulation phase-averaged results, as shown in Figure 5.13. The experimental torque coefficient (a) becomes relatively insensitive to λ at high tip-speed ratios for most of the upstream sweep but becomes increasingly negative in the downstream sweep. The experimental tangential force coefficient (c) behaves similarly in the upstream sweep, but contrary to torque, is nearly zero for much of the downstream sweep and generally independent of tip-speed ratio. This suggests a balance between the lift and drag coefficients, the relative velocity, and the projection of the aerodynamic forces into the direction of rotation. In contrast, the pitching moment contribution to torque (e) has a strong dependence on λ throughout rotation. Due to the λ^2 amplification of the pitching moment to torque, this term becomes increasingly detrimental at the higher tip-speed ratios even as C_M converges towards a small, constant value. The normal force coefficient (g) increases continuously with the tip-speed ratio, likely because lift becomes increasingly normal to the direction of rotation and increases in magnitude. The simulation results

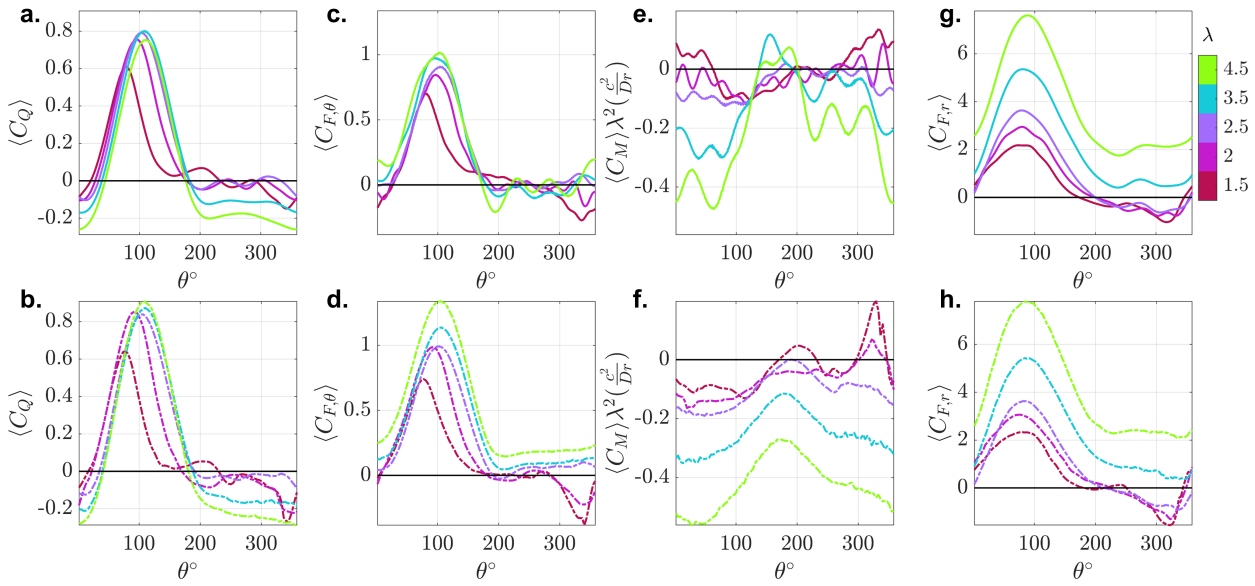

Figure 5.13: Blade-level (a,b) torque coefficient, (c,d) tangential force coefficient, (e,f) pitching moment contribution to torque, and (g,h) the normal force contribution for (top row) experiments and (bottom row) simulation. Note: the $\lambda = 1.3$ experiments are compared with simulation at $\lambda = 1.4$.

(b,d,f,h) largely agree with the experimental results except $C_{F,\theta}$. Unlike for the experiments, the simulation $C_{F,\theta}$ continues to increase at high tip-speed ratios, even becoming consistently positive in the downstream sweep. The deviation in trends could stem from limitations to the superposition strategy. However, the excellent agreement in the normal force between experiments and simulations suggest that this discrepancy could be driven by differences in drag. This could be a consequence of higher skin friction on the experimental blade compared to the smooth blade in simulation, or other simulation errors related to drag prediction in unsteady, separated flows. Ultimately, the larger simulation tangential force contributions are balanced out by more detrimental simulation pitching moment contributions, resulting in good agreement with experimental torque.

The normal force coefficient is always positive for the highest two tip-speed ratios, signifying

that the suction side never switches to the outside of the foil as it does for the lower tip-speed ratios in the downstream sweep. Virtual camber and incidence likely explain this. The virtual incidence for this geometry is $\approx 6°$, resulting in a $0°$ angle of attack. If we again consider NACA 6418 data, lift would point towards the center of rotation for angle of attack values ≥ -5, so it follows that the side closest to the axis of rotation is always the suction side at high tip-speed ratios.

5.4.1 Influence of the Pitching Moment on Turbine Performance

Chapter 4 demonstrates that the continual degradation in the downstream sweep performance is what determines the maximum turbine-level performance and the optimal tip-speed ratio. Using our new methodology, we can isolate the contributions of the tangential force (combination of the tangential projections of lift and drag) and the pitching moment to performance in the upstream and downstream sweep (Figure 5.14). The upstream contribution is computed by averaging blade-level values between $\theta = 0°$ and $\theta = 180°$. A corresponding calculation is used for the downstream contribution. The upstream and downstream contributions are scaled by 1/2 such that their sum is equal to the time-average. For the full rotation (a), upstream sweep (b), and downstream sweep (c), the difference between the tangential contribution and total performance increases continuously with λ, driven by an increasingly significant and detrimental contribution by the pitching moment. While the pitching moment contribution is almost entirely responsible for the performance degradation in the downstream sweep (c), its magnitude is relatively similar between the upstream and downstream sweeps, meaning that differences in the tangential force contribution drive performance differences between the two regions. Specifically, the tangential force term outweighs the detrimental pitching moment term in the upstream sweep, but is nearly neutral in the downstream sweep. These results highlight the importance of the pitching moment to cross-flow turbine performance; a stark contrast to the assumption following from Strickland [97] that the pitching moment is inconsequential to turbine performance. Analytical models like DMST should consider the pitching moment contribution. This is a topic worthy of further experimental and numerical investigation, given that reductions to the pitching moment could substantially improve time-average performance.

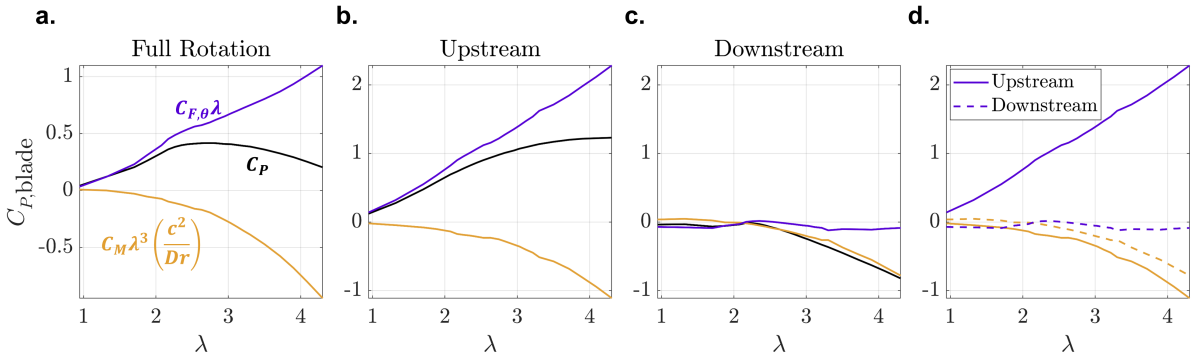

Figure 5.14: (a) Full rotation (time average), and (b) upstream and (c) downstream segment-averaged, blade-level performance compared to the corresponding tangential force and pitching moment contributions. (d) Comparison between the tangential force and pitching moment performance contributions between the upstream and downstream sweeps.

5.4.2 Implications to Turbine Design

The turbine- and blade-level force components have implications for structural design. Turbine-level thrust and lateral forces act on the turbine superstructures (e.g., support structures external to the turbine, foundation, anchors) and result in overturning moments on the turbine system that must be accounted for. Our results underscore the importance of considering force maximums in the design of cross-flow systems, as the averages are often not descriptive of maximum loads. As an example, time-averaged thrust is substantially higher than the lateral force, but the force ranges experienced throughout the rotation are comparable (Figure 5.10). At the blade-level, the study of the normal and tangential forces and the pitching moment provide insight for robust blade design. For instance, the normal force does not contribute to power but is the largest component of blade-level fluid forcing. In these experiments, the normal force coefficient can be up to six times the tangential force coefficient drives blade bending stresses and shear at the mounting points.

Single-bladed turbines are unlikely to be utilized in practice, but studying their blade-level force components can inform the design of multi-bladed turbines. Moreover, the methods in this work may be applied to multi-bladed turbines with two caveats. First, since forces are measured at the

center of rotation, $F^{\star}_{x,\text{blade}}$, $F^{\star}_{y,\text{blade}}$, and $Q^{\star}_{\text{blade}}$ contributions from individual blades are unknown. Second, because of this, the total tangential force from all the blades remains unknown, and the pitching moment cannot be solved for. However, applying the "Scaled Shaft" strategy to multi-bladed turbines could illuminate how aggregate blade-level thrust and lateral forcing differ with geometry and experimental conditions. This analysis is necessary for decoupling blade-level force trends from those of the support structures, especially for experiments where these are substantial. However, the aggregate blade-level force represents the sum of phase-shifted, oscillatory, individual blade forces that may constructively or destructively add. Therefore, it is unlikely the aggregate forces are representative of the range of forces experienced by an individual blade throughout the rotation. The number of blades will undoubtedly affect the force ranges experienced by an individual blade, but studying this requires direct blade-level force measurements. Finally, in one regard, the validity of the "Scaled Shaft" strategy may improve when applied to multi-bladed devices since induction would increase with blade count [19], meaning the loading on the shaft within the blade-span is increasingly negligible.

5.5 *Conclusion*

Consideration of blade-level forces and torques is key to demystifying the fundamental operation of cross-flow turbines and improving their structural design. To identify blade-level hydrodynamic forces and torques from experimental measurements at the axis of rotation, we define a "Scaled Shaft" superposition strategy. The accuracy of this method is demonstrated through the reasonable collapse in blade-level force and torque coefficients between turbine experiments consisting of four different shaft configurations, and strong agreement with equivalent blade-only simulations. Overall, the "Scaled Shaft" strategy is an empirical approach that works well for our single-bladed turbine geometry because it is consistent with the flow physics and, competing factors not included in the model, such as the velocity difference between the inside and outside of the blade-shaft connections (Figure 5.2), are largely offsetting. Factors such as higher blockage, non-ideal inflows, and more substantial blade-shaft connections (e.g., disc end plates) may reduce the efficacy of the "Scaled Shaft" strategy. In those cases, forcing on the blade-shaft connections could begin to differ

substantially between when the blades are present versus when they are not, and adjustments to our approach may be required.

Isolation of experimental blade-level torque and forces facilitates the study of the normal force, tangential force, and pitching moment coefficients. The normal force is the largest component of blade-level forcing, increases continuously with the tip-speed ratio, and is important for blade and mounting point design. Turbine performance is a function of the tangential force and pitching moment coefficients. The tangential force contribution is representative of trends in the upstream sweep and is largely responsible for differences between the upstream and downstream sweeps, while the pitching moment contribution is detrimental throughout the rotation and drives the continuous performance degradation in the downstream sweep. These results underscore the general importance of studying the pitching moment and that failing to consider this component results in an over-prediction of turbine performance by a large margin, particularly at high tip-speed ratios. This is relevant to improving analytical models, such as double multiple streamtube theory. By the same token, reductions to this detrimental term through geometry or control could improve cross-flow turbine performance.

Chapter 6

CONCLUSION

Cross-flow turbines have several potential benefits over axial-flow devices in wind and water applications but have complex fluid dynamics that are not yet sufficiently understood. This thesis considers the fundamental operation of these devices, contributes new methods to their study, and yields performance, force, and flow-field data for simulation validation. The chapters herein complement current cross-flow turbine literature by focusing on areas that have received limited research attention. Chapters 3 - 5 characterize a single-bladed cross-flow turbine in a uniform inflow with a specific focus on understanding the linkages between the near-blade fluid dynamics, performance, and blade-level forcing on a phase-averaged basis. Actual deployments of cross-flow turbines will likely use multi-bladed devices, but the knowledge gained by this research effort can inform improvements in turbine and blade design, control strategies, and modeling across a wide range of geometries.

Chapter 3, quantifies the cycle-to-cycle variability present in flow-field and performance measurements for two contrasting operational conditions via an unsupervised flow-field clustering pipeline. This clustering approach contributes to our understanding of the relationship between the near-blade fluid dynamics and performance while also providing a more comprehensive picture of the phase-varying flow fields than possible with aggregate, statistical representations. Specifically, we observe physically meaningful clusters representing a series of distinct flow-field evolutions that reveal variations in the timing of the dynamic stall process, consistent with observed variations in performance and inflow velocity. The practical applicability of this approach is a means to conditionally average data. It may be especially useful in lab and field environments with higher turbulence intensities.

Chapter 4 demonstrates the critical operational importance of the previously understudied down-

stream sweep while deciphering the interplay between rotor geometry, fluid dynamics, operating conditions, and turbine kinematics. To determine the drivers of performance degradation in the downstream sweep, performance and flow-field measurements were studied in concert for three different operating conditions. Due to interactions with the rotor and upstream disturbances, the inflow velocity diverges sharply from the free stream conditions in the downstream sweep, the momentum available for power production is reduced, and the orientation of lift and drag become increasingly unfavorable for power production. As a result, power consumption from the downstream sweep increases approximately linearly beyond the optimal tip-speed ratio and strongly influences maximum time-averaged performance. This finding is shown to be consistent across performance experiments with 55 unique combinations of geometry and Reynolds number. Induction renders the common analytical descriptions of the kinematics inaccurate, particularly in the downstream sweep, and drives the convergence to a limiting case with steady-state aerodynamics. Reaching the limiting case likely requires unrealistically high tip-speed ratios and induction than seen in cross-flow systems, but this model is useful for framing our understanding of high tip-speed ratio operation and trends.

Chapter 5 introduces a "Scaled Shaft" superposition methodology for isolating blade-level force components from force measurements at the axis of rotation. This work provides a basis for studying the terms contributing to performance and forcing and facilitates more detailed investigations into turbine operation and structural design. In doing so, the significance of the pitching moment term is illuminated. For the geometry studied, this term is shown to be detrimental to performance and to drive the downstream performance degradation identified in Chapter 4. Failing to consider the pitching moment contribution results in a substantial over-prediction of cross-flow turbine performance and further development of reduced-order modeling methods should consider the pitching moment, in addition to lift and drag.

6.1 *Future Work*

This thesis provides a set of well-characterized benchmark cases from which to contextualize future works that consider different turbine geometries, kinematics, or non-ideal inflows. Generally, future

studies should caution leaning on the nominal kinematic definitions to explain dynamics, particularly in the downstream sweep, and should consider performance changes throughout the entire rotation, the influence of virtual camber, and the tangential force and pitching moment contributions. Blade-level loads will undoubtedly change as more blades are added, so multi-bladed devices should be studied. Doing so experimentally would require instrumentation of individual blades, warranting further development of those capabilities.

This work highlights complex relationships between the fluid dynamics and performance of cross-flow turbines in an idealized experimental environment subject to uniform inflows with minimal freestream turbulence (turbulence intensity of $\approx 1-2\%$). Future work should consider non-ideal inflows with shear and higher turbulence more representative of conditions in the field. In field settings or laboratory conditions with higher turbulence, or the use of torque control, cycle-specific tip-speed ratios could be perturbed further from the phase-average. For such conditions, performance and hydrodynamic variability may increase, making a conditional-averaging technique like the clustering approach presented in Chapter 3 more necessary. In this work the clusters were based on the flow fields, but PIV data collection is time-intensive and generally confined to laboratory settings, so investigating the benefits of clustering on the basis of cross-flow turbine performance and forcing could be a direction for future research.

The downstream sweep is critical to overall performance and ways to reduce detrimental downstream torque should be considered. As recommended in Chapter 4, altering the pitching moment, reducing the drag coefficient, or increasing the lift coefficient could improve performance in the downstream sweep. The pitching moment largely drives the downstream performance degradation (Chapter 5), warranting a parametric study of the pitching moment for this purpose. A study of this type should consider different chord-to-radius ratios (affecting virtual camber) and blade profiles. Additionally, because large gradients exist and off-optimal operation is important when shedding power above the rated inflow velocity, a wide range of tip-speed ratios should be tested, not just the optimal performance point. The large parameter space necessary may render simulations cost-prohibitive, but the "Scaled Shaft" framework may enable cost-effective experimental campaigns.

Chapter 4 highlights how changes to geometric parameters like the preset pitch angle commonly affect the upstream and downstream sweeps differently. This finding supports the benefits of developing active or passive control strategies capable of individualized control between the upstream and downstream sweeps. Active pitch control is promising for performance improvement and load reductions [48] and deserves further study. Passive options have found success in axial flow turbines [102] and their application to cross-flow turbines could improve the practical applicability of individualized control.

Appendix A

PERFORMANCE AND FLOW-FIELD UNCERTAINTY ANALYSIS

The presented results involve relatively subtle, but statistically significant, observations in the performance and flow-field data. Despite the uncertainties in both data sets, we find statistically meaningful correlations between the different data streams that are in line with theory and current understanding (e.g., statistically meaningful correlations between the flow-field clusters obtained through PIV and measured performance).

A.1 Performance Uncertainty

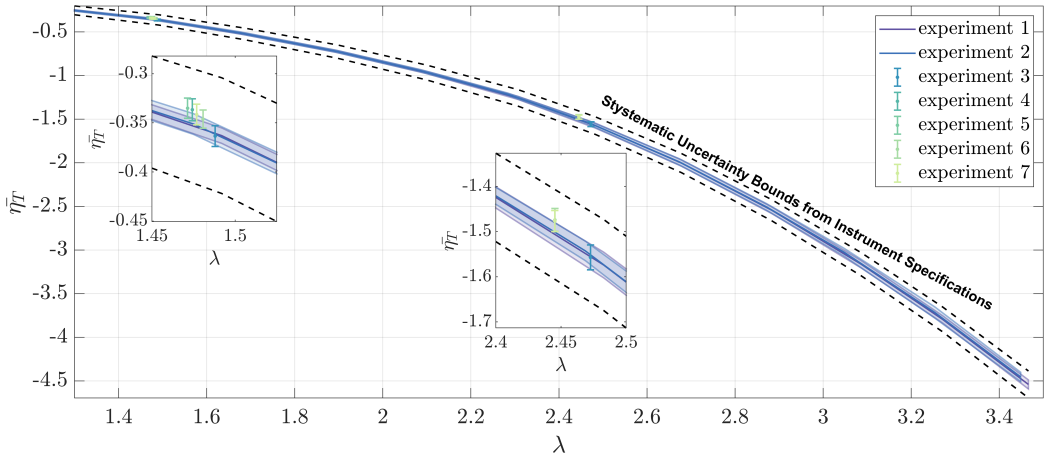

Figure A.1: Time-averaged full turbine performance measurements. The shaded regions and error bars represent ± two standard deviations in the cycle-averaged performance distributions. The dashed black lines represent the systematic uncertainty bounds computed following the methodology in [4]. The error bars for experiments 3-7 are best shown in the insets.

Table A.1: Instrument uncertainty for performance testing

Instrument	C_P	**Unit**	**Systematic Uncertainty**
Nortek Vectrino	U_∞^3	m/s	Sensor Accuracy: ±1% of measured values ±1 mm/s [a]
Motor Encoder	θ	degrees	Sensor accuracy: ±0.004
Futek FSH02595	τ	N-m	Sensor non-linearity: 0.2% of rated load Sensor hysteresis: ±0.2% of rated load Sensor non-repeatability: ±0.05% of rated load [b]

[a] U_∞ systematic uncertainty converted to U_∞^3 systematic uncertainty by converting the listed values to a percentage of U_∞ and multiplying by 3

[b] Summed as root sum of square, rated output of 11.3 N-m yields ±0.0325 N-m

One approach to assessing uncertainty is a formal analysis based on instrument accuracy. However, in performing such an analysis, two issues are encountered. First, the cycle-to-cycle variation that is the focus of this work would be treated as a random uncertainty in a formal analysis. Second, as subsequently shown, the systematic uncertainty indicated by a formal analysis exceeds the experimentally-observed variation.

Cross-flow turbine performance is a function of the measured hydrodynamic torque (Futek FSH02595 torque cell), the rotation rate (derivative of the measured position from the motor encoder), and the freestream velocity (Nortek Vectrino ADV). These measurements are all subject to systematic and random uncertainties. Systematic uncertainty describes the ability of the instrumentation to accurately determine the central moment, while random uncertainties are related to the variability around the central moment.

The systematic uncertainty for η_T (full turbine performance) is quantified following the methodology in Appendix A of [4]. The systematic uncertainties, as taken from the manufacturer specifications, are listed in Table A.1, and these bounds are shown relative to experimental performance for the full turbine in Figure A.1. Experimental repeatability is excellent, as evidenced by the small variations in cycle-averaged performance within and across repeated performance measurements.

Further, the systematic uncertainty estimated from the instrumentation specifications exceeds the observed variability. We note that the uncertainty analysis is done for the full turbine efficiency. It would be inappropriate to perform this analysis on the blade-level efficiency since the strut subtraction methodology involves independent measurements of the full turbine and the struts in isolation.

Given that we are less concerned with the absolute accuracy of the central moment of the distribution given by the systematic uncertainty, it is more instructive to consider the characteristics of the variability in blade-level efficiency around the central moment. The phase-averaged performance perturbations are defined as the difference between performance in a specific cycle relative to the phase-average of all cycles, so the variance (second moment) of the performance perturbations in each cluster is given as

$$\alpha_2 = \frac{1}{n}\sum(\eta')^2. \tag{A.1}$$

Substantial differences in the variance of the two clusters would suggest that the two distributions have different fundamental structure and that a comparison of their mean values (first moment) could be misleading, as well as invalidate the use of the Wilcoxon rank sum test used in Sections 3.3.2-3.3.3.

Similarly, the skewness (third moment) is given as

$$\alpha_3 = \frac{1}{n}\sum(\eta')^3. \tag{A.2}$$

A value of zero skewness would signify that the performance trajectories in a cluster are normally distributed around the phase-average of all cycles (i.e., cluster trajectories are randomly distributed). Conversely, positive values would signify that performance within a cluster is skewed above the phase-average and vice-versa for negative values.

Figure A.2 presents these moments for both tip-speed ratios. Figure A.2i-ii shows blade-level performance and performance perturbations for all trajectories (as presented in Figure 3.9). Here, the black lines denote the first moment of the distribution, emphasizing the relatively subtle trends in the underlying distribution of trajectories assigned to each cluster. We observe that the phase-average variance trends for each cluster are similar (Figure A.2iii), which shows that the cycles in

each cluster are similarly dispersed with respect to the phase-average of all cycles. This validates the use of the Wilcoxon rank sum test and comparisons between the phase-averages are meaningful. However, because variance is always positive, this does not show how the clusters are distributed

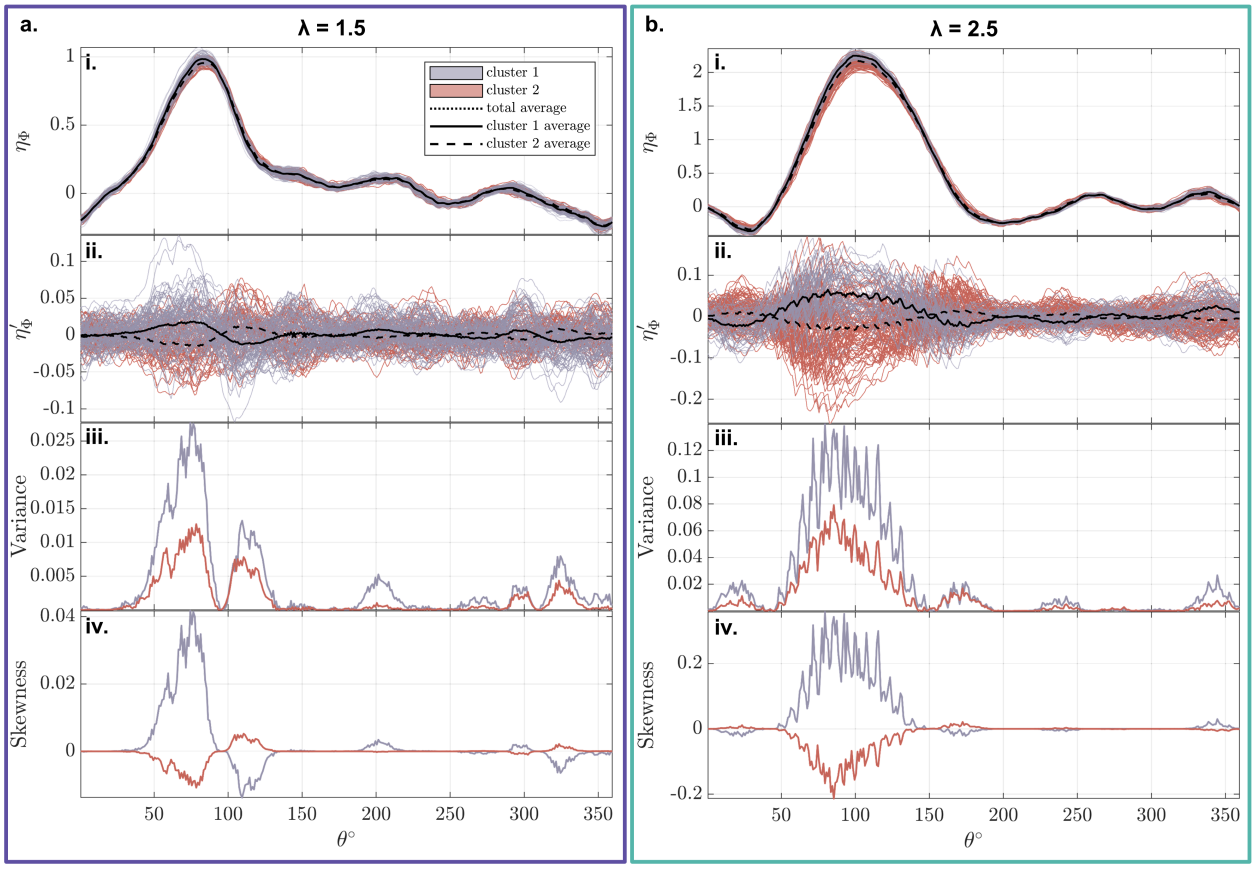

Figure A.2: Statitical analysis of the performance trajectories associated with the flow-field clusters for (a) $\lambda = 1.5$ and (b) $\lambda = 2.5$.(i) Performance trajectories and (ii) performance perturbations. The black lines represent the cluster conditional-averages for performance or performance perturbations (Equations 3.2 and 3.3). (iii) Variance (Equation A.1) in the performance trajectories associated with each cluster. (Bottom) Skewness (Equation A.2) for each cluster relative to the phase-average of all cycles.

.

with respect to the phase-average of all cycles. For both tip-speed ratios, the skewness (Figure A.2iv) shows that the performance trajectories associated with each cluster are not randomly distributed around the phase-average of all cycles and that they are skewed in opposing directions. If the cycle-to-cycle variability was all attributed to random uncertainty, the observed correlations between the performance and the flow-field clusters would not be present. While random uncertainty is certainly still present, the results presented in this work provide confidence that the cycle-to-cycle variation is driven by physical processes (i.e., inflow perturbations).

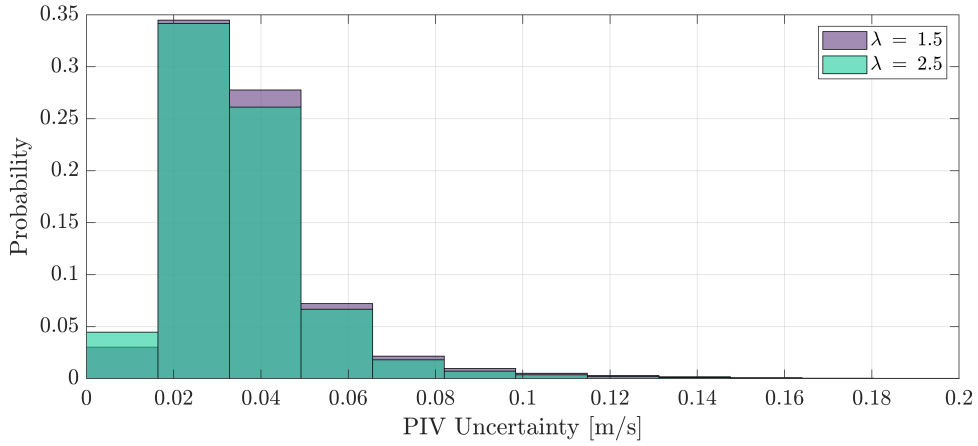

Figure A.3: Histograms PIV uncertainty for every vector across all phases for $\lambda = 1.5$ and $\lambda = 2.5$.

.

A.2 PIV Uncertainty

The PIV uncertainty is quantified by the correlation method employed in LaVision DaVis [**?**] which analyses individual pixel contributions to the correlation peak. The output is an uncertainty field corresponding to each individual flow field (i.e N=139 uncertainty fields at each phase corresponding to the N=139 flow fields at each phase). Histograms of PIV uncertainty for every vector across all phases are given in Figure A.3. The PIV uncertainty is ±0.037 m/s on average (average of all vectors across all phases for a specific tip-speed ratio) for $\lambda = 1.5$ and ±0.035 m/s for $\lambda = 2.5$.

These uncertainties are an order of magnitude smaller than the cycle-to-cycle variability observed in the flow fields (Figure 3.9).

Appendix B

LIMITING CASE FULL DERIVATION

For cross-flow turbines operating at sufficiently high tip-speed ratios and/or subject to significant induction, there exists a theoretical limiting case where the relative velocity, U_{rel}, is equal to the tangential velocity, $r\omega$. The corresponding angle of attack, α, is equal to the sum of the preset pitch angle, α_p, and the virtual incidence resulting from rotational effects. Under these conditions, the lift force acts normal to rotation and does not contribute to torque while the drag force, F_D, directly opposes rotation. Here we derive an analytical model for cross-flow turbine performance based on this limiting case. All steady-state aerodynamic coefficients should be determined based on the virtually cambered foil geometry. Cross-flow turbine torque, Q_{lim}, for a given chord-to-radius ratio, c/r, and α_p is then a function of the drag coefficient, $C_D(C_v, \alpha)$, and the pitching moment coefficient, $C_M(C_v, \alpha)$. The drag coefficient is formally defined as

$$C_D = \frac{F_D}{\frac{1}{2}\rho(r\omega)^2 Sc}, \tag{B.1}$$

where H is the blade span. Similarly, the pitching moment coefficient is formally defined as

$$C_M = \frac{M_P}{\frac{1}{2}\rho(r\omega)^2 Sc^2}. \tag{B.2}$$

Cross-flow turbine torque is the sum of the drag and moment contributions as

$$Q_{lim} = -C_D \frac{1}{2}\rho(r\omega)^2 Hcr + C_M \frac{1}{2}\rho(r\omega)^2 Sc^2. \tag{B.3}$$

The coefficient of torque in the limiting case is then

$$C_{Q,lim} = \frac{-C_D \frac{1}{2}\rho(r\omega)^2 Scr + C_M \frac{1}{2}\rho(r\omega)^2 Sc^2}{\frac{1}{2}\rho U_\infty^2 SDr}, \tag{B.4}$$

We note that $D \neq 2r$ because the diameter is defined by the blade outer surface, while the radius is defined by the distance to the quarter chord. So that we can formulate the result in terms of the

chord-to-radius ratio, we multiply the denominator by $\frac{r}{r}$ and simplify as

$$Q_{lim} = \frac{-C_D \frac{1}{2}\rho(r\omega)^2 Scr + C_M \frac{1}{2}\rho(r\omega)^2 Sc^2}{\frac{1}{2}\rho U_\infty^2 S(D\frac{r}{r})r}. \tag{B.5}$$

$$Q_{lim} = \lambda^2 \frac{-C_D cr + C_M c^2}{r^2(\frac{D}{r})}. \tag{B.6}$$

$$C_{Q,lim} = \frac{r}{D}\left[-C_D\frac{c}{r} + C_M\left(\frac{c}{r}\right)^2\right]\lambda^2, \tag{B.7}$$

and the coefficient of performance, $C_{P,lim}$ reduces to

$$C_{P,lim} = \frac{r}{D}\left[-C_D\frac{c}{r} + C_M\left(\frac{c}{r}\right)^2\right]\lambda^3. \tag{B.8}$$

Appendix C

MEASUREMENT OF THE PRODUCT OF ROTATING MASS AND RADIUS TO THE CENTER OF MASS

To determine the product of the rotating mass and radius to the center of mass, mr_g, we run the turbine in still air by commanding a range of sinusoidal ω profiles with different amplitudes and then apply Newton's second law. We assume the aerodynamic forces in still air are negligible in comparison to the hydrodynamic forces in moving water. The sum of forces in the streamwise, x, and cross-stream, y, directions are then written as

$$\cancelto{0}{F_x^\star(t)} = mr_g(-\omega(t)^2 sin\theta(t) + \dot{\omega}(t)cos\theta(t)) + F_{\mathrm{m},x}(t), \tag{C.1}$$

and

$$\cancelto{0}{F_y^\star(t)} = mr_g(\omega(t)^2 cos\theta(t) - \dot{\omega}(t)sin\theta(t)) + F_{\mathrm{m},y}(t). \tag{C.2}$$

mr_g is then solved for

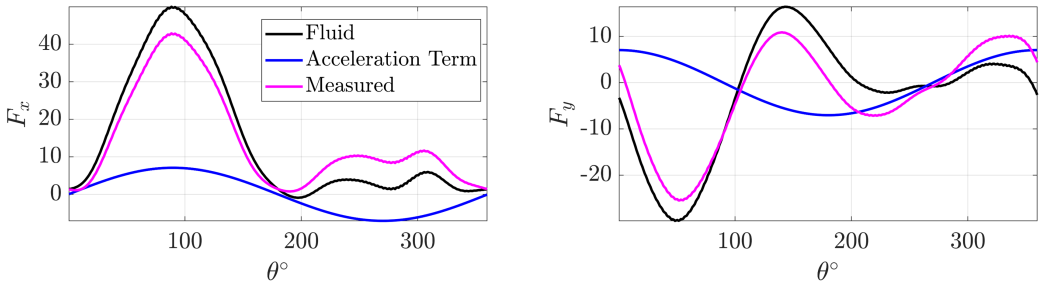

Figure C.1: phase-averaged fluid, acceleration, and measured force terms from Equations 5.10 and 5.11.

$$mr_g = \frac{-F^{\star}_{\mathrm{m},x}(t)}{\omega(t)^2 sin\theta(t) - \dot{\omega}(t) cos\theta(t)} \tag{C.3}$$

$$mr_g = \frac{-F^{\star}_{\mathrm{m},y}(t)}{-\omega(t)^2 cos\theta(t) - \dot{\omega}(t) sin\theta(t)} \tag{C.4}$$

A low-pass, zero-phase, Butterworth filter with 11 Hz cutoff frequency is applied to the measurements to remove high-frequency electromagnetic interference from the time series data. Then mr_g is computed via Equations C.3 and C.4 at each time-step. The median of the mr_g time-series is taken resulting in two mr_g constants (one from $F_{\mathrm{m},x}$ measurements and the other from $F_{\mathrm{m},y}$ measurements). These values are then averaged together as a best estimate for mr_g. This procedure is repeated for the for different turbine/shaft configurations.

Even under constant speed control, the acceleration terms, $mr_g\omega^2 \sin\theta$ and $-mr_g\omega^2 \sin\theta$ in the x and y directions respectively (Equations 5.10 and 5.11), are significant as shown in Figure C.1.

Appendix D

SUPERPOSITION STRATEGY DETAILS

To determine blade-level quantities via "Scaled Shaft" superposition of independent data sets with slightly varying experimental conditions, we need to estimate forces and torques on the different support components at the turbine experimental conditions. For example, the strut forcing at the turbine experimental conditions, denoted as Ψ, is computed as

$$\langle \vec{F}^{\star}_{\text{struts}}|\Psi\rangle \;=\; \langle \vec{F}^{\star}_{\text{sups}}|\Psi\rangle - \langle \vec{F}^{\star}_{\text{shaft}}|\Psi\rangle. \tag{D.1}$$

The fluid force on any component at the turbine conditions equals the fluid force coefficient of that component multiplied by the dimensional conditions corresponding to the turbine experimental conditions, $\boldsymbol{D}_{\Psi}$. Substituting, non-dimensionalizing $\vec{F}^{\star}_{\text{struts}}|\Psi$, and simplifying yields

$$\boldsymbol{C}_{\text{struts}} \;=\; \frac{\langle \vec{F}^{\star}_{\text{struts}}|\Psi\rangle}{\boldsymbol{D}_{\Psi}} \;=\; \frac{\langle \boldsymbol{C}_{\text{sups}}\rangle \cancel{\boldsymbol{D}_{\Psi}}}{\cancel{\boldsymbol{D}_{\Psi}}} - \frac{\langle \boldsymbol{C}_{\text{shaft}}\rangle \cancel{\boldsymbol{D}_{\Psi}}}{\cancel{\boldsymbol{D}_{\Psi}}}, \tag{D.2}$$

$$\langle \boldsymbol{C}_{\text{struts}}\rangle \;=\; \langle \boldsymbol{C}_{\text{sups}}\rangle - \langle \boldsymbol{C}_{\text{shaft}}\rangle. \tag{D.3}$$

We follow the same procedure to determine the blade-level coefficients but also need to account for differences in the dynamic depth between experiments when the blade is present versus when absent. This arises for the same static depth due to differences in flow resistance. While static depth could be adjusted in an *ad hoc* manner to match dynamic depth, this would be time consuming. The dynamic depth of the shaft-only case is represented as H_{Υ} and the dynamic depth for the turbine experiments is represented as H_{Ψ}. The proportion of force on the shaft outside of the turbine span is then evaluated as $\langle \vec{F}^{\star}_{\text{blade}}|\Psi\rangle \frac{H_{\Psi}-S'}{H_{\Upsilon}}$ and the blade-level forcing is computed as.

$$\langle \vec{F}^{\star}_{\text{blade}}|\Psi\rangle \;=\; \langle \vec{F}^{\star}_{\text{turb}}|\Psi\rangle - \langle \vec{F}^{\star}_{\text{struts}}|\Psi\rangle - \langle \vec{F}^{\star}_{\text{blade}}|\Psi\rangle \frac{H_{\Psi}-S'}{H_{\Upsilon}}. \tag{D.4}$$

The blade-level coefficients are determined as

$$\langle \boldsymbol{C}_{\text{blade}} \rangle = \frac{\langle \vec{F}^{\star}_{\text{blade}} | \Psi \rangle}{\boldsymbol{D}_{\Psi}} = \frac{\langle \boldsymbol{C}_{\text{sups}} \rangle \cancel{\boldsymbol{D}_{\Psi}}}{\cancel{\boldsymbol{D}_{\Psi}}} - \frac{\langle \boldsymbol{C}_{\text{shaft}} \rangle \cancel{\boldsymbol{D}_{\Psi}}}{\cancel{\boldsymbol{D}_{\Psi}}} - \frac{\langle \boldsymbol{C}_{\text{shaft}} \rangle \cancel{\boldsymbol{D}_{\Psi}}}{\cancel{\boldsymbol{D}_{\Psi}}} \frac{H_{\Psi} - S'}{H_{\Upsilon}} \tag{D.5}$$

$$\langle \boldsymbol{C}_{\text{blade}} \rangle = \langle \boldsymbol{C}_{\text{turb}} \rangle - \langle \boldsymbol{C}_{\text{struts}} \rangle - \langle \boldsymbol{C}_{\text{shaft}} \rangle \frac{H_{\Psi} - S'}{H_{\Upsilon}}. \tag{D.6}$$

The forcing on the blade-shaft connections and on the shaft likely depends on the Reynolds number and the tip-speed ratio. The freestream velocity varies slightly between full turbine experiments and experiments without the blade (supports and shaft-only) because of how the presence of the turbine affects the incoming flow for a given command frequency to the flume pumps. As a result, the tip-speed ratio and the Reynolds number vary slightly between experiments. In this work, the actual experimental Reynolds number varied only slightly ($< 1\%$) between corresponding turbine, supports, and shaft experiments and is likely inconsequential. To account for the slight variations in λ between experiments, we interpolated the support and shaft coefficients to the corresponding turbine tip-speed ratios.

This approach is contrasted to the superposition strategy presented in Strom et al. [84] where the blade-level coefficients are computed as

$$\langle \boldsymbol{C}_{\text{blade}} \rangle = \langle \boldsymbol{C}_{\text{turb}} \rangle - \langle \boldsymbol{C}_{\text{sups}} \rangle. \tag{D.7}$$

Time-averaged, blade-level torque, thrust, lateral, and tangential force coefficients computed via the "Scaled Shaft" strategy and the Strom et al. strategy are compared to the blade-level simulation and turbine-level results in Figure D.1. As expected, the two superposition strategies result in almost identical blade-level torque because torque on the shaft is negligible. Both superposition strategies decrease the magnitude of thrust and the lateral force relative to the turbine-level results. The "Scaled Shaft" strategy has excellent agreement with the simulation time-averaged thrust coefficient and has a physical basis. Therefore, while the Strom et al. strategy tracks the simulations better for the lateral force coefficient at some tip-speed ratios, the "Scaled Shaft" strategy is employed in this work. The time-averaged tangential force coefficient is insensitive to the superposition strategy because of offsetting differences across phase in the phase-averages.

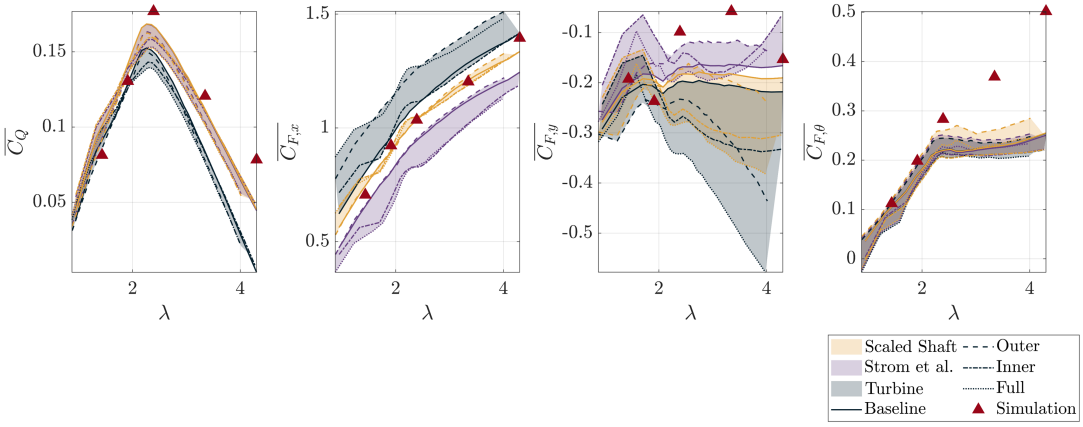

Figure D.1: Time-averaged torque, thrust force, lateral force, and tangential force coefficients for the full turbine, the blades (from the "Scaled Shaft" and "Strom et al." strategies), and the simulations. The spread of the colored area corresponds to the range of the time-averaged values of the different shaft configurations (Figure 5.3).

BIBLIOGRAPHY

[1] W. Timmer. Two-dimensional low-reynolds number wind tunnel results for airfoil naca 0018. *Wind engineering 32(6), 525-537*, 32, 12 2008.

[2] Bastian Bechtold. *Violin Plots for Matlab*. Github Project, 2016.

[3] Aidan Hunt, Benjamin Strom, Gregory Talpey, Hannah Ross, Isabel Scherl, Steven Brunton, Martin Wosnik, and Brian Polagye. A parametric evaluation of the interplay between geometry and scale on cross-flow turbine performance. *arXiv preprint arXiv:2310.20616*, 2023.

[4] Robert J. Cavagnaro and Brian Polagye. Field performance assessment of a hydrokinetic turbine. *International Journal of Marine Energy*, 14:125–142, 2016.

[5] M. Mahmood, N. Hayat, A. U. Farooq, Z. Ali, S. R. Jamil, and Z. Hussain. Vertical axis wind turbine – a review of various configurations and design techniques. *Renewable and Sustainable Energy Reviews*, 16(4):1926 – 1939, 2012.

[6] S. Eriksson, H. Bernhoff, and M. Leijon. Evaluation of different turbine concepts for wind power. *Renewable and Sustainable Energy Reviews*, 12(5):1419 – 1434, 2008.

[7] Isabel Scherl, Benjamin Strom, Steven L. Brunton, and Brian L. Polagye. Geometric and control optimization of a two cross-flow turbine array. *Journal of Renewable and Sustainable Energy*, 12(6):064501, 12 2020.

[8] J. O. Dabiri. Potential order-of-magnitude enhancement of wind farm power density via counter-rotating vertical-axis wind turbine arrays. *Journal of Renewable and Sustainable Energy*, 3(4):1–12, 2011.

[9] Mukul Dave, Benjamin Strom, Abigale Snortland, Owen Williams, Brian Polagye, and Jennifer A. Franck. Simulations of intracycle angular velocity control for a crossflow turbine. *AIAA Journal*, 59(3):812–824, mar 2021.

[10] Mukul Dave and Jennifer A. Franck. Comparison of rans and les for a cross-flow turbine in confined and unconfined flow. *Journal of Renewable and Sustainable Energy*, 13(6):064503, 2021.

[11] Sébastien Le Fouest and Karen Mulleners. The dynamic stall dilemma for vertical-axis wind turbines. *Renewable Energy*, 198:505–520, 2022.

[12] A. Bianchini, F. Balduzzi, F. Ferrara, and L. Ferrari. Virtual incidence effect on rotating airfoils in darrieus wind turbines. *Energy Conversion and Management*, 111:329 – 338, 2016.

[13] C. Simão Ferreira, G. Van Kuik, G. Van Bussel, and F. Scarano. Visualization by PIV of dynamic stall on a vertical axis wind turbine. *Experiments in Fluids*, 46(1):97–108, 2009.

[14] A-J. Buchner, M. W. Lohry, L. Martinelli, J. Soria, and A. J. Smits. Dynamic stall in vertical axis wind turbines: Comparing experiments and computations. *Journal of Wind Engineering and Industrial Aerodynamics*, 146:163 – 171, 2015.

[15] R. Dunne and B. McKeon. Dynamic stall on a pitching and surging airfoil. *Experiments in Fluids*, 56, 08 2015.

[16] H-C Tsai and T. Colonius. Coriolis effect on dynamic stall in a vertical axis wind turbine. *AIAA Journal*, 54(1):216–226, 2016.

[17] P. G. Migliore, W. P. Wolfe, and J. B. Fanucci. Flow curvature effects on darrieus turbine blade aerodynamics. *Journal of Energy*, 4(2):49–55, 1980.

[18] Abdolrahim Rezaeiha, Hamid Montazeri, and Bert Blocken. Characterization of aerodynamic performance of vertical axis wind turbines: Impact of operational parameters. *Energy Conversion and Management*, 169:45–77, 2018.

[19] Abdolrahim Rezaeiha, Hamid Montazeri, and Bert Blocken. Towards optimal aerodynamic design of vertical axis wind turbines: Impact of solidity and number of blades. *Energy*, 165:1129–1148, 2018.

[20] Qing'an Li, Takao Maeda, Yasunari Kamada, Junsuke Murata, Kento Shimizu, Tatsuhiko Ogasawara, Alisa Nakai, and Takuji Kasuya. Effect of solidity on aerodynamic forces around straight-bladed vertical axis wind turbine by wind tunnel experiments (depending on number of blades). *Renewable Energy*, 96:928–939, 2016.

[21] Abdolrahim Rezaeiha, Ivo Kalkman, and Bert Blocken. Effect of pitch angle on power performance and aerodynamics of a vertical axis wind turbine. *Applied Energy*, 197:132–150, 2017.

[22] Han-Wen Chi. *The Influence of Preset Pitch on the Performance of Cambered Foils within Cross-flow Turbines*. PhD thesis, 2024.

[23] Hannah Ross and Brian Polagye. Effects of dimensionless parameters on the performance of a cross-flow current turbine. *Journal of Fluids and Structures*, 114:103726, 2022.

[24] H. Ross and B. Polagye. An experimental assessment of analytical blockage corrections for turbines. *Renewable Energy*, 152:1328 – 1341, 2020.

[25] H. Beri and Y. Yao. Double Multiple Stream Tube Model and Numerical Analysis of Vertical Axis Wind Turbine. *Energy and Power Engineering*, 3:262–270, 2011.

[26] Ion Paraschivoiu. Double-multiple streamtube model for darrieus in turbines. *NASA. Lewis Research Center Wind Turbine Dyn.*, 1981.

[27] M. Abdul Akbar and V. Mustafa. A new approach for optimization of vertical axis wind turbines. *Journal of Wind Engineering and Industrial Aerodynamics*, 153:34–45, 2016.

[28] Mico Pucci, Stefania Zanforlin, Debora Bellafiore, and Georg Umgiesser. A dmst-based tool to establish the best aspect ratio, solidity and rotational speed for tidal turbines in real sea conditions, 2022.

[29] A. A. Ayati, K. Steiros, M. A. Miller, S. Duvvuri, and M. Hultmark. A Double Multiple Streamtube model for Vertical Axis Wind Turbines of arbitrary rotor loading. *Wind Energy Science*, 4(4):653–662, 2019.

[30] Jonathan Murray and Matthew Barone. The development of cactus, a wind and marine turbine performance simulation code. *49th AIAA Aerospace Sciences Meeting including the New Horizons Forum and Aerospace Exposition*.

[31] Martin Wosnik, Pete Bachant, Vincent Sinclair Neary, and Andrew W. Murphy. Evaluation of design and analysis code, cactus, for predicting crossflow hydrokinetic turbine performance. Technical report, 9 2016.

[32] T. Lee and P. Gerontakos. Lee, t., & gerontakos, p. *Journal of Fluid Mechanics*, 512:313–341, 2004.

[33] Hanns Friedrich Müller-Vahl. Wind turbine blade dynamic stall and its control, doctoral thesis, technical university of berlin. 2015.

[34] J.-P. Küppers and T. Reinicke. A wavenet-based fully stochastic dynamic stall model. *Wind Energy Science Discussions*, 2022:1–24, 2022.

[35] K. Mulleners and M. Raffel. The onset of dynamic stall revisited. *Exp Fluids*, 52:779 – 793, 2012.

[36] A. Choudhry, R. Leknys, M. Arjomandi, and R. Kelso. An insight into the dynamic stall lift characteristics. *Experimental Thermal and Fluid Science*, 58:188–208, 10 2014.

[37] Philippe Wernert, Wolfgang Geissler, Markus Raffel, and Juergen Kompenhans. Experimental and numerical investigations of dynamic stall on a pitching airfoil. *AIAA Journal*, 34(5):982–989, 1996.

[38] P. Ouro, T. Stoesser, and L. Ram. Effect of Blade Cambering on Dynamic Stall in View of Designing Vertical Axis Turbines. *Journal of Fluids Engineering*, 140(June):1–12, 03 2018.

[39] Z. Wang and M. Zhuang. Leading-edge serrations for performance improvement on a vertical-axis wind turbine at low tip-speed-ratios. *Applied Energy*, 208:1184 – 1197, 2017.

[40] Nidiana Rosado Hau, Lin Ma, Derek Ingham, and Mohamed Pourkashanian. A critical analysis of the stall onset in vertical axis wind turbines. *Journal of Wind Engineering and Industrial Aerodynamics*, 204:104264, 2020.

[41] N. Fujisawa and S. Shibuya. Observations of dynamic stall on turbine blades. *Journal of Wind Engineering and Industrial Aerodynamics*, 89(2):201–214, 2001.

[42] J. M. Edwards, L. Angelo Danao, and R. J Howell. Novel experimental power curve determination and computational methods for the performance analysis of vertical axis wind turbines. *ASME. J. Sol. Energy Eng.*, 134(4), 2012.

[43] Mukul Dave and Jennifer A. Franck. Analysis of dynamic stall development on a cross-flow turbine blade. *Phys. Rev. Fluids*, 8:074702, Jul 2023.

[44] A. Rezaeiha, H. Montazeri, and B. Blocken. Characterization of aerodynamic performance of vertical axis wind turbines: Impact of operational parameters. *Energy Conversion and Management*, 169:45 – 77, 2018.

[45] K.M. Almohammadi, D.B. Ingham, L. Ma, and M. Pourkashanian. Modeling dynamic stall of a straight blade vertical axis wind turbine. *Journal of Fluids and Structures*, 57:144–158, 2015.

[46] Sébastien Le Fouest, Daniel Fernex, and Karen Mulleners. Time scales of dynamic stall development on a vertical-axis wind turbine blade. *Flow*, 3:E11, 2023.

[47] Qing'an Li, Takao Maeda, Yasunari Kamada, Junsuke Murata, Kazuma Furukawa, and Masayuki Yamamoto. Measurement of the flow field around straight-bladed vertical axis wind turbine. *Journal of Wind Engineering and Industrial Aerodynamics*, 151:70–78, 04 2016.

[48] Karen Mulleners Sébastien Le Fouest. Optimal blade pitch control for enhanced vertical-axis wind turbine performance. *Nature Communications*, 15, 2024.

[49] Lawrence W Carr, Kenneth W McAlister, and William J McCroskey. Analysis of the development of dynamic stall based on oscillating airfoil experiments. Technical report, 1977.

[50] W. J. McCroskey. The Phenomenon of Dynamic Stall. Technical report, 1981.

[51] Gordon J Leishman. *Principles of helicopter aerodynamics with CD extra*. Cambridge university press, 2006.

[52] K. Mulleners and M. Raffel. Dynamic stall development. *Exp Fluids*, 54, 2013.

[53] A. Snortland, O. Williams, and B. Polagye. Influence of near-blade hydrodynamics on cross-flow turbine performance. *Proceedings of the 13th European Wave and Tidal Energy Conference*, pages 1 – 9, 2019.

[54] Claudio A Consul, Richard H J Willden, and Simon C McIntosh. Blockage effects on the hydrodynamic performance of a marine cross-flow turbine. *Philosophical Transactions of the Royal Society A: Mathematical, Physical and Engineering Sciences*, 371(1985):20120299, 2013.

[55] Nitin Kolekar and Arindam Banerjee. Performance characterization and placement of a

marine hydrokinetic turbine in a tidal channel under boundary proximity and blockage effects. *Applied Energy*, 148:121–133, 2015.

[56] Thomas Kinsey and Guy Dumas. Impact of channel blockage on the performance of axial and cross-flow hydrokinetic turbines. *Renewable Energy*, 103:239–254, 2017.

[57] Chris Garrret and Patrick Cumins. The efficiency of a turbine in a tidal channel. *Journal of Fluid Mechanics*, 588:243–251, 2007.

[58] Abigale Snortland, Isabel Scherl, Brian Polagye, and Owen Williams. Cycle-to-cycle variations in cross-flow turbine performance and flow fields. *Experiments in Fluids*, 64, 2023.

[59] M. Lennie, J. Steenbuck, B. R. Noack, and C. O. Paschereit. Cartographing dynamic stall with machine learning. *Wind Energy Science*, 5(2):819–838, 2020.

[60] Graham Riches, Robert Martinuzzi, and Chris Morton. Proper orthogonal decomposition analysis of a circular cylinder undergoing vortex-induced vibrations. *Physics of Fluids*, 30(10):105103, 2018.

[61] Tanner Harms, Pourya Nikoueeyan, and Jonathan W. Naughton. *An Experimental Evaluation of Cycle-to-Cycle Variations of Dynamic Stall*. 2018.

[62] Manikandan Ramasamy, Jacob Wilson, William McCroskey, and Preston Martin. Characterizing cycle-to-cycle variations in dynamic stall measurements. *Journal of the American Helicopter Society*, 63, 04 2018.

[63] M. Miller, S. Duvvuri, I. Brownstein, M. Lee, J. Dabiri, and M. Hultmark. Vertical-axis wind turbine experiments at full dynamic similarity. *Journal of Fluid Mechanics*, 844:707–720, 2018.

[64] Mark Miller, Subrahmanyam Duvvuri, and Marcus Hultmark. Solidity effects on the performance of vertical-axis wind turbines. *Flow*, 1, 01 2021.

[65] Peter Bachant, Martin Wosnik, Budi Gunawan, and Vincent S. Neary. Experimental study of a reference model vertical-axis cross-flow turbine. *PLOS ONE*, 11(9):1–20, 09 2016.

[66] K. K. Y. Tsang, R. M. C. So, R. C. K. Leung, and X. Q. Wang. Dynamic stall behavior from unsteady force measurements. *Journal of Fluids and Structures*, 24(1):129 – 150, 2008.

[67] Manikandan Ramasamy, Armaun Sanayei, Jacob S Wilson, Preston B Martin, Tanner Harms, Pourya Nikoueeyan, and Jonathan Naughton. Reducing uncertainty in dynamic stall measurements through data-driven clustering of cycle-to-cycle variations. *Journal of the American Helicopter Society*, 66(1):1–17, 2021.

[68] K. Beyer, J. Goldstein, R. Ramakrishnan, and U. Shaft. When is nearest neighbor meaningful? *University of Wisconsin-Madison Department of Computer Sciences*, 1998.

[69] K. Taira, S. Brunton, S. Dawson, C. Rowley, T. Colonius, B. McKeon, O. Schmidt, S. Gordeyev, V. Theofilis, and L. Ukeiley. Modal analysis of fluid flows: An overview. *AIAA Journal*, 55, 02 2017.

[70] Steven L. Brunton and J. Nathan Kutz. *Data-Driven Science and Engineering: Machine Learning, Dynamical Systems, and Control*. Cambridge University Press, 2019.

[71] Isabel Scherl, Benjamin Strom, Jessica K. Shang, Owen Williams, Brian L. Polagye, and Steven L. Brunton. Robust principal component analysis for modal decomposition of corrupt fluid flows. *Phys. Rev. Fluids*, 5:054401, May 2020.

[72] Hans-Peter Kriegel, Peer Kröger, and Arthur Zimek. Clustering high-dimensional data: A survey on subspace clustering, pattern-based clustering, and correlation clustering. *ACM Trans. Knowl. Discov. Data*, 3(1), mar 2009.

[73] Michael C. Thrun and Alfred Ultsch. Using projection-based clustering to find distance- and density-based clusters in high-dimensional data. *Journal of Classification*, 38(2):1432–1343, 2021.

[74] Tom Wester, Sirko Bartholomay, Dominik Traphan, Michael Hölling, Joachim Peinke, and Gerd Guelker. Using high speed piv measurements and pod to solve the mystery of dynamic stall. 07 2018.

[75] Joel L. Weightman, Omid Amili, Damon Honnery, Julio Soria, and Daniel Edgington-Mitchell. Signatures of shear-layer unsteadiness in proper orthogonal decomposition. *Experiments in Fluids*, 59(12), 2018.

[76] Karen Mulleners and Markus Rütten. Analysis of intermittent trailing-edge vortex shedding using recurrence plots. *AIAA Journal*, 56(2):571–580, 2018.

[77] Geert De Soete and J. Douglas Carroll. K-means clustering in a low-dimensional euclidean space. In Edwin Diday, Yves Lechevallier, Martin Schader, Patrice Bertrand, and Bernard Burtschy, editors, *New Approaches in Classification and Data Analysis*, pages 212–219, Berlin, Heidelberg, 1994. Springer Berlin Heidelberg.

[78] Chris Ding and Xiaofeng He. K-means clustering via principal component analysis. In *Proceedings of the Twenty-First International Conference on Machine Learning*, ICML '04, page 29. Association for Computing Machinery, 2004.

[79] Irem Ersöz Kaya, Ayça Çakmak Pehlivanlı, Emine Gezmez Sekizkardeş, and Turgay Ibrikci. Pca based clustering for brain tumor segmentation of t1w mri images. *Computer Methods and Programs in Biomedicine*, 140:19–28, 2017.

[80] Claudia Canali and Riccardo Lancellotti. Improving scalability of cloud monitoring through pca-based clustering of virtual machines. *Journal of Computer Science and Technology*, 29(1):38–52, 2014.

[81] Zhe Bai, Steven L. Brunton, Bingni W. Brunton, J. Nathan Kutz, Eurika Kaiser, Andreas Spohn, and Bernd R. Noack. *Data-Driven Methods in Fluid Dynamics: Sparse Classification from Experimental Data*, pages 323–342. Springer International Publishing, Cham, 2017.

[82] Eurika Kaiser, Bernd R. Noack, Laurent Cordier, Andreas Spohn, Marc Segond, Markus Abel, Guillaume Daviller, Jan Östh, Siniša Krajnović, Robert K. Niven, and et al. Cluster-based reduced-order modelling of a mixing layer. *Journal of Fluid Mechanics*, 754:365–414, 2014.

[83] Aditya G. Nair, Chi-An Yeh, Eurika Kaiser, Bernd R. Noack, Steven L. Brunton, and Kunihiko Taira. Cluster-based feedback control of turbulent post-stall separated flows. *Journal of Fluid Mechanics*, 875:345–375, 2019.

[84] Benjamin Strom, Noah Johnson, and Brian Polagye. Impact of blade mounting structures on cross-flow turbine performance. *Journal of Renewable and Sustainable Energy*, 10(3):034504, 2018.

[85] Aidan Hunt, Carl Stringer, and Brian Polagye. Effect of aspect ratio on cross-flow turbine performance. *Journal of Renewable and Sustainable Energy*, 12(5):054501, 2020.

[86] Brian Polagye, Ben Strom, Hannah Ross, Dominic Forbush, and Robert J. Cavagnaro. Comparison of cross-flow turbine performance under torque-regulated and speed-regulated control. *Journal of Renewable and Sustainable Energy*, 11(4):044501, 2019.

[87] Jerry Westerweel and Fulvio Scarano. Universal outlier detection for piv data. *Experiments in Fluids*, 39:1096–1100, 12 2005.

[88] Joe H. Ward Jr. Hierarchical grouping to optimize an objective function. *Journal of the American Statistical Association*, 58(301):236–244, 1963.

[89] H. B. Mann and D. R. Whitney. On a Test of Whether one of Two Random Variables is Stochastically Larger than the Other. *The Annals of Mathematical Statistics*, 18(1):50 – 60, 1947.

[90] Philippe Druault and Grégory Germain. Prediction of the tidal turbine power fluctuations from the knowledge of incoming flow structures. *Ocean Engineering*, 252:111180, 2022.

[91] Jim Thomson, Brian Polagye, Vibhav Durgesh, and Marshall C Richmond. Measurements of turbulence at two tidal energy sites in puget sound, wa. *IEEE Journal of Oceanic Engineering*, 37(3):363–374, 2012.

[92] Karen Mulleners Sébastien Le Fouest. Optimal blade pitch control for enhanced vertical-axis wind turbine performance. *Nature Communications*, 15, 2024.

[93] R.A. McAdam, G.T. Houlsby, and M.L.G. Oldfield. Experimental measurements of the hydrodynamic performance and structural loading of the transverse horizontal axis water turbine: Part 2. *Renewable Energy*, 59:141–149, 2013.

[94] Aidan Bharath, Hannah Ross, Casey Nichols, Andrew Simms, Mark Murphy, Robert Raye, Patrick O'Byrne, Michael Monahan, and Martin Wosnik. Open water blade strain measurements on a vertical-axis tidal turbine: Paper no. omae2023-101076. 2023. ASME 2023 42nd International Conference on Ocean, Offshore and Arctic Engineering ; Conference date: 11-06-2023 Through 16-06-2023.

[95] Effect of number of blades on aerodynamic forces on a straight-bladed vertical axis wind turbine. *Energy*, 90:784–795, 2015.

[96] Alessandro Bianchini, Francesco Balduzzi, Giovanni Ferrara, and Lorenzo Ferrari. Aerodynamics of Darrieus Wind Turbines Airfoils: The Impact of Pitching Moment. *Journal of Engineering for Gas Turbines and Power*, 139(4):042602, 11 2016.

[97] J H Strickland. Darrieus turbine: a performance prediction model using multiple streamtubes. Technical report.

[98] Gabriele Bedon, Marco Raciti Castelli, and Ernesto Benini. Optimization of a darrieus vertical-axis wind turbine using blade element – momentum theory and evolutionary algorithm. *Renewable Energy*, 59:184–192, 2013.

[99] Ye Li and Sander M. Calisal. Three-dimensional effects and arm effects on modeling a vertical axis tidal current turbine. *Renewable Energy*, 35(10):2325–2334, 2010.

[100] D.H. Myszka. *Machines and Mechanisms: Applied Kinematic Analysis*. Pearson Prentice Hall, 2012.

[101] Wenyong Ma, Jianhan Liu, Yaya Jia, Longqian Jin, and Xinshuai Ma. The aerodynamic forces and wake flow of a rotating circular cylinder under various flow regimes. *Journal of Wind Engineering and Industrial Aerodynamics*, 224:104977, 2022.

[102] Katerine Van Ness, Alberto Aliseda, and Brian Polagye. Experimental comparison of passive adaptive blade pitch control strategies for an axial-flow current turbine. *Journal of Ocean Engineering and Marine Energy*, 10, 2024.

[103] K. Yousefi and A Razeghi. Determination of the critical reynolds number for flow over symmetric naca airfoils. 01 2018.

[104] F. E. Fish and G. V. Lauder. Passive and active flow control by swimming fishes. *Annual Review of Fluid Mechanics*, 38(1):193–224, 2006.

[105] B. Strom, S. Brunton, and B. Polagye. Intracycle angular velocity control of cross-flow turbines. *Natural Energy*, 2:17103, 2017.

[106] L. Graftieaux, M. Michard, and N. Grosjean. Combining PIV, POD and vortex identification algorithms for the study of unsteady turbulent swirling flows. *Measurement Science and Technology*, 12(9):1422–1429, 8 2001.

[107] K. J. Ryan, F. Coletti, C. J. Elkins, J. O. Dabiri, and J. K. Eaton. Three-dimensional flow field around and downstream of a subscale model rotating vertical axis wind turbine. *Experiments in Fluids*, 57(3):1–15, 2016.

[108] *Aerodynamics of Horizontal Axis Wind Turbines*, chapter 3, pages 39–136. John Wiley & Sons, Ltd, 2011.

[109] C. Simão Ferreira, H. Madsen, M. Barone, B. Roscher, P. Deglaire, and I. Arduin. Comparison of aerodynamic models for vertical axis wind turbines. *Journal of Physics: Conference Series*, 524:012125, 06 2014.

[110] A. A. Mohammed, H. M. Ouakad, A. Z. Sahin, and H. M. S. Bahaidarah. Vertical axis wind turbine aerodynamics: Summary and review of momentum models. *ASME. J. Energy Resour. Technol.*, 141(5):050801, 05 2019.

[111] S. L. Brunton, C. W. Rowley, and D. R. Williams. Reduced-order unsteady aerodynamic models at low reynolds numbers. *Journal of Fluid Mechanics*, 724:203–233, 2013.

[112] J. G. Holierhoek, J. B. de Vaal, A. H. van Zuijlen, and H. Bijl. Comparing different dynamic stall models. *Wind Energy*, 16(1):139–158, 2013.

[113] J. G. Leishman. Challenges in modelling the unsteady aerodynamics of wind turbines. *Wind Energy*, 5(2-3):85–132, 2002.

[114] K. M. Almohammadi, D. B. Ingham, L. Ma, and M. Pourkashanian. Modeling dynamic stall of a straight blade vertical axis wind turbine. *Journal of Fluids and Structures*, 57:144 – 158, 2015.

[115] E. M. Jonathan, L. A. Danao, and R. J. Howell. PIV measurements and CF simulation of the performance and flow physics and of a small-scale vertical axis wind turbine. *Wind Energy*, 18:201–217, 2015.

[116] M. Somoano and F. J. Huera-Huarte. Flow dynamics inside the rotor of a three straight bladed cross-flow turbine. *Applied Ocean Research*, 69:138–147, 2017.

[117] B. Sasson and D. Greenblatt. Effect of leading-edge slot blowing on a vertical axis wind turbine. *AIAA Journal*, 49:1932–1942, 09 2011.

[118] J. Yen and N. A. Ahmed. Enhancing vertical axis wind turbine by dynamic stall control

using synthetic jets. *Journal of Wind Engineering and Industrial Aerodynamics*, 114:12 – 17, 2013.

[119] O. S. Mohamed, A. A. Ibrahim, A. K. Etman, A. A. Abdelfatah, and A. M. R. Elbaz. Numerical investigation of darrieus wind turbine with slotted airfoil blades. *Energy Conversion and Management: X*, 5:100026, 2020.

[120] E. Sobhani, M Ghaffari, and M. J. Maghrebi. Numerical investigation of dimple effects on darrieus vertical axis wind turbine. *Energy*, 133:231 – 241, 2017.

[121] M. Elkhoury, T. Kiwata, and E. Aoun. Experimental and numerical investigation of a three-dimensional vertical-axis wind turbine with variable-pitch. *Journal of Wind Engineering and Industrial Aerodynamics*, 139:111 – 123, 2015.

[122] G. Abdalrahman, W. Melek, and F. Lien. Pitch angle control for a small-scale darrieus vertical axis wind turbine with straight blades (h-type vawt). *Renewable Energy*, 114:1353 – 1362, 2017.

[123] B. Strom. *Cross-Flow Turbine Fluid Mechanics: Experimental Optimization and Analysis*. PhD thesis, University of Washington, 2018.

[124] P. Schmid. Dynamic mode decomposition of numerical and experimental data. *Cambridge University Press*, 656:5–28, 2010.

[125] C. A. Consul, R. H. J. Willden, and S. C. McIntosh. Blockage effects on the hydrodynamic performance of a marine cross-flow turbine. *Philosophical Transactions of the Royal Society A: Mathematical, Physical and Engineering Sciences*, 371(1985):20120299, 2013.

[126] D. Greenblatt, A. B. Harav, and H. Mueller-Vahl. *Mechanism of Dynamic Stall Control on a Vertical Axis Wind Turbine*.

[127] E. Möllerström, P. Gipe, J. Beurskens, and F. Ottermo. A historical review of vertical axis

wind turbines rated 100 kw and above. *Renewable and Sustainable Energy Reviews*, 105:1 – 13, 2019.

[128] A. Bianchini, F. Balduzzi, G. Ferrara, and L. Ferrari. A computational procedure to define the incidence angle on airfoils rotating around an axis orthogonal to flow direction. *Energy Conversion and Management*, 126:790 – 798, 2016.

[129] F. Balduzzi, A. Bianchini, R. Maleci, G. Ferrara, and L. Ferrari. Blade design criteria to compensate the flow curvature effects in h-darrieus wind turbines. *Journal of Turbomachinery*, 137, 09 2014.

[130] Q. Li, T. Maeda, T. Kamada, J. Murata, K. Shimizu, T. Ogasawara, A. Nakai, and T. Kasuya. Effect of solidity on aerodynamic forces around straight-bladed vertical axis wind turbine by wind tunnel experiments (depending on number of blades). *Renewable Energy*, 96:928 – 939, 2016.

[131] Y. Wang, X. J. Sun, B. Zhu, H. J. Zhang, and D. G. Huang. Effect of blade vortex interaction on performance of darrieus-type cross flow marine current turbine. *Renewable Energy*, 86:316 – 323, 2016.

[132] Q. Li, T. Maeda, Y. Kamada, J. Murata, K. Furukawa, and M. Yamamoto. Measurement of the flow field around straight-bladed vertical axis wind turbine. *Journal of Wind Engineering and Industrial Aerodynamics*, 151:70 – 78, 2016.

[133] Q. Li, T. Maeda, Y. Kamada, J. Murata, K. Furukawa, and M. Yamamoto. On the relationships between local vortex identification schemes. *Journal of Fluid Mechanics*, 535:189–214, 2005.

[134] P. Bachant and M. Wosnik. Characterising the near-wake of a cross-flow turbine. *Journal of Turbulence*, 16(4):392–410, 2015.

[135] John O. Dabiri. Optimal vortex formation as a unifying principle in biological propulsion. *Annual Review of Fluid Mechanics*, 41(1):17–33, 2009.

[136] Theodore Yaotsu Wu. Fish swimming and bird/insect flight. *Annual Review of Fluid Mechanics*, 43(1):25–58, 2011.

[137] M. S. Triantafyllou, G. S. Triantafyllou, and D. K. P. Yue. Hydrodynamics of fishlike swimming. *Annual Review of Fluid Mechanics*, 32(1):33–53, 2000.

[138] Sahil Kommalapati. *Machine Learning for Coherent Structure Identification and Super Resolution in Turbulent flows*. PhD thesis, 2021.

[139] Brad Perfect, Nirnimesh Kumar, and JJ Riley. Vortex structures in the wake of an idealized seamount in rotating, stratified flow. *Geophysical Research Letters*, 45(17):9098–9105, 2018.

[140] Tian Ma and Shouhong Wang. *Geophysical Fluid Dynamics and Climate Dynamics*, pages 373–446. Springer New York, New York, NY, 2014.

[141] Fatma Ayancik and Karen Mulleners. All you need is time to generalise the goman–khrabrov dynamic stall model. *Journal of Fluid Mechanics*, 942, may 2022.

[142] Violin plots: A box plot-density trace synergism. *The American Statistician*, 52(2):181–184, 1998.

[143] Megan C Leftwich. *The hydrodynamics of lamprey locomotion*. PhD thesis, 2010.

[144] Gabriel Thomas Scarlett and Ignazio Maria Viola. Unsteady hydrodynamics of tidal turbine blades. *Renewable Energy*, 146:843–855, 2020.

[145] CP Butterfield, D Simms, G Scott, and AC Hansen. Dynamic stall on wind turbine blades. Technical report, National Renewable Energy Lab., Golden, CO (United States), 1991.

[146] Howon Lee, Nicholas Simone, Yunxing Su, Yuanhang Zhu, Bernardo Luiz R. Ribeiro, Jennifer A. Franck, and Kenneth Breuer. Leading edge vortex formation and wake trajectory: Synthesizing measurements, analysis, and machine learning. *arXiv preprint*, 2022.

[147] Norman D Ham and Melvin S Garelick. Dynamic stall considerations in helicopter rotors. *Journal of the American Helicopter Society*, 13(2):49–55, 1968.

[148] He Zhu, Hong Nie, Limao Zhang, Xiaohui Wei, and Ming Zhang. Design and assessment of octocopter drones with improved aerodynamic efficiency and performance. *Aerospace Science and Technology*, 106:106206, 2020.

[149] K. Y. Yeung and W. L. Ruzzo. Principal component analysis for clustering gene expression data . *Bioinformatics*, 17(9):763–774, 09 2001.

[150] Bernardo Luiz R. Ribeiro and Jennifer A. Franck. A machine learning approach to classify vortex wakes of energy harvesting oscillating foils, 2022.

[151] Laurel M. M. Marsh, Michael C. Barbour, Venkat Keshav Chivukula, Fanette Chassagne, Cory M. Kelly, Samuel H. Levy, Louis J. Kim, Michael R. Levitt, and Alberto Aliseda. Platelet dynamics and hemodynamics of cerebral aneurysms treated with flow-diverting stents. *Annals of Biomedical Engineering*, 48, 01 2020.

[152] Georgy E Manucharyan, Rosalinda Lopez-Acosta, and Monica M Wilhelmus. Spinning ice floes reveal intensification of mesoscale eddies in the western Arctic Ocean. *Scientific Reports*, 12(1):7070, 2022.

[153] Benjamin Strom, Brian Polagye, and Steven L Brunton. Near-wake dynamics of a vertical-axis turbine. *Journal of Fluid Mechanics*, 935:A6, 2022.

[154] G. Tescione, D. Ragni, C. He, C.J. Simão Ferreira, and G.J.W. van Bussel. Near wake flow analysis of a vertical axis wind turbine by stereoscopic particle image velocimetry. *Renewable Energy*, 70:47–61, 2014. Special issue on aerodynamics of offshore wind energy systems and wakes.

[155] C E Brunner, J Kiefer, MOL Hansen, and M Hultmark. Unsteady effects on a pitching airfoil at conditions relevant for large vertical axis wind turbines. *Journal of Physics: Conference Series*, 1618(5):052065, sep 2020.

[156] Kristen M. Thyng, Chad A. Greene, Robert D. Hetland, Heather M. Zimmerle, and Steven F. DiMarco. True colors of oceanography: Guidelines for effective and accurate colormap selection. *Oceanography*, September 2016.

[157] T.C. Hohman, L. Martinelli, and A.J. Smits. The effect of blade geometry on the structure of vertical axis wind turbine wakes. *Journal of Wind Engineering and Industrial Aerodynamics*, 207:104328, 2020.

[158] Daniel B. Araya, Tim Colonius, and John O. Dabiri. Transition to bluff-body dynamics in the wake of vertical-axis wind turbines. *Journal of Fluid Mechanics*, 813:346–381, 2017.

[159] Abigale Snortland, Aidan Hunt, Owen Williams, and Brian Polagye. Influence of the downstream blade sweep on cross-flow turbine performance. *arXiv preprint arXiv:2404.19072*, 2024.

[160] David Bensason, Sébastien Le Fouest, Anna Young, and Karen Mulleners. Greenberg's force prediction for vertical-axis wind turbine blades. *AIAA Journal*, 60(7):4467–4470, 2022.